Ultracold Rydberg Atoms

Thesis

Department of Physics and Astronomy

The Open University

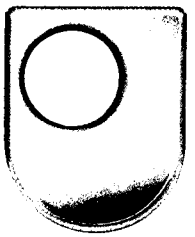

Michał J. Piotrowicz

Ultracold Rydberg Atoms

A thesis submitted for the degree of Doctor of Philosophy

Milton Keynes, 2010

Date of Submission: 2 September 2010

Date of Award: 19 January 2011

Yes, naturally stupid are all who are unaware of God,
and who, from good things seen,
have not been able to discover Him-who-is,
or, by studying the works, have not recognised the Artificer.
And if they have been impressed by their power and energy,
let them deduce from these how much mightier
is he that has formed them,
since through the grandeur and beauty of the creatures
we may, by analogy, contemplate their Author.

Wisdom 13:1,4–5

Summary

This thesis presents a new experimental facility that has been developed in the course of the PhD of the author together with the experimental measurements of the dipole moments for transitions between $5P_{3/2}$ and $nD_{5/2}$ states in ^{87}Rb atoms, where $20 \leq n \leq 48$. A laser cooling setup for rubidium atoms was designed and built that allows to produce 3×10^6 atoms at temperature of few microkelvins. A laser system for coherent excitation to Rydberg states was realised that exploits a two-photon ladder excitation scheme.

Such setup allowed to directly measure transition dipole moments from the first excited state to high n Rydberg states. The electromagnetically induced transparency and Autler-Townes splitting phenomena were exploited in order to obtain the values of the dipole moments, which were found to be in an excellent agreement with the theoretical values calculated using the quasiclassical approach by our collaborators in Novosibirsk.

To the author's knowledge, these are the first direct measurements of such dipole moments. The data shown in the thesis proves the reliability of the measurement method. The obtained results are extremely useful to validate theoretical models and gain insight in the physics of the interactions that will be an object of subsequent studies. The methods presented in the dissertation will be used in the future to detect in a non-destructive way Rydberg-Rydberg interactions within mesoscopic samples.

Contents

List of Figures

List of Tables

List of Abbreviations

AOM	Acousto-optic modulator
APP	Anamorphic prism pair
AT	Autler-Townes
BEC	Bose-Einstein condensate
BEM	Boundary element method
C-NOT	controlled NOT
CPO	Charged Particles Optics
ECDL	Extended-cavity diode laser
EIT	Electromagnetically induced transparency
EOM	Electro-optic modulator
MCP	Micro-channel plate
MOT	Magneto-optical trap
NA	Numerical aperture
OBE	Optical Bloch equations
PBS	Polarisation beam-splitter
PZT	Piezo-electric transducer
RWA	Rotating-wave approximation
SFI	State-selective field ionisation
SHG	Second harmonic generation/generator
TEC	Thermoelectric cooler

CHAPTER 1

Introduction

Rydberg atoms, atoms excited to highly electronic states, have been investigated for decades in gases at room temperature. The first observations of Rydberg atoms guided to Balmer's formula in the end of 19th century. Later Rydberg atoms were observed in he emission lines from distant galaxies (Mezger and Hoglund, 1967; Dravskikh and Dravskikh, 1967) and in early 70s of 20th century the advent of tunable lasers allowed a number of groups to study Rydberg atoms in laboratory. Energy levels of Rydberg states in rubidium were studied for instance by Lee *et al.* (1978) or Lorenzen and Niemax (1983). With the development of cooling methods for neutral atoms (Chu *et al.*, 1985) the possibility of a new range of investigations of Rydberg atoms in the ultracold regime opened up, where the kinetic energy of Rydberg atoms is small compared to the interactions amongst them, and thus their motion is negligible at the small timescales of a typical experimental measurement. The very first experiments with ultracold Rydberg atoms were carried out in 1998 in the USA (Anderson *et al.*, 1998) and in France (Mourachko *et al.*, 1998). In both experiments population transfers between Rydberg states were studied by spectroscopic methods. It was found that in a cold Rydberg gas the energy transfer resonances are broadened compared to

predictions based on a two-body collision process. This shows that the interactions have to be described in terms of many-body phenomena and this behaviour is more similar to that of solids. The term 'frozen Rydberg gas' was therefore proposed to describe this system.

Rydberg atoms are particularly interesting because of their extreme properties in comparison with 'normal' atoms. For instance, they display a huge polarisability, which makes them extremely sensitive to external electric fields, even those produced by neighbouring atoms. Several proposals to use Rydberg atoms as candidates for quantum computing (Jaksch *et al.*, 2000; Lukin *et al.*, 2001; Protsenko *et al.*, 2002) strongly rely on this enhanced sensitivity to other atoms. Specifically a two-qubit quantum gate can be operated exploiting entanglement between Rydberg atoms induced by the strong dipole-dipole interaction, e.g. in a series of micron-sized dipole traps. The realisation of a quantum gate based on Rydberg interactions has been achieved by Isenhower *et al.* (2010) and atom entanglement was demonstrated very recently by the same group (Zhang *et al.*, 2010).

By exploiting the strong interactions between ultracold Rydberg atoms, it is also possible to create collective excited states in a mesoscopic cloud, where a single excitation is shared between a number of atoms. This effect, occurring in dense ensembles, relies on the blockading of the excitation of multiple atoms simultaneously, which is enabled by the strong interactions amongst them. As a consequence the energy levels are shifted and a narrow band laser source cannot promote multiple excitations. The first evidence for this dipole blockade phenomenon was seen in a mesoscopic cold atom cloud (Tong *et al.*, 2004; Singer *et al.*, 2004; Cubel Liebisch *et al.*, 2005; Heidemann *et al.*, 2007), by observing the suppression of Rydberg excitations in the sample as a function of the density and the interaction strength. It was shown that within the sample blockaded regions are formed, where the atoms exhibit collective behaviour, manifesting itself

as an increase of the Rabi frequency of atoms flopping between the ground and Rydberg states (Heidemann *et al.*, 2007; Urban *et al.*, 2009; Gaëtan *et al.*, 2009).

Another quantum phenomenon which has attracted considerable attention in relation to Rydberg atoms is electromagnetically induced transparency (EIT). EIT is a phenomenon in which the transmission of light in a normally optically thick medium is greatly increased when two laser sources are used to couple two atomic transitions which share a common intermediate energy level and where a transition between the two remaining energy states is forbidden (figure 1.1). This

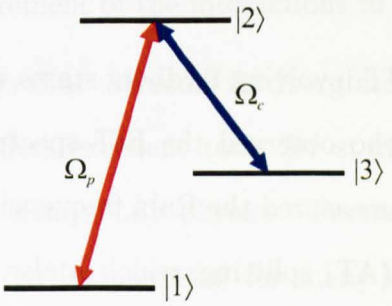

Figure 1.1: Three-level system for EIT. Two lasers (Ω_p and Ω_c) are coupled to two atomic transitions ($|1\rangle \rightarrow |2\rangle$ and $|2\rangle \rightarrow |3\rangle$) whereas transition between states $|1\rangle$ and $|3\rangle$ is dipole forbidden.

configuration leads to destructive quantum interference between the excitation paths resulting in a sharp modification of the optical properties of the medium and was named *electromagnetically induced transparency* by Harris *et al.* (1990). In EIT the presence of a coupling laser field creates transparency for the probe light around the resonance. The corresponding change in refractive index allows the manipulation of the group velocity of light, an effect commonly know as 'slow light'. The observation of the reduction of the group velocity of light to 17 m/s in a Bose-Einstein condensate (BEC) by Hau *et al.* (1999) has attracted great attention to this field. Small values of velocity were also observed by Kash *et al.* (1999) and Budker *et al.* (1999) in hot (room-temperature) rubidium gas. Hau's group further demonstrated a remarkable phenomenon (Liu *et al.*, 2001); the

slowed group velocity allowed the light pulse of the probe beam to be spatially compressed and contained completely in an atomic cloud. At this stage the coupling beam was rapidly switched off and the coherent information of the probe beam was stored into the atomic states. The information was subsequently read out by restoring the coupling field. This method allowed to store the light in a BEC for up to 1 millisecond. Recently the Durham group studied EIT in a cold Rydberg sample and demonstrated that EIT involving Rydberg states can lead to extremely large Kerr effect due to the very high polarisability of Rydberg states (Mohapatra *et al.*, 2008).

The investigation of EIT involving Rydberg states was pioneered by the work of Clarke *et al.* (2001), who observed the EIT spectra in a room-temperature rubidium vapour cell and measured the Rabi frequencies for transitions $5P_{3/2} \rightarrow 8D_{3/2,5/2}$. Autler-Townes (AT) splitting, which is also an effect arising from coherent atom-light interactions, closely related to EIT, was observed in cold Rydberg atoms by Teo *et al.* (2003). Contrary to most experiments, they used the $5S_{1/2} \rightarrow 5P_{3/2}$ as a coupling transition, while $5P_{3/2} \rightarrow 44D$ was the probe transition. They measured the dependence of the Autler-Townes splitting on pump polarisation, intensity, and detuning and found their results in agreement with calculations derived solving the density matrix equations.

In 2005 Friedler *et al.* (2005) proposed a scheme based on slow light and EIT in Rydberg atoms to realise a photonic phase gate, which relies on photon-atoms entanglement. This motivated Mohapatra *et al.* (2007) to observe EIT in room temperature rubidium with Rydberg states involving $n = 26 - 124$. The EIT peaks they measured were very narrow, allowing them to measure the fine structure splitting of the *nd* series. In their next work, Weatherill *et al.* (2008), they have investigated EIT in ultracold atoms trapped in a MOT for $n = 19 - 26$. In the regime of a weakly interacting Rydberg gas a depopulation of Rydberg states was observed and from signatures in EIT spectra they could detect

interactions between Rydberg atoms. For powers of the probe laser that enabled a few per cent of the population to be transferred into the Rydberg state, they observed a significant reduction of the Rydberg state population that could not be explained by the spontaneous decay, nor by optical pumping, so they deduced that it was due to the strong interactions that alter the dynamics of the system on a much faster timescale then the Rydberg lifetime. This effect was proved to be enhanced at higher density, when the interatomic distance is reduced and the interactions are stronger. This work indicates that EIT could be efficiently used for non-destructive measurement of the interactions in cold Rydberg sample.

The above review shows that ultracold Rydberg atoms are a rapidly growing field of research, which offers excellent tools for studies of atom-atom, atom-photon entanglement and many-body physics. Furthermore, the recent developments in the field, proved its potential for many envisaged applications in quantum computing and cold chemistry (Bendkowsky *et al.*, 2009). At the Open University a new state-of-the-art facility for ultracold Rydberg atoms have been developed, which is the subject of this thesis. The setup allows for the investigation of the dipole blockade and collective excitation of Rydberg atoms in a high density sample. A lot of effort was devoted to the design and building of the apparatus, which will be described in detail, and to the creation of an ultracold cloud of atoms and the laser excitation sources.

Motivated by the possibility of exploiting EIT for non-destructive measurements of the excitations and by the need to validate theoretical models that will guide future experiments, the EIT and AT spectra involving different Rydberg states in rubidium 87 were observed, from which the dipole moments for transitions to Rydberg states were obtained. Despite the number of existing theoretical models (e.g. Bates and Damgaard, 1949; Theodosiou, 1984; Gounand, 1979), a lack of experimental data on the dipole matrix elements for rubidium complicates their verification, with the exception for transitions between the ground and the

first excited state. Until now, only oscillator strengths for $5S \rightarrow nP_{1/2,3/2}$ transitions in rubidium with $n \leq 20$ were measured by Caliebe and Niemax (1979) and later, measurements for $n \leq 26$ were done by Shabanova and Khlyustalov (1984). Indirect verification of the theoretical calculations of the radial matrix elements was also achieved by comparing the experimentally measured lifetimes of rubidium Rydberg states with the theory (Theodosiou, 1984; Branden *et al.*, 2010; Beterov *et al.*, 2009). However, the calculation of lifetimes was done by summing over a large number of spontaneous and black-body radiation induced transition rates, thus making the spectroscopic features of each transition unobservable. Hence, direct measurements of the radial matrix elements are necessary for the validation of these models. Presented in this thesis are the measured values of dipole matrix elements for transitions between states $5P_{3/2}$ and $nD_{5/2}$, for $n = 20 - 48$ obtained by deducing the Rabi frequency from AT splitting measurements, which are found to be in a very good agreement with the semi-classical calculations by Beterov (2010).

The structure of this thesis is as follows: chapter 2 gives the background theory on atom-light interaction, starting from the two-level atom interacting with a light field and leading to electromagnetically induced transparency in a three-level system. The description of the system is carried out using the optical Bloch equations. In chapter 3 properties of Rydberg atoms are introduced and a comparison with hydrogen atoms is made, by introducing the quantum defect theory. This chapter describes also the interactions between Rydberg atoms that lead to dipole blockade and its applications.

Chapter 4 deals with the experimental setup and methods. It describes the work carried out by the author in building a new facility to investigate ultracold Rydberg atoms. It presents the principles of operation of laser cooling and magneto-optical trapping and shows the experimental implementation and the

preparation of a cold atoms sample. The laser setup used for two-photon excitation of Rydberg state and EIT experiments is also described in detail.

The main results of this thesis are presented in chapter 5. The detailed description of obtaining and interpreting EIT/AT spectra is presented, which enables to measure dipole transitions to Rydberg states. The results are compared with semi-classical calculations carried out by our collaborators in Novosibirsk.

In chapter 6 the simulations of the detection system of Rydberg atoms and the design of a new vacuum chamber are briefly described. The new vacuum chamber will allow the detection of Rydberg atoms by selective field ionisation. The new system has the potential to be upgraded to achieve very high spatial resolution, which will allow the detection of single Rydberg atoms separated by a few tens of micrometres.

CHAPTER 2

Review on Atom-Light Interaction

This chapter will present a review on the interaction of light with atoms, starting from a two energy level atom interacting with a classical electric field. The optical Bloch equations will be derived for the two-level case and this treatment will then be extended to the three-level case. A three-level system interacting with two laser fields can show interesting features, like electromagnetically induced transparency (EIT) and Autler-Townes (AT) splitting, which are linked to coherent processes induced by the laser fields.

2.1 The two-level atom

The interaction of a two-level atom with a classical electromagnetic field is first considered. The states of the atom are labelled $|1\rangle$ for the ground state, and $|2\rangle$ for the excited state, with energies E_1 and E_2 respectively and energy difference, $\omega_{21} = (E_2 - E_1)/\hbar$ (see figure 2.1). The time-dependent Schrödinger's equation is written as

$$i\hbar\frac{\partial\Psi}{\partial t} = \mathcal{H}\Psi, \tag{2.1}$$

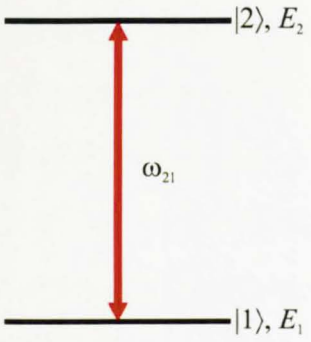

Figure 2.1: Two level atom. States $|1\rangle$ and $|2\rangle$, with energies E_1 and E_2, are separated by $\omega_{21} = (E_2 - E_1)/\hbar$.

and for an interacting system the Hamiltonian has two parts

$$\mathcal{H} = \mathcal{H}_0 + \mathcal{H}_{Int}(t), \tag{2.2}$$

where, $\mathcal{H}_0$ is the Hamiltonian for a free single-electron atom and $\mathcal{H}_{Int}$ is the time-dependent interaction between the atom (or more precisely, the valence electron charge, $-e$, in the atom) and the oscillating electric field.

The general state $|\Psi\rangle$ of the whole system evolves in time and can be defined in terms of the probability amplitudes $c_n(t)$:

$$|\Psi\rangle = \sum_n c_n(t) e^{-iE_n t/\hbar} |\psi_n\rangle, \tag{2.3}$$

where states $|\psi_n\rangle$ form an orthonormal basis with energies E_n, where for a two-level system $n = 1, 2$.

Substituting the general state 2.3 into the time dependent Schrödinger's equation 2.1 the dynamics of the system can be described by the following equation governing the time evolution of $c_n(t)$:

$$\frac{dc_n(t)}{dt} = -\frac{i}{\hbar} \sum_m c_m(t) H_{nm}^{Int} e^{-i\omega_{mn} t}. \tag{2.4}$$

Here $\omega_{mn} = (E_m - E_n)/\hbar$ and $H_{nm}^{Int} = \langle \psi_n | \mathcal{H}_{Int} | \psi_m \rangle$ are matrix elements.

2.1.1 Rabi oscillations

The electromagnetic field, which models light of frequency ω_L interacting with the atom, is described by an oscillating electric field $\vec{E} = \frac{1}{2}\vec{E}_0 \left(e^{i\omega_L t} + e^{-i\omega_L t}\right)$. In the electric dipole approximation the Hamiltonian takes the following form:

$$\mathcal{H}_{Int}(t) = -e\vec{r} \cdot \vec{E} = -\frac{e}{2}\vec{r} \cdot \vec{E}_0 \left(e^{i\omega_L t} + e^{-i\omega_L t}\right) \tag{2.5}$$

with $\vec{r}$ being the position of electron with respect to the atom's centre of mass.

Using equations 2.4 with $n = 1, 2$ one can obtain the evolution of the probability amplitudes for a two-level system, as the interaction with the electric field mixes the two states with energies E_1 and E_2. The explicit expression of the interaction Hamiltonian 2.5 is substituted into equation 2.4 and leads to a set of equations

$$\begin{aligned} \frac{dc_1(t)}{dt} &= \frac{i\Omega}{2}\left(e^{i\omega_L t} + e^{-i\omega_L t}\right) e^{-i\omega_{21} t} c_2(t) \\ \frac{dc_2(t)}{dt} &= \frac{i\Omega}{2}\left(e^{i\omega_L t} + e^{-i\omega_L t}\right) e^{i\omega_{21} t} c_1(t), \end{aligned} \tag{2.6}$$

where Ω is the Rabi frequency for the $|1\rangle$ to $|2\rangle$ transition defined as:

$$\Omega = -\frac{\langle 1|e\vec{r} \cdot \vec{E}|2\rangle}{\hbar}. \tag{2.7}$$

The significance of the Rabi frequency will be explained in the following paragraphs.

The equations 2.6 can be rewritten and terms with $\omega_{21} + \omega_L$ and $\delta = \omega_L - \omega_{21}$ will appear in the exponent which represent events happening at different timescales. If the radiation has a frequency close to the atomic resonance (ω_{21}) the terms with frequencies $\omega_{21} + \omega_L$ are fast oscillating and can be neglected as they average to zero over the interaction time. This approximation, called

rotating-wave approximation (RWA), leads to the simplified relations

$$\begin{aligned} \frac{dc_1(t)}{dt} &= \frac{i\Omega}{2} e^{i\delta t} c_2(t) \\ \frac{dc_2(t)}{dt} &= \frac{i\Omega}{2} e^{-i\delta t} c_1(t). \end{aligned} \tag{2.8}$$

If these equations are solved for initial conditions $c_1(0) = 1$ and $c_2(0) = 0$, so that at time $t = 0$ the atom is in the ground state, then the probability of being excited to the upper state is

$$|c_2(t)|^2 = \frac{\Omega^2}{\Omega^2 + \delta^2} \sin^2\left(\frac{\sqrt{\Omega^2 + \delta^2}}{2} t\right). \tag{2.9}$$

At resonance $\omega_L = \omega_{21}$, so this probability becomes

$$|c_2(t)|^2 = \sin^2\left(\frac{\Omega t}{2}\right). \tag{2.10}$$

and the population oscillates between the two levels at frequency Ω. Those oscillations are called Rabi oscillations. For a laser pulse of duration t such that $\Omega t = \pi$ all the population is transferred from state $|1\rangle$ into state $|2\rangle$. The half duration pulses (for the same Rabi frequency Ω) ($\pi/2$-pulses) put the atom wave function in a superposition of states $|1\rangle$ and $|2\rangle$ with equal amplitudes.

2.1.2 The density matrix and the optical Bloch equations

A convenient mean of describing a quantum system is to use the density matrix. It is especially useful for the description of mixed states, which consist of the statistical mix of pure states $|\Psi_i\rangle$ with probabilities p_i. The density matrix operator of the state is defined as

$$\rho = \sum_i p_i |\Psi_i\rangle\langle\Psi_i|. \tag{2.11}$$

The two-level atom is described by a pure state $|\Psi\rangle = c_1|1\rangle + c_2|2\rangle$, so all the probabilities p_i are zero, except one. Thus the density matrix elements have the form:

$$\rho_{nm} = c_n(t)c_m^*(t) \tag{2.12}$$

where $n, m = 1, 2$. ρ_{11} and ρ_{22} are the probabilities of being in the ground and excited state respectively, ρ_{12} and ρ_{21} express the interference effects between states $|1\rangle$ and $|2\rangle$, and if they are non-zero they show that a certain degree of coherence exists between these states. Hence ρ_{nm}, $n \neq m$, are called coherences.

The time evolution of the density matrix can be derived from eqn 2.12 in terms of probability amplitudes:

$$\frac{d\rho_{nm}}{dt} = \frac{dc_n(t)}{dt}c_m^*(t) + c_n(t)\frac{dc_m^*(t)}{dt}. \tag{2.13}$$

Until now coherent interaction of an atom with light was considered, and the dynamics were described by simple sinusoidal functions that were completely reversible. In reality these oscillations are damped by relaxation leading to decoherence. Spontaneous emission is a relaxation phenomena that occurs when an atom interacts with electric field and is an irreversible process. It can be included in this treatment by introducing it phenomenologically, i.e. by subtracting terms representing the radiative decay rates. The decay of population of the excited state, ρ_{22}, can be modelled in the same way as a damping term for the oscillator, so the time evolution of the density matrix elements (ρ_{22} and ρ_{12}) can be written as:

$$\begin{aligned}
\frac{\partial\rho_{22}}{\partial t} &= \frac{i\Omega}{2}\left(\rho_{12}e^{-i\delta t} - \rho_{21}e^{i\delta t}\right) - \Gamma\rho_{22} \\
\frac{\partial\rho_{12}}{\partial t} &= \frac{i\Omega}{2}e^{i\delta t}\left(\rho_{22} - \rho_{11}\right) - \frac{\Gamma}{2}\rho_{12}
\end{aligned} \tag{2.14}$$

Here $\Gamma = 1/\tau$ (rad/s), and τ is the excited state lifetime ($\tau = 26.23$ ns, $\Gamma = 6.065$ MHz for ^{87}Rb D2 transitions, (Gutterres *et al.*, 2002)). The remaining elements are then found from the relations $\rho_{11} = 1 - \rho_{22}$ and $\rho_{12} = \rho_{21}^*$.

It is helpful to simplify those equations by applying the following transformation that removes the oscillatory factors:

$$\begin{aligned} \tilde{\rho}_{12} &= \rho_{12} e^{-i\delta t} \\ \tilde{\rho}_{21} &= \rho_{21} e^{i\delta t}. \end{aligned} \tag{2.15}$$

This transformation does not affect the population, as $\rho_{11} = \tilde{\rho}_{11}$ and $\rho_{22} = \tilde{\rho}_{22}$ and yields the following:

$$\begin{aligned} \frac{\partial \tilde{\rho_{12}}}{\partial t} &= -\left(i\delta + \frac{\Gamma}{2}\right)\tilde{\rho}_{12} + \frac{i\Omega}{2}(\rho_{22} - \rho_{11}) \\ \frac{\partial \tilde{\rho_{21}}}{\partial t} &= -\left(-i\delta + \frac{\Gamma}{2}\right)\tilde{\rho}_{21} - \frac{i\Omega}{2}(\rho_{22} - \rho_{11}) \\ \frac{\partial \rho_{11}}{\partial t} &= \frac{i\Omega}{2}(\tilde{\rho}_{21} - \tilde{\rho}_{12}) + \Gamma\rho_{22} \\ \frac{\partial \rho_{22}}{\partial t} &= \frac{i\Omega}{2}(\tilde{\rho}_{12} - \tilde{\rho}_{21}) - \Gamma\rho_{22}. \end{aligned} \tag{2.16}$$

The above equations are called the *optical Bloch equations* (OBE) and give the description of the dynamics of excitation of a two-level atom by radiation close to resonance, including decays by spontaneous emission. They also give the full description of the time evolution of both populations and coherences in the system. OBE can be easily generalised to include extra levels and fields, in particular this will be presented in section 2.2.1 for three-level atomic system and two light fields.

The OBE can be also derived starting from the time evolution of the density matrix with damping added by introducing the *decay matrix*, $\mathcal{D}$, that describes

the damping of the populations and coherences:

$$\frac{d\rho}{dt} = -\frac{i}{\hbar}[\mathcal{H}, \rho] + \mathcal{D}, \tag{2.17}$$

with the interaction Hamiltonian in the rotating frame of the following form:

$$\mathcal{H}_{Int}^{RWA} = -\frac{\hbar}{2}\begin{pmatrix} 0 & \Omega \\ \Omega & -2\delta \end{pmatrix}, \tag{2.18}$$

and decay matrix:

$$\mathcal{D} = \begin{pmatrix} \Gamma\rho_{22} & -\frac{\Gamma}{2}\tilde{\rho}_{12} \\ -\frac{\Gamma}{2}\tilde{\rho}_{21} & -\Gamma\rho_{22} \end{pmatrix}, \tag{2.19}$$

where the excited state energy is shifted by δ. This Hamiltonian can be generalised to multi-level systems, and also to describe electromagnetically induced transparency, as it will be shown in the following sections (Fleischhauer *et al.*, 2005).

2.1.3 Scattering rate

The steady-state solution of the OBE of the system is reached at times which are long compared to the lifetime of the upper state. It can be derived by setting the time derivatives to zero, and the steady-state population of the upper level is then found to be

$$\rho_{22} = \frac{\Omega^2}{\Gamma^2 + 4\delta^2 + 2\Omega^2}. \tag{2.20}$$

It is useful to define the saturation intensity $I_{sat} = \frac{\pi hc}{3\lambda^3\tau}$, where c is the speed of light, λ is the wavelength of the transition and h is Planck's constant, to link the population of excited state to the intensity of the light via the saturation parameter, I/I_{sat}, defined as:

$$\frac{I}{I_{sat}} = \frac{2\Omega^2}{\Gamma^2}. \tag{2.21}$$

For ^{87}Rb $|F = 2, m_F = \pm 2\rangle \rightarrow |F' = 3, m'_F = \pm 3\rangle$ transition $I_{sat} = 1.669\,\mathrm{mW/cm^2}$. Using the saturation parameter the population of the upper level (eqn 2.20) can be rewritten as

$$\rho_{22} = \frac{1}{2}\frac{I/I_{sat}}{1 + I/I_{sat} + 4\delta^2/\Gamma^2}. \tag{2.22}$$

Having obtained the steady-state population, the total scattering rate of light can be derived. It is given by the population of the excited state times the decay rate:

$$R = \frac{\Gamma}{2}\frac{I/I_{sat}}{1 + I/I_{sat} + 4\delta^2/\Gamma^2}. \tag{2.23}$$

This result plays a significant role in understanding the radiation force and the operation laser cooling, as will be seen in chapter 4.

2.2 The three-level ladder atom

In the previous sections the interaction between the electromagnetic field and two-level atom was presented. Here the results will be extended to a three-level system interacting with two light fields. The three-level atomic system considered here is called a ladder or cascade system and is presented in figure 2.2a. The transition between states $|1\rangle$ and $|3\rangle$ is dipole forbidden, so there is no direct coupling

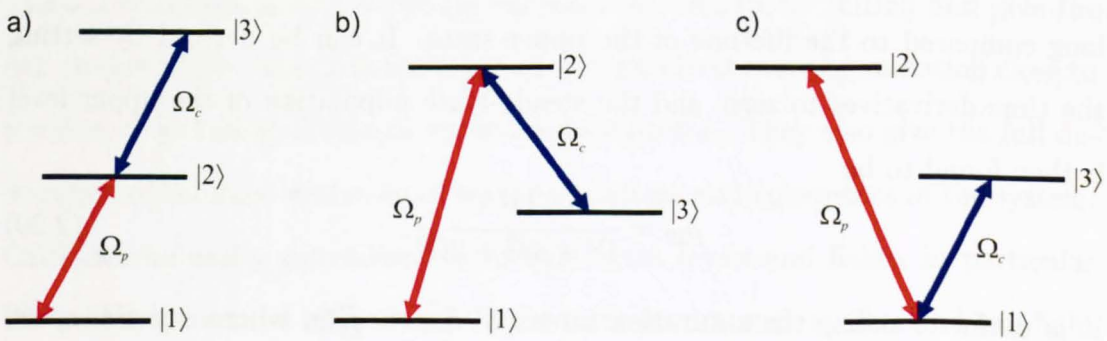

Figure 2.2: Three-level systems: a) ladder, b) lambda, c) vee. In a) and b) transition between states $|1\rangle$ and $|3\rangle$ is dipole forbidden, and in c) between $|2\rangle$ and $|3\rangle$. Ω_p and Ω_c are Rabi frequencies of the two laser sources interacting with the system.

between these states. The excitation to Rydberg state in our experiment follows the two-photon scheme via the ladder system. In this case the state $|1\rangle$ is the ground state of rubidium atoms ($5S_{1/2}$) while $|2\rangle$ is the first excited state $|5P_{3/2}\rangle$ and $|3\rangle$ is a Rydberg state nD. It is worth noticing that ladder system is not the only configuration of three-level atom in which the dipole forbidden transition exists. The others are lambda (Λ) and vee (V) systems (see figure 2.2b,c) and it is relatively straightforward to generalise the results obtained for the ladder system to Λ and V configurations.

2.2.1 The optical Bloch equations for the three-level ladder system

As in the two-level case, the Hamiltonian for the system has to be derived. The three-level interaction part of the Hamiltonian (a 3×3 matrix) has the following elements

$$\begin{aligned} H_{11}^{Int} &= H_{22}^{Int} = H_{33}^{Int} = 0 \\ H_{12}^{Int} &= H_{21}^{Int} = \frac{\hbar\Omega_p}{2}\left(e^{i\omega_p t} + e^{-i\omega_p t}\right) \\ H_{23}^{Int} &= H_{32}^{Int} = \frac{\hbar\Omega_c}{2}\left(e^{i\omega_c t} + e^{-i\omega_c t}\right). \end{aligned} \tag{2.24}$$

The two laser fields are forming this Hamiltonian: the probe and the coupling field, that are driving the $|1\rangle \rightarrow |2\rangle$ and $|2\rangle \rightarrow |3\rangle$ transitions respectively. Those lasers have frequencies ω_p and ω_c and may be detuned from the atomic transitions by $\Delta_p = \omega_{21} - \omega_p$ and $\Delta_c = \omega_{32} - \omega_c$. Ω_p and Ω_c are Rabi frequencies of the probe and coupling laser fields. The OBE for the three-level system can be derived in the similar way as for the two-level atom by calculating the time evolution of the density matrix elements and making RWA. However, it was mentioned that OBE can comes naturally from eqn 2.17. The Hamiltonian in the rotating frame for

the three-level ladder system has the form (Fleischhauer *et al.*, 2005):

$$\mathcal{H}_{Int}^{RWA} = -\frac{\hbar}{2}\begin{pmatrix} 0 & \Omega_p & 0 \\ \Omega_p & -2\Delta_p & \Omega_c \\ 0 & \Omega_c & -2(\Delta_p + \Delta_c) \end{pmatrix}. \tag{2.25}$$

The decays and dephasing should be added phenomenologically (figure 2.3) by adding the decay matrix $\mathcal{D}$. Spontaneous emission from $|2\rangle$, which is assumed to decay only to level $|1\rangle$, is modelled as a term proportional to the population of state $|2\rangle$, the proportionality constant being a decay rate Γ_{21} (as in two-level system). The state $|3\rangle$ can decay to the $|2\rangle$, however, as the lifetime of Rydberg

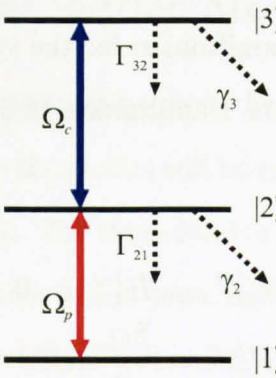

Figure 2.3: Three-level scheme with decays. Γ_{21} and Γ_{32} are radiative decay rates from states $|2\rangle$ and $|3\rangle$ respectively, and γ_2 and γ_3 are dephasing rates of those states.

states is very long, the decay rates from Rydberg states due to lifetime can be neglected, so Γ_{32} is negligible. The off-diagonal elements, ρ_{ij}, $i \neq j$, decay at half the spontaneous rate for the two levels involved (Γ_{ij}), plus an additional dephasing rate (γ_i) that include all decoherence rates (laser fluctuations, etc.) (Fleischhauer *et al.*, 2005). This gives the following decay rates for the off-diagonal elements: $\gamma_{32} = \frac{1}{2}(\gamma_2 + \gamma_3 + \Gamma_{21})$, $\gamma_{21} = \frac{1}{2}(\gamma_2 + \Gamma_{21})$ and $\gamma_{31} = \frac{1}{2}\gamma_3$, as decay from $|3\rangle$ are

neglected and $|1\rangle$ is a ground state. Thus the decay matrix has the form:

$$\mathcal{D} = \begin{pmatrix} \Gamma_{21}\rho_{22} & -\frac{\Gamma_{21}+\gamma_2}{2}\tilde{\rho}_{12} & -\frac{\gamma_3}{2}\tilde{\rho}_{13} \\ -\frac{\Gamma_{21}+\gamma_2}{2}\tilde{\rho}_{21} & -\Gamma_{21}\rho_{22} & -\frac{\Gamma_{21}+\gamma_2+\gamma_3}{2}\tilde{\rho}_{23} \\ -\frac{\gamma_3}{2}\tilde{\rho}_{31} & -\frac{\Gamma_{21}+\gamma_2+\gamma_3}{2}\tilde{\rho}_{32} & 0 \end{pmatrix}. \tag{2.26}$$

Now the OBE with decays can be written:

$$\begin{aligned}
\frac{d\rho_{11}}{dt} &= i\frac{\Omega_p}{2}\left(\tilde{\rho}_{12} - \tilde{\rho}_{21}\right) + \Gamma_{21}\rho_{22} \\
\frac{d\rho_{22}}{dt} &= i\frac{\Omega_p}{2}\left(\tilde{\rho}_{21} - \tilde{\rho}_{12}\right) + i\frac{\Omega_c}{2}\left(\tilde{\rho}_{23} - \tilde{\rho}_{32}\right) - \Gamma_{21}\rho_{22} \\
\frac{d\rho_{33}}{dt} &= i\frac{\Omega_c}{2}\left(\tilde{\rho}_{32} - \tilde{\rho}_{23}\right) \\
\frac{d\tilde{\rho}_{12}}{dt} &= -\left(i\Delta_p + \frac{\Gamma_{21}+\gamma_2}{2}\right)\tilde{\rho}_{12} + i\frac{\Omega_p}{2}\left(\rho_{11} - \rho_{22}\right) + i\frac{\Omega_c}{2}\tilde{\rho}_{13} \\
\frac{d\tilde{\rho}_{23}}{dt} &= \left(i\Delta_c - \frac{\Gamma_{21}+\gamma_2+\gamma_3}{2}\right)\tilde{\rho}_{23} + i\frac{\Omega_c}{2}\left(\rho_{22} - \rho_{33}\right) - i\frac{\Omega_p}{2}\tilde{\rho}_{13} \\
\frac{d\tilde{\rho}_{13}}{dt} &= i\left(\Delta_p + \Delta_c - \frac{\gamma_3}{2}\right)\tilde{\rho}_{13} + i\frac{\Omega_c}{2}\tilde{\rho}_{12} - i\frac{\Omega_p}{2}\tilde{\rho}_{23}.
\end{aligned} \tag{2.27}$$

2.2.2 Electromagnetically induced transparency and Autler-Townes splitting

In a three-level atomic system, as described above, coherence and quantum interference effects occur when the system is excited by two resonant laser fields. These effects can result in cancellation of light absorption, leading to electromagnetically induced transparency (EIT). Two levels, $|2\rangle$ and $|3\rangle$, are strongly coupled by a coherent laser beam, called the coupling beam, and the sample is probed on a transition $|1\rangle \rightarrow |2\rangle$ by a weak, coherent probe beam (see figure 2.4). Levels $|1\rangle$ and $|3\rangle$ are not coupled, as such a transition is dipole forbidden. Usually the coupling beam is resonant with the $|2\rangle \rightarrow |3\rangle$ transition and the probe beam experiences the cancellation of absorption when its frequency is tuned to $|1\rangle \rightarrow |2\rangle$ resonance. To understand this phenomenon one should consider the

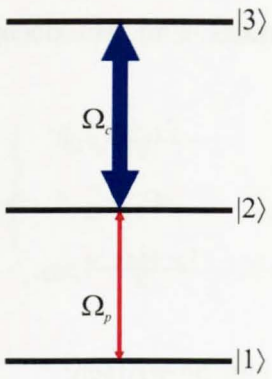

Figure 2.4: Three-level ladder atomic system for EIT. States $|2\rangle$ and $|3\rangle$ are coupled by strong coupling light Ω_c and transition between states $|1\rangle$ and $|2\rangle$ is probed by weak probe light Ω_p.

interaction Hamiltonian at the resonance condition $\Delta_p + \Delta_c = 0$:

$$\mathcal{H}^{Int} = -\frac{\hbar}{2}\begin{pmatrix} 0 & \Omega_p & 0 \\ \Omega_p & -2\Delta_p & \Omega_c \\ 0 & \Omega_c & 0 \end{pmatrix}. \tag{2.28}$$

Then the eigenvalues are

$$\begin{aligned} \omega_0 &= 0 \\ \omega_\pm &= \frac{1}{2}\left(\Delta_p \pm \sqrt{\Delta_p^2 + \Omega_p^2 + \Omega_c^2}\right), \end{aligned} \tag{2.29}$$

and the corresponding eigenvectors can be written

$$\begin{aligned} |a_+\rangle &= \sin\Theta\sin\Phi|1\rangle + \cos\Phi|2\rangle + \cos\Theta\sin\Phi|3\rangle \\ |a_0\rangle &= \cos\Theta|1\rangle - \sin\Theta|3\rangle \\ |a_-\rangle &= \sin\Theta\cos\Phi|1\rangle - \sin\Phi|2\rangle + \cos\Theta\cos\Phi|3\rangle, \end{aligned} \tag{2.30}$$

where Θ and Φ are so-called 'mixing angles' that are dependent in a simple way upon the Rabi frequencies and the detunings, and for resonance are defined as

$\tan\Theta = \Omega_p/\Omega_c$ and $\tan 2\Phi = \sqrt{\Omega_p^2 + \Omega_c^2}/\,\Delta_p$ (Fleischhauer *et al.*, 2005). States $|a_\pm\rangle$ contain all three atomic states, while $|a_0\rangle$ has no contribution from state $|2\rangle$, so in the $|a_0\rangle$ state the atomic population is trapped in $|1\rangle$ and $|3\rangle$ states and therefore there is no absorption of the probe light. The non-absorbing state is called a dark state; the system evolves to the dark state by spontaneous decay from other states. Hence in the steady-state, at the resonance the probe beam is no longer absorbed by atoms and the medium becomes transparent to the probe laser. Using the dressed-state picture of states ($|a_0\rangle$ and $|a_\pm\rangle$) in the weak probe case ($\Omega_p \ll \Omega_c$) the ground state becomes $|a_0\rangle$ (as $\Theta \to 0$) from which the excitation cannot occur. It means that in the case of strong coupling beam most of the atoms remain in the ground, $|1\rangle$, state. EIT was first proposed by Harris *et al.* (1990) and was for the first time observed by the same group (Boller *et al.*, 1991) in a strontium vapour.

Assuming a strong coupling field ($\Omega_C \gg \Omega_p$) the populations of states $|2\rangle$ and $|3\rangle$ can be neglected ($\rho_{11} \approx 1$, $\rho_{22} \approx 0$ and $\rho_{33} \approx 0$), thus solving the optical Bloch equations for the steady state ($\frac{d\rho}{dt} = 0$) one gets (Gea-Banacloche *et al.*, 1995):

$$\tilde{\rho}_{12} \approx \frac{i\Omega_p}{\Gamma_{12} - 2i\Delta_p + \frac{\Omega_c^2}{\gamma_3 - 2i(\Delta_p + \Delta_c)}}. \tag{2.31}$$

The coherence of states $|1\rangle$ and $|2\rangle$ gives the information about the absorption and dispersion of the probe beam propagating through the atoms. It can be derived starting from the relation of the polarisation in terms of electric field, $P = \frac{1}{2}\epsilon_0 \vec{E}_p^0 \left[\chi(\omega_p)e^{-i\omega_p t} + \chi(\omega_p)e^{i\omega_p t}\right]$, where $\vec{E}_p = \vec{E}_p^0 \left(e^{-i\omega_p t} + e^{i\omega_p t}\right)$ is the oscillating electric field of the probe beam, and χ is the complex electric susceptibility. The polarisation of an atomic sample is given as $P = N\langle e\vec{r}\rangle$, with N – the number density, so that

$$P = N\mu_{21}\left(\rho_{21}e^{i\omega_p t} + \rho_{12}e^{-i\omega_p t}\right), \tag{2.32}$$

where μ_{21} is the dipole moment element. It follows that:

$$\chi = -\frac{2N|\mu_{21}|^2\rho_{21}}{\hbar\epsilon_0\Omega_p}. \tag{2.33}$$

χ is complex, $\chi = \chi_{Re} + i\chi_{Im}$, and the absorption coefficient is calculated using the imaginary part of the susceptibility, thus the probe absorption is proportional to $\mathrm{Im}(\tilde{\rho}_{12})$:

$$Im(\tilde{\rho}_{12}) = \frac{\Omega_p\left(\Gamma_{12}\gamma_3^2 + 4\Gamma_{12}\left(\Delta_p + \Delta_c\right)^2 + \gamma_3\Omega_c^2\right)}{\left(\Gamma_{12}^2 + 4\Delta_p^2\right)\left(\gamma_3^2 + 4\left(\Delta_c + \Delta_p\right)^2\right) + 2\left(\Gamma_{12}\gamma_3 - 4\Delta_p\left(\Delta_p + \Delta_c\right)\right)\Omega_c^2 + \Omega_c^4} \tag{2.34}$$

Figure 2.5 shows the calculated probe absorption profile as a function of its detuning from the resonance (Δ_p) for different values of the Rabi frequency of the coupling field. Here, γ_3 was set to zero. This models the theoretical situation where there is no decoherence in the system, and it allows to see the effect of the coupling beam on the absorption of the probe beam depending on the Rabi

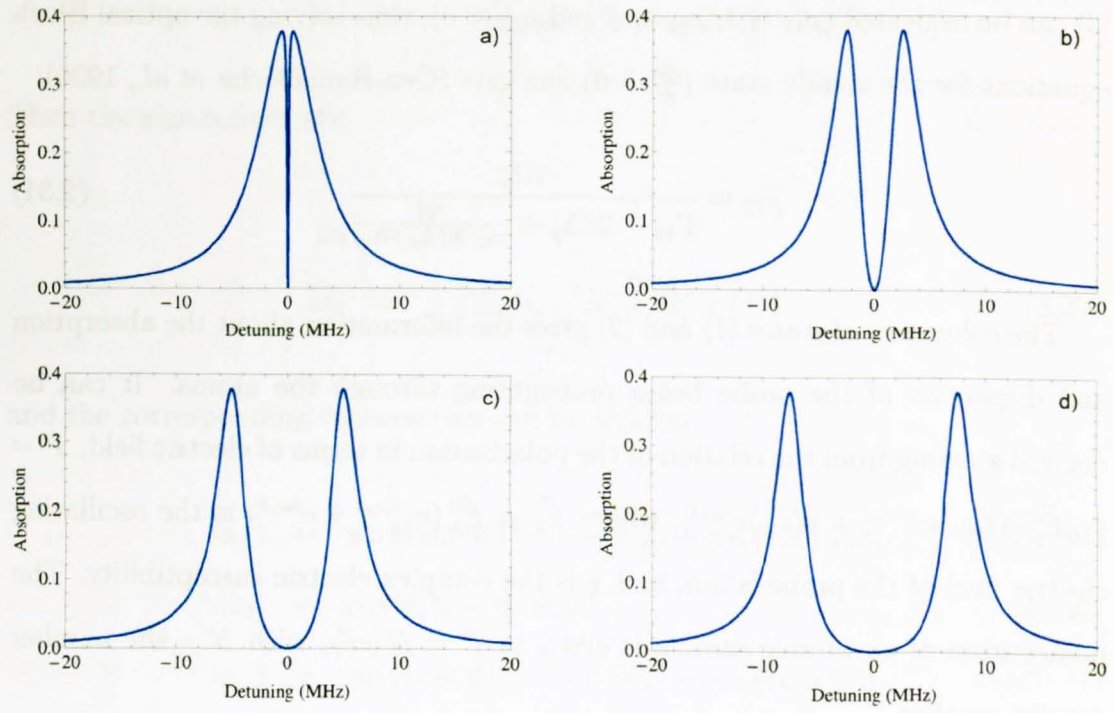

Figure 2.5: Effect of the Rabi frequency of coupling field on the EIT. (a) $\Omega_c = 1$ MHz, (b) $\Omega_c = 5$ MHz, (c) $\Omega_c = 10$ MHz, (d) $\Omega_c = 15$ MHz.

frequency. As the figures show, transparency occurs at resonance, i.e. when both lasers are tuned to $|1\rangle \rightarrow |2\rangle$ and $|2\rangle \rightarrow |3\rangle$ transitions respectively and the medium becomes transparent under the action of the strong coupling field. The different graphs show the absorption of the probe for different intensities of the coupling beam and indicate that the splitting of the two peaks increases with Ω_c. This splitting, called the Autler-Townes (AT) splitting (Autler and Townes, 1955), is in fact proportional to the effective Rabi frequency:

$$\Delta = \sqrt{\Omega_p^2 + \Omega_c^2}. \tag{2.35}$$

Autler-Townes splitting arises from the fact that the strongly coupled system is now described by a new set of basis states $|a_\pm\rangle$, and it is visible when the Rabi frequency of the coupling field is greater then the natural linewidth of the probe transition. Recently, Abi-Salloum (2010) investigated the differences between the EIT and AT regime. It was shown that there is a threshold for the coupling Rabi frequency, $\Omega_t = \gamma_{21} - \gamma_{31}$, that distinguishes between those two phenomena. This threshold for Ω_c separates two regimes: weak and strong coupling field. For the ladder system discussed in here, if the Rabi frequency of the coupling field is smaller then Ω_t, the nature of the dip in the spectrum is a result of destructive interference of the two resonances. However, for the Rabi frequency greater then the threshold the absorption profile is the sum of the two resonances separated by the AT splitting given by eqn. 2.35, and the observed dip is the gap between those resonances. Thus, for the strong coupling field regime the nature of the phenomenon is characteristic for the AT effect, while for a weak coupling field the dip is the signature of EIT. For the profiles presented in the figure 2.5 $\Omega_t = 3$ MHz (as $\gamma_{21} = \frac{1}{2}\Gamma_{21} \simeq 3$ MHz, $\gamma_{31} = 0$), so graph a) presents EIT phenomenon, while the others, b)–d), the AT regime.

The splitting of the peaks gives information about the Rabi frequency of the $|2\rangle \rightarrow |3\rangle$ transition, and therefore describes its nature. From the splitting, Ω_c

can be determined and therefore the strength of the $|2\rangle \rightarrow |3\rangle$ transition can be measured. This can be used to determinate the dipole moments of transitions, as presented in chapter 5.

In the previous paragraphs the decoherence of state $|3\rangle$, γ_3, was neglected, however in practice γ_3 is finite as decoherence takes place in the real system. The influence of γ_3 on the shape of the EIT signal is shown in figure 2.6. As could be expected, the increase of decoherence has a great impact on the shape of the absorption profile, as EIT and AT are a coherent processes. The increase of γ_3 causes the decrease of the transparency at the resonance and the transparency window becomes shallower from almost full transparency for $\gamma_3 = 1$ MHz, to only about 20% depth for $\gamma_3 = 10$ MHz. Also the maximum amplitude of the absorption signal decreases with higher values of γ_3 by the factor of 1.8 for the above values of γ_3.

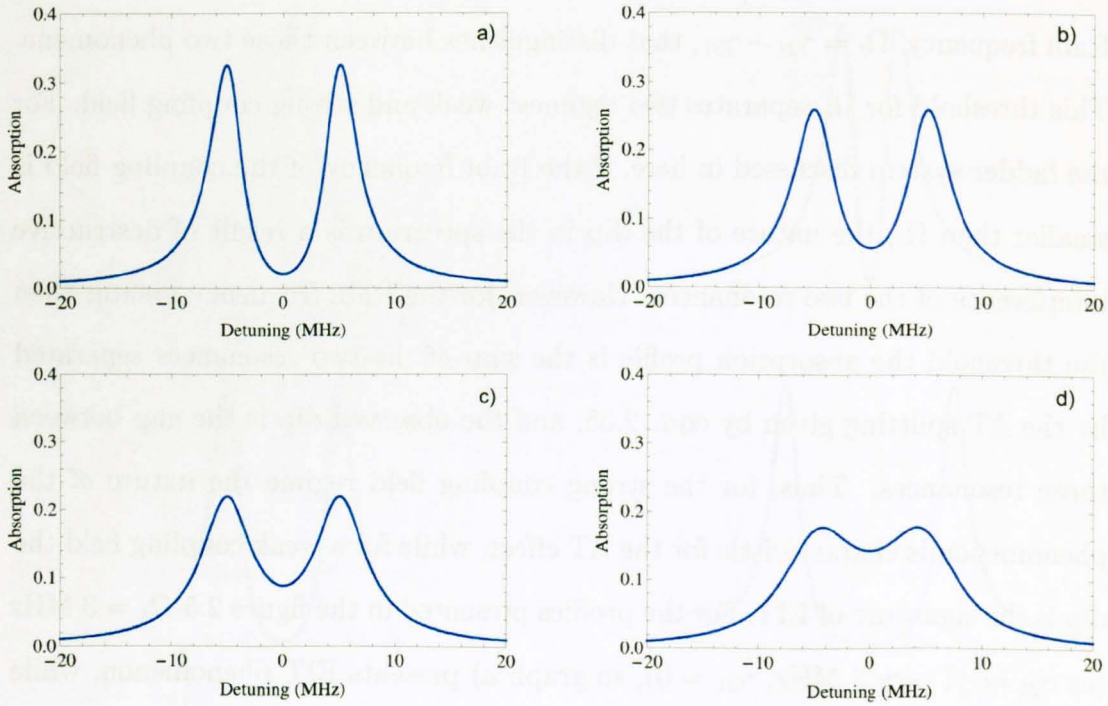

Figure 2.6: Effect of the dephasing of the state $|3\rangle$ on the EIT. $\Omega_c = 10$ MHz, (a) $\gamma_3 = 1$ MHz, (b) $\gamma_3 = 3$ MHz, (c) $\gamma_3 = 5$ MHz, (d) $\gamma_3 = 10$ MHz.

The influence of γ_3 on the depth of the transparency dip can be seen by putting $\Delta_p = 0$ and $\Delta_c = 0$ in 2.31. The imaginary part of the susceptibility is then proportional to γ_3:

$$\chi_{Im}\left(\Delta_p = 0, \Delta_c = 0\right) \propto \frac{\gamma_3}{\Gamma_{12}\gamma_3 + \Omega_c^2}. \tag{2.36}$$

It can also be seen that transparency increases with the increasing intensity of the coupling light even in the presence of decoherence.

Understanding of EIT lineshape, especially the influence of Ω_c and γ_3, is a key point for the analysis of the data measured in this thesis, as will be demonstrated in chapter 5.

CHAPTER 3

Rydberg Atoms

3.1 Properties of Rydberg atoms

Rydberg atoms are atoms in highly excited electronic states, very close to the ionisation limit. This gives them extraordinary physical properties. The first observations of Rydberg atoms were made by Balmer at the end of the 19th century with his discovery of the visible series of atomic hydrogen and the relationship between the principal quantum number, n, and measured wavelengths, λ,

$$\lambda = \frac{bn^2}{n^2 - 4}, \tag{3.1}$$

where $b = 3645.6$ Å. It was later Hartley, who had realised that the frequencies of transition are key to understanding the series of other atoms by rewriting Balmer's formula in terms of wave numbers ($\nu = 1/\lambda$) (Hartley, 1883)

$$\nu = \frac{4}{b}\left(\frac{1}{4} - \frac{1}{n^2}\right), \tag{3.2}$$

which shows that series are linked to energy differences between the $n = 2$ and higher states. Following those works Rydberg started to classify the spectra of other atoms (alkali atoms) into different series (*s*harp, *p*rincipal and *d*iffuse) with a single formula

$$\nu_\ell = \nu_{\mathrm{inf}\,\ell} - \frac{Ry}{(n-\delta_\ell)^2}, \tag{3.3}$$

where $Ry = 109721.6\ \mathrm{cm}^{-1}$ is the Rydberg constant, universal for different atoms, $\nu_{\mathrm{inf}\,\ell}$ is the series limit, δ_ℓ is the quantum defect and $\ell = s, p, d$. The Rydberg constant can be calculated using Bohr's theory of atoms

$$Ry = \frac{Z^2 e^4 m_{el}}{2(4\pi\epsilon_0)^2\hbar^2}. \tag{3.4}$$

Two important properties of highly excited states can be deduced from the classical Bohr theory: the binding energies of those states have n^{-2} dependance and the orbital radii increase as n^2:

$$E_{bind} = \frac{Ry}{n^2}, \tag{3.5}$$

$$r = n^2 \frac{(4\pi\epsilon_0)\hbar^2}{Ze^2 m_{el}}. \tag{3.6}$$

This means that atoms in high n Rydberg states have a weakly bound valence electron and its most probable distance from the atomic core is large. Other properties of Rydberg atoms are extraordinary in comparison with the ground state, and they are listed in Table 3.1.

The wave functions of Rydberg atoms can be obtained by solving the Schrödinger's equation. It is convenient to use atomic units, which are defined so that all parameters for the ground state of hydrogen atom have magnitude one. To obtain the Rydberg atom's wave functions it is convenient to start from the

property of Rb atom	$(n^*)^x$	$Rb(60d)$
binding energy, meV	$(n^*)^{-2}$	3.96
energy spacing $(E_n - E_{n-1})$, meV	$(n^*)^{-3}$	0.13
GHz		33.5
orbital radius, a_0	$(n^*)^2$	5156
geometric cross section, a_0^2	$(n^*)^4$	8.36×10^7
polarisability, MHz/(V/cm)^2	$(n^*)^7$	191
radiative lifetime, μs	$(n^*)^3$	215

Table 3.1: Properties of Rydberg atoms. Dependence on the effective principal quantum number was taken from Gallagher (1994). To calculate the values for the rubidium $60d$ state n^* were obtained using quantum defects from formula 3.11. The formula for radiative lifetime can be obtained from fit to theoretical calculations (Gallagher, 1994) and for d-states of rubidium it is $2.09(n^*)^{2.85}$.

time-dependent Schrödinger's equation for hydrogen atom

$$\left(-\frac{\nabla^2}{2\mu} - \frac{1}{r}\right)\psi = E\psi, \tag{3.7}$$

with E being the energy of state ψ, r the distance of the electron from the core and μ the reduced mass of the core and electron. The wave function ψ can be separated into radial, $\frac{1}{r}U_{n\ell}(r)$, and spherical terms as the Coulomb potential is purely radial $(1/r)$, where the spherical part is expressed using spherical harmonics, $Y_{\ell m}(\theta,\phi)$:

$$\psi = \frac{1}{r}U_{n\ell}(r)Y_{\ell m}(\theta,\phi). \tag{3.8}$$

The position of the electron is given in spherical coordinates r, θ and ϕ. This allows to separate the equation 3.7 into the angular and radial parts. This separation leads to the radial part of the equation:

$$\left(-\frac{1}{2\mu}\frac{d}{dr^2} - \frac{1}{r} + \frac{\ell(\ell+1)}{2\mu r^2}\right)U_{n\ell}(r) = EU_{n\ell}(r), \tag{3.9}$$

where ℓ is a positive integer. Solving the above equation for bound states of hydrogen atom, i.e. $E < 0$ with boundary conditions for $U_{n\ell}$ yields the expression for the allowed energies:

$$E = -\frac{1}{2n^2}. \tag{3.10}$$

The detailed calculation can be found in any quantum mechanics textbook; they are also shown in Gallagher (1994).

The Rydberg atom can be treated as a hydrogen atom, as the core electrons effectively shield the valence electron from the electric field of the nucleus. However, the core still has some influence on the valence electron and the quantum defect allows to correct the principal quantum number of alkali atoms due to this influence. When an electron is far away from the atomic core it sees it as a net positive charge $+e$. However, when it comes closer to the core, the fact that this is not a point-like particle means that the electron can penetrate or polarise the core (see figure 3.1). The quantum defect therefore depends very highly on the ℓ state of electron. For states that deeply penetrate the core, like s and p, quantum defects are significant, while configurations for f and higher angular momentum are almost hydrogen-like, so the quantum defects are close to 0 (Gallagher, 1994). For rubidium the values of quantum defect are (Li *et al.*, 2003; Lorenzen and Niemax, 1983): $\delta_s = 3.13$, $\delta_p = 2.65$, $\delta_d = 1.35$. The quantum defects depend also slightly on the principal quantum number n, and they can be expressed by the following formula

$$\delta_\ell(n) = a + \frac{b}{(n-a)^2} + \frac{c}{(n-a)^4} + \frac{d}{(n-a)^6} + \ldots, \tag{3.11}$$

where the coefficients a, b, c, d... are tabulated e.g. in Lorenzen and Niemax (1983). Due to the penetration of the core the potential seen by the valence electron is deeper then the Coulomb potential, but it is still assumed to depend

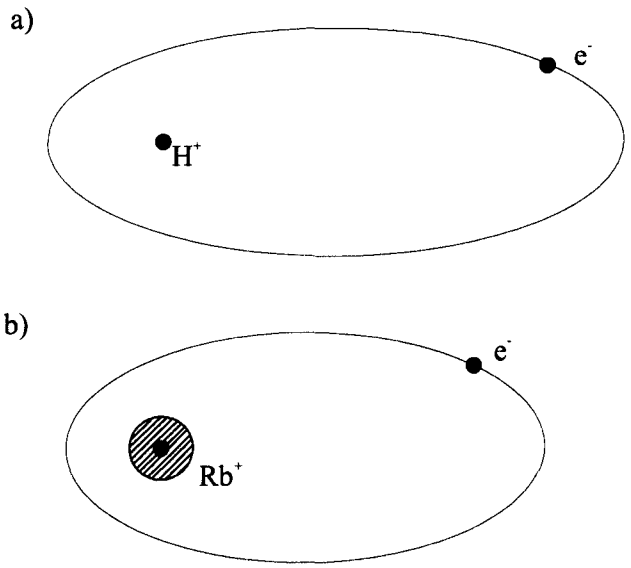

Figure 3.1: Representation of Rydberg states for a) H and b) Rb. In H the electron orbits around the point of charge of the proton. In Rb it orbits around the +37 nuclear charge and 36 inner shell electrons. In the high ℓ states Rb behaves identically to H, but in low ℓ states the Rb electron penetrates and polarises the inner shell electrons of the Rb^+ core. (Gallagher (1994)).

only on r, thus wave functions for alkali atoms differ only in radial function from the hydrogenic wave functions. The analysis of the influence of the change in the potential can be found in Gallagher (1994), and it allows the energy of Rydberg levels in rubidium to be rewritten as

$$E_\ell(n) = E_i^{Rb} - \frac{Ry^{Rb}}{(n-\delta_\ell)^2} \tag{3.12}$$

with $Ry^{Rb} = 109736.605\,\mathrm{cm}^{-1}$ and the ionisation energy $E_i^{Rb} = 33690.798(2)\,\mathrm{cm}^{-1}$ (Lorenzen and Niemax, 1983). The comparison of the energy levels of rubidium and hydrogen is presented in figure 3.2. For states with lower ℓ the differences of the energy levels in rubidium and hydrogen are significant. The low n states for s, p and d cannot be treated as Rydberg states and formula 3.12 cannot be used to calculate their energies. The literature data from NIST database were used in

the graph instead (Ralchenko *et al.*, 2008). For higher n the effect of quantum defect is clearly visible, e.g. for s state the quantum defect is close to 3 and so the energy of $n = 8$ in rubidium atom is very close to the energy of hydrogen's $n = 5$ state.

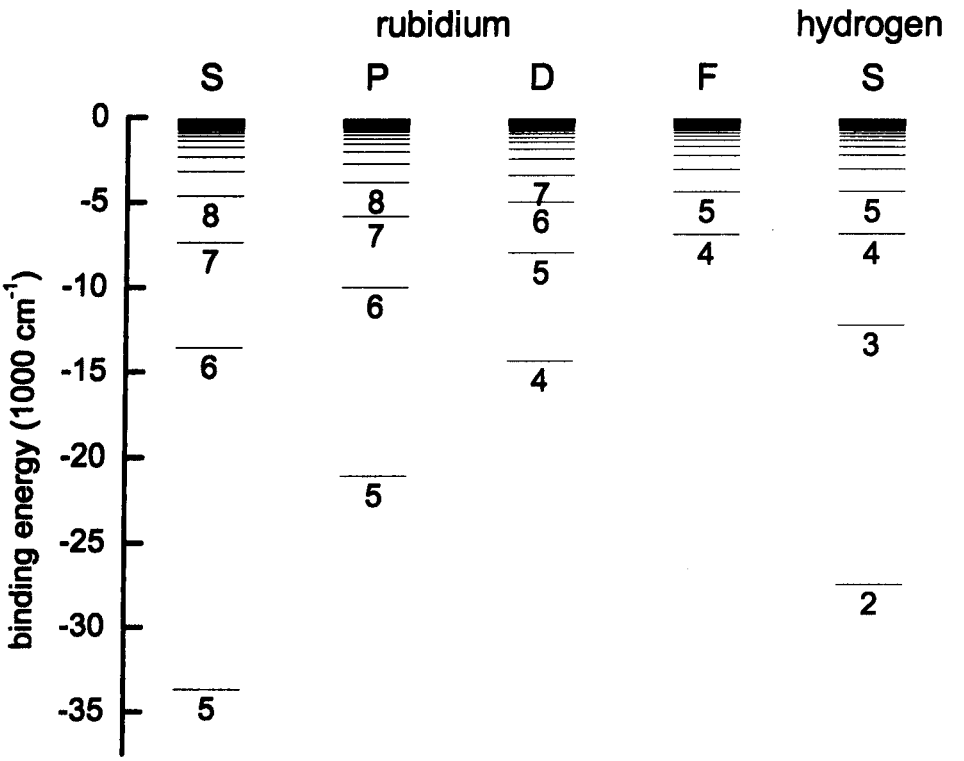

Figure 3.2: Energy levels of rubidium and hydrogen. The numbers below the levels indicate the principal quantum number n. For high n the energy values are calculated using equation 3.12, for low n they are taken from tables (Ralchenko *et al.*, 2008).

The wave functions for Rydberg states can be calculated numerically by solving the Schrödinger's equation with the modified potential. Calculations of the radial wave functions of Rydberg states allow to calculate the matrix elements between those states. This can give information about the properties of Rydberg atoms. Using the combination of radial matrix elements and the energies of the states it is possible to obtain the scaling properties as a function of the effective quantum number, n^*, as listed in table 3.1. For instance the polarisability of the

atom comes from the atom's response to an electric field. Using second order perturbation theory (Stark effect), one can show that it is the sum of squares of electric dipole matrix elements ($\mu_{nn'}$) divided by the energy difference:

$$\alpha_{nn'} = -2\sum \frac{|\mu_{nn'}|^2}{E_{\ell'}(n') - E_{\ell}(n)} \tag{3.13}$$

The dipole matrix elements between neighbouring states scale with n^2 and the energy difference as n^{-3}, thus the polarisability has an n^7 dependence. This strong dependance on n means that Rydberg atoms are very sensitive to electric fields. Another useful property of Rydberg atoms is their lifetime. Rydberg states are very long-lived, the lifetime for a given state scales with n^3. As an example, for $n = 60d$ the radiative lifetime is of the order of 200 μs, which makes them ideal system for experimental investigation. Furthermore, the ionisation energies of such states are very small (about 4 meV for $n = 60$ while for rubidium ground state it is 4.2 eV) so Rydberg atoms can very easily be ionised using an electric field, which gives a perfect tool for detection of Rydberg atoms.

3.2 Interactions in a gas of Rydberg atoms

In the previous chapter the interaction of Rydberg atoms with light was described, but one of the facts, why Rydberg atoms became such an interesting topic of research, are the interactions between Rydberg atoms. Because of their high polarisability, Rydberg atoms are very sensitive to external perturbations, even those caused by nearby Rydberg atoms, e.g. for rubidium in $n = 79D$ state the interactions can be seen between atoms separated by 11μm (Urban *et al.*, 2009). In this section some properties of those interactions will be presented.

3.2.1 Dipole interactions of two atoms

The interaction energy of two classical dipole moments $\vec{\mu}_1$ and $\vec{\mu}_2$ is given by

$$E = \frac{\vec{\mu}_1 \cdot \vec{\mu}_2}{|\vec{R}|^3} - 3\frac{\left(\vec{\mu}_1 \cdot \vec{R}\right)\left(\vec{\mu}_2 \cdot \vec{R}\right)}{|\vec{R}|^5} \tag{3.14}$$

where $\vec{R}$ is the distance vector between the two dipoles (Gallagher, 1994). The dipole moment is represented as a dipole matrix element, $\vec{\mu} = \langle\phi_1|e\vec{r}|\phi_2\rangle$, between the two states $|\phi_1\rangle$ and $|\phi_2\rangle$, and the interaction energy between two atoms is:

$$V_{dd} \propto \frac{1}{R^3}\sum_{|\phi_1\rangle,|\phi_2\rangle}\langle\phi_1|\mu_1|\phi_1'\rangle\langle\phi_2|\mu_2|\phi_2'\rangle = \sum_{|\phi_1\phi_2\rangle}\left\langle\phi_1\phi_2\left|\frac{\mu_1\mu_2}{R^3}\right|\phi_1'\phi_2'\right\rangle. \tag{3.15}$$

The interaction can be described using the model consisting of three Rydberg states $|r_p\rangle$, $|r_s\rangle$ and $|r_{s'}\rangle$, where s and p denote different angular momenta (see figure 3.3a). The two atoms are initially in the state $|r_p\rangle$ and the energy difference between this state and two nearby states (r_s and $r_{s'}$) is large. However, when the two-particle states, $|r_p r_p\rangle$ and $|r_s r_{s'}\rangle$ or $|r_{s'} r_s\rangle$, are considered the difference

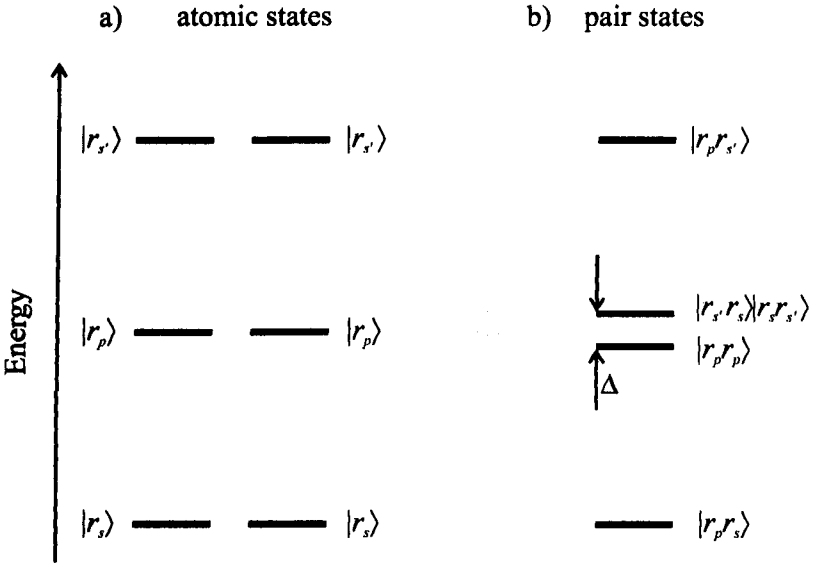

Figure 3.3: a) Single-atom energy levels for two atoms b) two-atom energy levels. Δ is the energy difference between the $|pp\rangle$ and $|ss'\rangle/|s's\rangle$ states.

between two particle states is Δ and they are almost degenerate (see figure 3.3b). The dipole matrix elements between $|r_p\rangle$ and $|r_s\rangle$ and between $|r_p\rangle$ and $|r_{s'}\rangle$ are non-vanishing, whereas the one between $|r_s\rangle$ and $|r_{s'}\rangle$ is vanishing. Thus the only two-particle states to be considered are the ones that have a non-vanishing dipole-dipole interaction with the $|r_p r_p\rangle$ state that are closest in energy: $|r_s r_{s'}\rangle$ and $|r_{s'} r_s\rangle$. The Hamiltonian takes the form:

$$\mathcal{H} = \mathcal{H}_0 + \mathcal{H}_{int} = \begin{pmatrix} -\Delta & \frac{\mu_1\mu_2}{R^3} \\ \frac{\mu_1\mu_2}{R^3} & 0 \end{pmatrix} \tag{3.16}$$

where $\mathcal{H}_0$ is the atomic Hamiltonian, and $\mathcal{H}_{int}$ the interaction. The energy levels of the system are:

$$E_\pm = -\frac{\Delta}{2} \pm \sqrt{\left(\frac{\Delta}{2}\right)^2 + \left(\frac{\mu_1\mu_2}{R^3}\right)^2} \tag{3.17}$$

and for the zero detuning ($\Delta = 0$) the energies of the two new states $|+\rangle$ and $|-\rangle$ are split by $2\mu_1\mu_2/R^3$.

For most atomic systems the energy difference Δ is non-zero. For the case of large detuning, $\Delta \gg \frac{\mu_1\mu_2}{R^3}$, Taylor expansion of 3.17 leads to an energy shift of the state $|r_p r_p\rangle$ of

$$\Delta E_{|r_p r_p\rangle} = \frac{(\mu_1\mu_2)^2/\Delta}{R^6}. \tag{3.18}$$

This is the van der Waals interaction energy. As $\mu \propto n^2$ and $\Delta \propto n^{-3}$ the scaling of the van der Waals coefficient, C_6, is $C_6 = (\mu_1\mu_2)^2/\Delta \propto n^{11}$. Depending on the sign of the energy difference to the nearest coupled pair state the interaction can be either attractive or repulsive.

If the energy difference approaches zero, $\Delta \ll \frac{\mu_1\mu_2}{R^3}$, the system exhibits a pair state resonance, called a Föster resonance in analogy to Föster resonances in biological systems, where dipole-dipole coupling between molecules is responsible

for radiation-less energy transfer. In this case equation 3.17 reduces to

$$E_{\pm} = \pm\frac{\mu_1\mu_2}{R^3} = \pm\frac{C_3}{R^3}. \tag{3.19}$$

The interaction energy depends on the distance as R^{-3} and in experiments with alkali atoms, such a situation can be achieved for certain settings of the external electric field. There exist also some states, which are almost degenerate at zero electric field, e.g. $58d_{3/2}$, $58d_{3/2}$ and $60p_{1/2}$, $56f_{5/2}$ for rubidium (Walker and Saffman, 2008).

3.2.2 Local dipole blockade

If the excitation to a Rydberg state is now considered, the strong dipole-dipole interactions can cause energy levels to shift and prevent the excitation of more then one atom to Rydberg states in an atomic ensemble by a narrow bandwidth laser beam. This phenomenon is called *dipole blockade* and was first proposed for Rydberg atoms by Lukin *et al.* (2001). To explain the blockade effect two individual atoms, held close enough to have a strong interaction, are considered. The ground state, $|g\rangle$, and Rydberg state, $|r\rangle$, are separated by energy E. The system can be described in terms of number of excitations it holds, so when both atoms are in ground state ($|gg\rangle$) they can be excited by a laser of Rabi frequency Ω to a state where one atom is in Rydberg state ($|rg\rangle$ or $|gr\rangle$), as is shown in figure 3.4. There are two situations to be considered. For non-interacting atoms, i.e. separated far enough away one from another, the two-atom spectrum exhibits two transitions at the same frequency $E/\hbar$, so excitation ends with a double-excited state $|rr\rangle$. However, when the atoms are separated from each other by the distance closer then the blockade radius, R_b, a strong interaction can occur, which shifts the energy of $|rr\rangle$ by an amount ΔE and a narrow-band laser excitation cannot bring the two atoms to state $|rr\rangle$. As a consequence of such a blockade the atoms

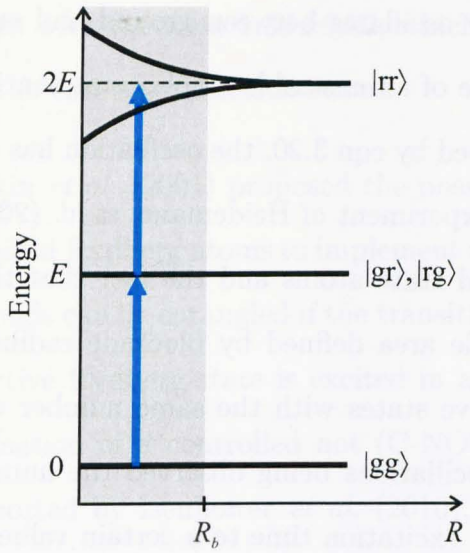

Figure 3.4: Principles of the Rydberg blockade between two atoms separated by a distance R. If atoms are closer then blockade radius R_b the narrow-band laser cannot excite double-excited state $|rr\rangle$.

are excited into the entangled state $|\Psi_+\rangle = \frac{1}{\sqrt{2}}\left(e^{i\vec{k}\cdot\vec{r}_1}|rg\rangle + e^{i\vec{k}\cdot\vec{r}_2}|gr\rangle\right)$ where $\vec{r}_1$ and $\vec{r}_2$ are the positions of the two atoms and $\vec{k}$ is the wave vectors of the exciting laser field. In general, for N atoms the so-called collective state is given by

$$|\Psi_+\rangle = \frac{1}{\sqrt{N}}\sum_{i=1}^{N} e^{i\vec{k}\cdot\vec{r}_i}|g, g, \ldots, r, \ldots, g\rangle. \tag{3.20}$$

In this system only one atom can be transferred into a Rydberg state but as the light is coherent over the extent of the atoms it is not possible to tell which atom is excited. Thus, the whole system is sharing one single excitation.

The first experimental evidence of suppression of excitation due to the local blockade effect was given by Singer *et al.* (2004), where the number of atoms excited to Rydberg states for a high-density atomic cloud was significantly smaller than expected if no blockade mechanism would occur. Later, the blockade effect was also reported in cold caesium atoms at Föster resonances (Vogt *et al.*, 2007) and the evidence of collective excitation of Rydberg atoms in a MOT were observed by Heidemann *et al.* (2007). A single atom exposed to a resonant ex-

citation light coherently oscillates between ground and excited state with Rabi frequency Ω. In the case of an ensemble of N atoms sharing one excitation, like the collective state defined by eqn 3.20, the oscillation has the collective Rabi frequency $\sqrt{N}\Omega$. In the experiment of Heidemann *et al.* (2007) the inhomogeneity of the density of ground state atoms and the fact that the excitation area was larger than the blockade area defined by blockade radius, R_b, prevented them from producing collective states with the same number of atoms. This caused that instead of Rabi oscillations being observed the number of Rydberg atoms detected saturates with excitation time to a certain value which depends on the density.

The first direct observation of Rydberg blockade was presented in 2009 by the group of Walker and Saffman (Urban *et al.*, 2009) and Grangier's group (Gaëtan *et al.*, 2009). In both cases the blockade was observed between two single neutral atoms. Urban *et al.* (2009) reported the Rydberg blockade at the distance of 11 μm in ultracold ^{87}Rb atoms excited to the $79D_{5/2}$ state. In the experiment the two single atoms were loaded into two dipole traps and one of them, the control atom, was excited to the Rydberg state. If the control atom was excited into Rydberg state, the other atom, the target, could not hold an extra excitation due to the blockade effect. Their results showed that the presence of Rydberg atom in the control site indeed reduces the probability of populating the Rydberg state in the target site.

On the other hand, Gaëtan *et al.* (2009), focused on the observation of the collective two-atom behaviour. The two atoms were also held in two dipole traps, separated by a distance of $\sim$4 μm. The Rydberg state used in their experiment was $58D_{3/2}$. Here the suppression of probability to excite both atoms to Rydberg state was also seen. To observe the collective state excitation they measured the Rabi oscillations of only one atom excited to the Rydberg state in two situations: when the second dipole trap was occupied and empty. Those two Rabi oscillations

had different frequencies with the ratio 1.38 ± 0.03, which is compatible with the expected ratio $\sqrt{2}$ for the two-atom collective state.

In their article, Lukin *et al.* (2001) proposed the possibility of exploiting the dipole blockade in ultracold Rydberg atoms to implement a quantum gate. Qubits stored in two atomic clouds can be entangled if the transitions in one ensemble are inhibited when a collective Rydberg state is excited in a second ensemble. The first experimental realisation of a controlled not (C-NOT) gate using Rydberg atoms was recently reported by Isenhower *et al.* (2010). In a C-NOT gate the result of the target bit depends on the value of the control bit. If the control bit is 1 the target bit is flipped, otherwise it stays unchanged. They excited a control atom to a Rydberg level with principal quantum number $n = 90$, which prevented subsequent excitation of a target atom in a neighbouring site separated by $R = 10$ μm.

The observation of light-atom interactions, like electromagnetically induced transparency, can also give insight into the interactions between Rydberg atoms. Tauschinsky *et al.* (2010) observed the distance dependent shifts of the Rydberg levels of atoms excited near the surface of an atom chip.

As mentioned before Rydberg atoms are very easy to ionise. Rydberg atoms can therefore be detected easily by the state-selective electric field ionisation (SFI). This technique makes the use of the fact that each Rydberg state has a different ionisation energy, so by applying a particular electric field only atoms in a states above a suitable threshold will be ionised. If the field is ramped atoms in different states will be ionised at different times. Detection of electrons striped out from the atoms by time-of-flight technique can then give information not only on which Rydberg states were excited, but also what was the initial position of the corresponding Rydberg atom, as was firstly presented by van Ditzhuijzen *et al.* (2006, 2008). If two atoms placed at different distances from the detector

after the ionisation pulse they will reach the detector in the different time, which enables to calculate the initial position of the atoms.

In 2002 Boisseau *et al.* predicted that two Rydberg atoms can form molecules. They called those ultralong range molecules *macrodimers* with equilibrium distances of many thousands of Bohr radii. It was shown that, for some molecular symmetries, interaction between two Rydberg atoms can lead to creation of the potential wells supporting several bounding states and they also proposed an experimental way to detect such molecules. De Oliveira *et al.* (2003) showed experimental agreement with calculations made by Boisseau *et al.* (2002) that suggest the existence of such ultralong range potentials. Farooqi *et al.* (2003) presented the evidence for molecular resonances in a cold dense gas of rubidium Rydberg atoms, but again this was made in a regime of a large number of Rydberg atoms. Liu and Rost (2006) investigated a different type of molecules, ultralong-range polyatomic molecules formed with a Rydberg atom and several ground-state atoms. The length of the molecular bond in such molecules is of the order of $n^2 a_0$, where n is the principal quantum number of the Rydberg electron and a_0 is the Bohr radius. The first spectroscopic observation of molecules created from bonding the Rydberg electron with a ground-state atom was presented by Bendkowsky *et al.* (2009). Molecular states were formed by rubidium Rydberg atoms in the spherically symmetric s state with principal quantum numbers $n = 34$ to 40.

The experiments at the Open University aim to investigate the strong interactions between Rydberg atoms in the regime of high densities and small, controllable number of atoms stored in the dipole trap. In this thesis the interaction with light in the EIT/AT experiment is presented, and future experiments aim to deal with direct observation of collective excitation in such a small ensemble.

CHAPTER 4

The Experimental Apparatus

In this chapter a description of the experimental apparatus used for the production of ultracold Rydberg atoms will be presented. It is noteworthy that at the start of the PhD of the author the laboratory was literally empty, hence most of the apparatus described here was designed and assembled by the author as part of his PhD project (see figure 4.1). A new state-of-the-art facility was built for experiments in cold Rydberg atoms which will be described in the following sections.

The first goal was to produce a source of cold rubidium atoms using well-known laser cooling techniques; principles of operation of laser cooling and magneto-optical trapping as well as the experimental implementation will hence be described in detail. Particular emphasis will be placed on the techniques used to narrow the natural emission line shape and the fine control of the frequency tuning of the laser sources. Experiments carried out to test and characterise the cold atomic sample will be presented in section 4.3. The last two sections will present the two-photon excitation scheme implemented to obtain Rydberg states, with a detailed description of the frequency stabilisation of the lasers exploiting the electromagnetically induced transparency spectrum.

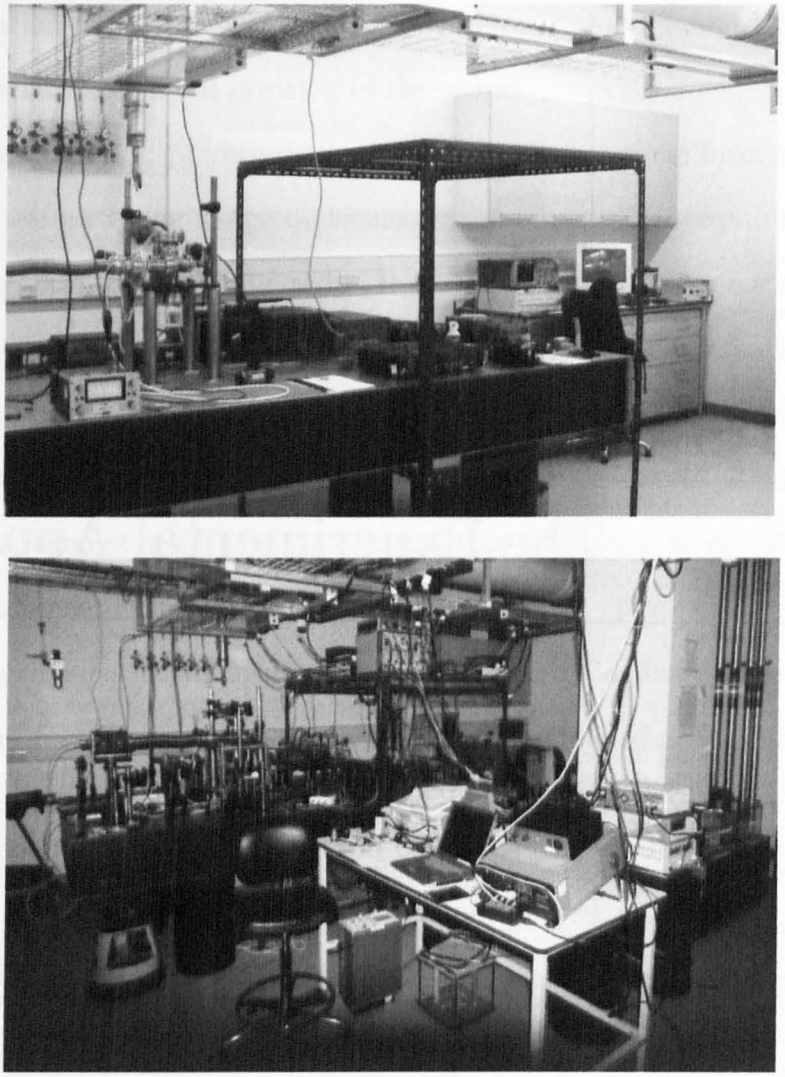

Figure 4.1: Photographs of the laboratory: December 2006 (top) and December 2009 (bottom).

4.1 Laser cooling and trapping

In this section an overview of the basic principles of laser cooling for neutral atoms will be given. Radiation pressure can be used to cool down moving atoms by exploiting the Doppler effect, as first proposed by Hänsch and Schawlow (1975). Other mechanisms of cooling rely on the presence of polarisation gradients and leads to sub-Doppler temperatures. A description of the magneto-optical trap will also be presented, which provides not only cooling of the atoms but also their confinement, so that higher atomic densities can be achieved.

4.1.1 Radiation pressure force

When the atom interacts with the near-resonant light it experiences a radiation pressure force due to momentum transfer during processes of absorption followed by spontaneous emission of photons. The photon carries momentum $\hbar\vec{k}$, which is transferred to the atom while the photon is absorbed. Eventually, a photon is emitted in a spontaneous emission process, but this process is isotropic, so there is no preferred emission direction. As a result, averaging over many cycles of photon absorption and emission, no net momentum is gained from the spontaneous emission process. The force resulting from multiple scattering processes is given by $\vec{F}_{scatt} = n\hbar\vec{k}$, where n is the number of scattered photons per unit time, the scattering rate, and is given by eqn 2.23, thus

$$F_{scatt} = \hbar k \frac{\Gamma}{2} \frac{I/I_{sat}}{1 + I/I_{sat} + 4\delta^2/\Gamma^2}, \tag{4.1}$$

where δ is the detuning of the light from the resonance, typically of the order of Γ.

4.1.2 Optical molasses and the Doppler cooling limit

Let one consider an atom moving with a velocity $\vec{v}$ towards the photon that is *red* detuned from the resonance (i.e. it is tuned below the resonance frequency), as in figure 4.2. In the situation where the atom is moving the Doppler shift also has to be taken into account. The Doppler shift for a moving atom gives a detuning of kv, so the total detuning of the laser light from the atomic transition is $\delta = \omega - \omega_{21} + kv$, where ω is the laser frequency.

From equation 4.1 it follows that the radiation pressure force strongly depends on the detuning from the resonance. If a pair of counter-propagating laser beams of equal intensity and at resonance frequency is considered, the forces exerted by the laser beams will be balanced only for stationary atoms, while for any moving

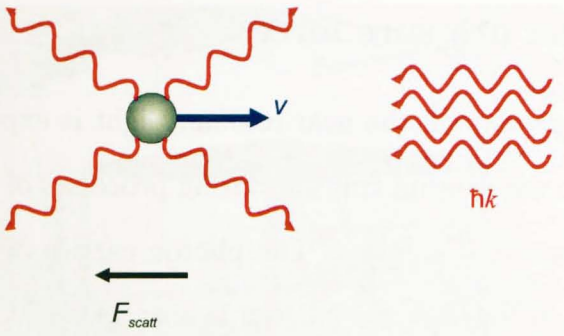

Figure 4.2: For an atom travelling towards the laser beam each absorbed photon reduces its momentum and scattered photons go in random directions, resulting in a force that slows down the atom.

atom the Doppler effect will shift the frequency 'seen' by the atom, which leads to an imbalance in the forces. In the situation when both lasers are red detuned, the atoms travelling towards the beam see the frequency of the light shifted towards resonance, and consequently, the atoms scatter more photons from this beam. At the same time the co-propagating beam is even more detuned from resonance which causes a decrease in the force it can impact on the atom. The total force, $F_{molasses}$, is given by

$$\begin{aligned} F_{molasses} &= F_{scatt}(\omega - \omega_0 - kv) - F_{scatt}(\omega - \omega_0 + kv) \\ &\simeq F_{scatt}(\omega - \omega_0) - kv\frac{\partial F}{\partial \omega} - \left(F_{scatt}(\omega - \omega_0) + kv\frac{\partial F}{\partial \omega})\right) \\ &= -2\frac{\partial F}{\partial \omega}kv \end{aligned} \tag{4.2}$$

in the limit of low velocities, $kv \ll \Gamma$. The force acting on the atoms due to a pair of counter-propagating beams is then frictional, $F_{molasses} = -\alpha v$, so the term *optical molasses* has been used for this technique (Chu *et al.*, 1985). The frictional coefficient is given by

$$\alpha = 2k\frac{\partial F}{\partial \omega} \simeq 4\hbar k^2 \frac{I/I_{sat}}{(1 + 4\delta^2/\Gamma^2)^2} \tag{4.3}$$

where I/I_{sat} in the denominator of 4.1 has been neglected as optical molasses are operated at intensities well below saturation ($I/I_{sat} \ll 1$).

The cooling by the radiation force is limited by the momentum transfer due to random scattering of photons by the atoms. This is called the Doppler cooling limit and the lowest temperature achievable in the optical molasses can be shown to be (Dalibard and Cohen-Tannoudji, 1989):

$$T_D = \frac{\hbar\Gamma}{2k_B}. \tag{4.4}$$

For rubidium the Doppler cooling limit is $T_D = 142\ \mu$K.

4.1.3 Sub-Doppler cooling

The first experiments in cooling and trapping of atoms showed that temperatures much lower then those predicted in the Doppler limit can be easily achieved (Lett *et al.*, 1988). It was evident that some other cooling process must be involved to justify these lower temperatures. The first explanation was proposed by Dalibard and Cohen-Tannoudji (1989) and it involves the so-called Sisyphus cooling that arises from optical pumping between different Zeeman sublevels associated with a polarisation gradient.

Sisyphus cooling can be understood by considering an atom with ground state hyperfine number $F = 1/2$ and excited state hyperfine number $F' = 3/2$ (figure 4.3a). In a 1-D optical molasses, formed by two counter-propagating beams with orthogonal linear polarisation π, the beams form a standing wave within which the polarisation varies with the position (see figure 4.3b). This produces spatial regions with different light shifts due to different Clebsch-Gordan coefficients for different polarisations, so a moving atom travels over potential hills and valleys. Kinetic energy is lost when the atom absorbs a photon at the top of the hill and emits a spontaneous photon of a higher energy and ends up in a valley.

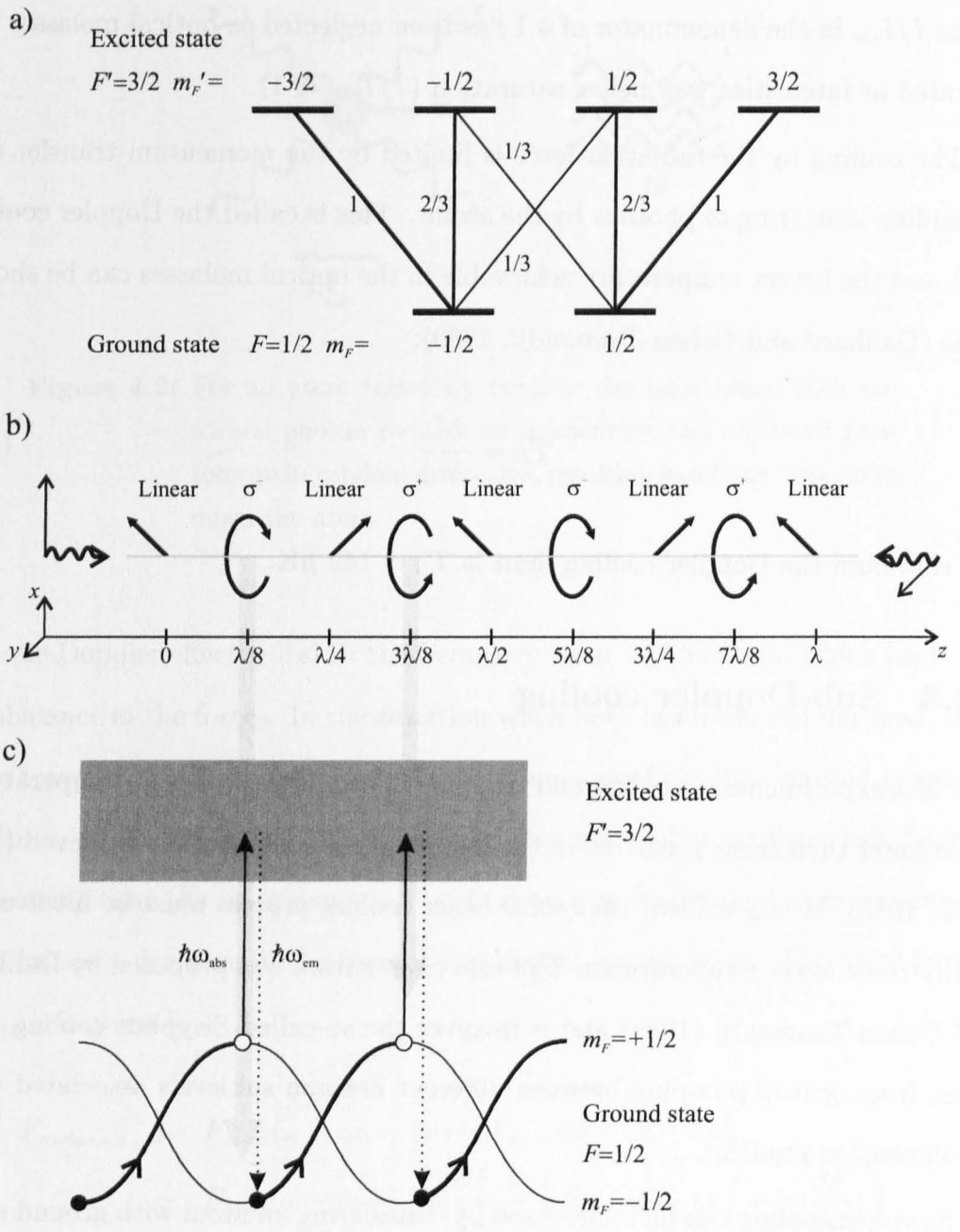

Figure 4.3: Details of Sisyphus cooling mechanism. a) The electric dipole transitions between two levels with angular momenta $F = 1/2$ and $F' = 3/2$ with relative strengths indicated for each transition. b) standing wave polarisation pattern – formed by two laser beams propagating along z with perpendicular polarisations (along x and y) c) ground state energy shifts and cooling mechanism. Atoms are travelling up and down hills and valleys in the potential energy. Kinetic energy is lost when the atom absorbs at the top of the hill and emits a spontaneous photon of a higher energy and ends up in a valley.

Here this process will be presented in more details. When atoms are moving along the axis of the laser beam they experience a spatially varying polarisation. The two ground state magnetic sublevels will also present spatially-varying light shift (see figure 4.3b,c). Furthermore, when the atoms move from a σ^- region to σ^+, the probability of being optically pumped to $m_F = +1/2$ increases and is maximum at pure σ^+. So when the atom in $m_F = -1/2$ travels in the $+z$ direction and starts climbing the potential hill at position $\lambda/8$ (see figure 4.3c), it is very likely to be optically pumped into $m_F = +1/2$ when it reaches the top of the hill at $3\lambda/8$. At this point some of the kinetic energy has been converted to potential energy which is now lost in emission. In each process the atom loses an energy approximately equal to the hight of the potential hill, which suggests that the Sisyphus cooling is acting until the moment when atoms have enough kinetic energy to climb the hill. It can be shown that the final temperature is related to the laser intensity, I, and detuning, δ:

$$T_S \propto \frac{1}{k_B}\frac{I}{|\delta|}. \tag{4.5}$$

Sisyphus cooling describes the situation in a configuration of linearly polarised beams, however, it also takes place in optical molasses created by three pairs of circularly polarised beams due to the complex 3-D standing wave pattern generated by those circularly polarised beams (Hopkins and Durrant, 1997).

4.1.4 Magneto-optic trap

Optical molasses are capable of cooling atoms, but they provide no confinement for the atoms and the density achievable is therefore very low. Pritchard *et al.* (1986) suggested that adding an inhomogeneous magnetic field and counter-propagating laser beams of opposite circular polarisations enables atoms confinement.

Using two coils with currents flowing in opposite directions (the anti-Helmholtz configuration) a quadrupole magnetic field can be generated. The magnetic field is zero at the centre of the crossing area of the beams and has a steep uniform gradient away from this centre. The magnetic field does not confine atoms by itself but causes an imbalance in the scattering force generated by the cooling beams due to a space-depending splitting of the the Zeeman substates. Because the magnetic field is linear the Zeeman effect causes the energy levels of states $m_J = \pm 1$ to shift linearly with the relative position of the atom from the centre of the trap. In a 1-D situation, as in Figure 4.4, where counter-propagating beams

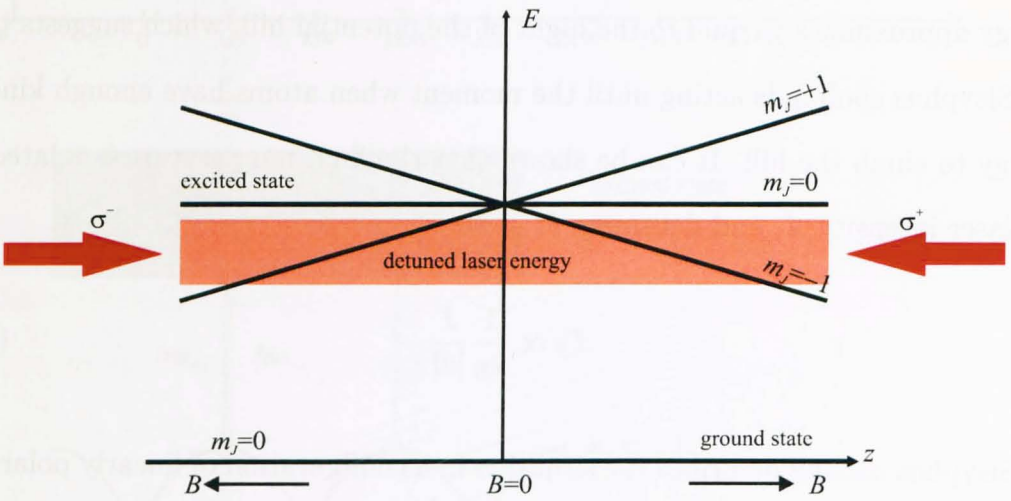

Figure 4.4: MOT's schematic representation showing the Zeeman shift and lasers configuration.

have circular polarisation and the laser frequency is red detuned from resonance, for an atom on the region to the right ($z > 0$) the $m_J = -1$ state is shifted closer to the resonance. However, due to selection rules, this transition is excited only by σ^+ polarisation so the scattering force (same as in molasses) pushes the atom towards the centre. A similar process occurs for atoms on the left side of the trap, this time, the $m_J = +1$ state is closer to the resonance, and transition is driven by σ^- light so atoms are again pushed towards $z = 0$. This mechanism

give rise to a restoring force $F_z = -\beta z$, where the spring constant, β, is given by

$$\beta = \frac{g_e \mu_B}{\hbar k} \frac{dB_z}{dz} \alpha \tag{4.6}$$

where g_e is the g-factor of the excited state and μ_B is the Bohr magneton. The total force acting on an atom in the z direction in the MOT is therefore

$$F_{MOT} = -\alpha v - \beta z. \tag{4.7}$$

To achieve a 3-D cooling and trapping a set of three pairs of molasses beams centred together with anti-Helmholtz coils is used. The magnetic field in the centre of the trap is therefore zero.

4.2 Cooling and trapping rubidium atoms

In the following paragraphs a description of the experimental setup implemented for laser cooling of rubidium atoms will be presented. The lasers used in the experiment will be described together with a discussion of the methods used to actively tune their frequency and reduce the linewidth. The following sections will present the realisation of a magneto-optical trap for rubidium atoms and its characterisation.

4.2.1 Cooling ^{87}Rb atoms: laser sources

^{87}Rb has nuclear spin $I = 3/2$ and the hyperfine interaction splits the levels in the eigenstates of the total angular momentum F, according to the scheme in figure 4.5. The lifetime of the first excited state is 26.23 ns, corresponding to a natural linewidth of of $\Gamma/2\pi = 6.065$ MHz (Gutterres *et al.*, 2002).

A typical laser-cooling experiment requires different laser sources tuned at different frequencies. In section 4.1.4 the magneto-optical trap principles were

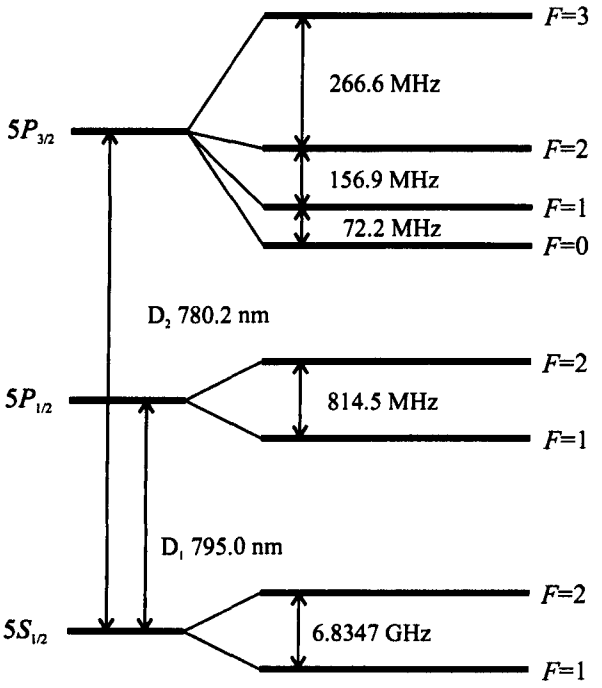

Figure 4.5: Scheme of the hyperfine structure for ^{87}Rb atom. Cooling transition for D_2 line is $5S_{1/2}$, $F = 2 \rightarrow 5P_{3/2}$, $F' = 3$, and repumping is done on $5S_{1/2}$, $F = 1 \rightarrow 5P_{3/2}$, $F' = 2$ transition.

described considering a two-level atomic system. In practice ^{87}Rb, and other alkali metals, are cooled by exploiting their hyperfine structure. The transition used to cool and trap the atoms of rubidium-87 is the D_2 $5S_{1/2}$, $F = 2 \rightarrow 5P_{3/2}$, $F' = 3$ at the wavelength of 780.2 nm, as shown in figure 4.5.

The selection rules allow only $\Delta F = 0, \pm 1$ dipole transitions, so if the laser is tuned to excite the $5S_{1/2}$, $F = 2 \rightarrow 5P_{3/2}$, $F' = 3$ hyperfine transition the excited state can decay only back to the $5S_{1/2}$, $F = 2$ state. Such a transition is closed, which means that the atoms circulate only between those two hyperfine states, $F = 2$ and $F' = 3$, so it resembles a two-level transition. However, there is still some finite probability of the laser coupling to the $5S_{1/2}$, $F = 2 \rightarrow 5P_{3/2}$, $F = 2$ transition, which will cause a decay to the state $5S_{1/2}\, F = 1$. If the atoms are transferred into this state, they do not interact with light anymore so after many cooling cycles all the population is transferred to $F = 1$. In order to avoid this and to repopulate the $5S_{1/2}$, $F = 2$ state, where the cycling transition is effective, an

extra laser needs to be added. This laser, called the repumper, is tuned to transfer atoms from $5S_{1/2}$, $F = 1$ to $5P_{3/2}$, $F = 2$, from which they can spontaneously decay back to $5S_{1/2}$, $F = 2$.

4.2.2 Grating-stabilised diode lasers

For the wavelength of 780 nm there are commercially available laser diodes, which are relatively cheap. However their linewidth needs to be narrowed and the frequency actively tuned. To achieve this a technique exploiting grating feedback and an extended cavity is used. The Sanyo DL-7140-201 diode lasers are set up with an external cavity, using a diffraction grating in the Littrow configuration, as shown in figure 4.6. The design of the cavity is based on the work by Arnold *et al.* (1998) with modifications by Hawthorn *et al.* (2001) and the implementation was made at the S&T Workshop at the OU.

Diode lasers are in fact very sensitive to optical feedback. The free-running laser has many different oscillation modes and the emission frequency is determined by the competition between those modes. With optical feedback one can increase the number of photons at a specific selected frequency, ω_f, therefore increasing the intensity at this frequency and thus forcing the laser to emit at ω_f, reducing the linewidth.

Presented here extended-cavity diode laser (ECDL) uses a diffraction grating to select the specific wavelength to be fed back. Figure 4.6 shows the scheme of the ECDL used in the lab. The beam from the laser diode goes through a collimation lens to the grating and the first order diffracted beam is retro-reflected to the diode whilst the zeroth order beam is reflected and used as output. The extended cavity, which is formed by the back facet of the diode and the grating, allows to select the wavelength of the laser beam at the frequency of the reflected beam. Increasing cavity length also allows for narrower emission linewidth because of the increased Q-factor of the cavity. The grating is mounted on a piezo-electric transducer

(PZT) that can change the cavity length by applying a control voltage and thus allows to tune the laser. The grating is also mounted on a rotating mount which can be tilted with another piezo stack. By varying the tilt angle, the wavelength is selected according to the dispersive law of the grating:

$$2d \sin\theta = m\lambda, \tag{4.8}$$

where d is the pitch of the grating in nm, θ is the incidence angle of the laser beam and the grating and m is the diffractive order. The zeroth order beam is routed towards the output via a mirror mounted on the same rotatable arm so output beam alignment is decoupled from the rotation of the arm. Changing the length of the laser cavity allows fine tuning while rotating the grating gives the coarse tuning of the wavelength. The ECDL allows to reduce the linewidth of the laser from tens of MHz to few hundreds of kHz, and the linewidth was measured by beating two lasers. The beat note between two lasers tuned to close frequencies (e.g. cooling and repumping transitions) is equal to frequency difference of the two lasers and can be registered by the photodiode. By measuring the width of

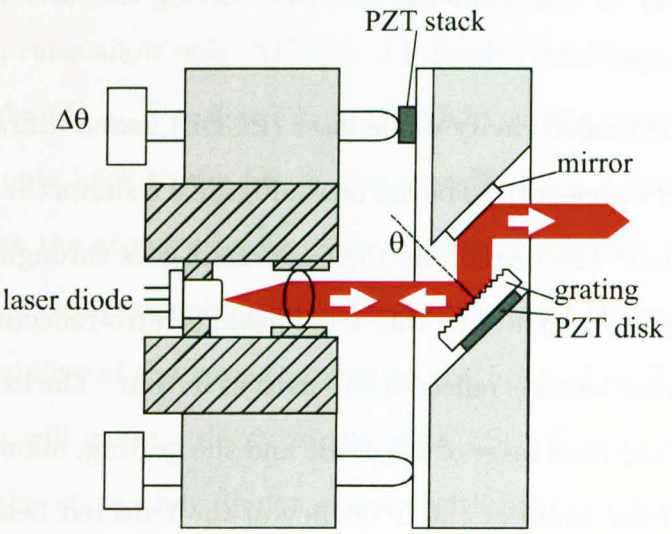

Figure 4.6: Schematic diagram of the extended-cavity laser, after Hawthorn *et al.* (2001), viewed from above.

beat signal, σ_{beat}, with the spectrum analyser the frequency of linewidth of the lasers can recovered as $\sigma_{laser} = \sigma_{beat}/\sqrt{2}$.

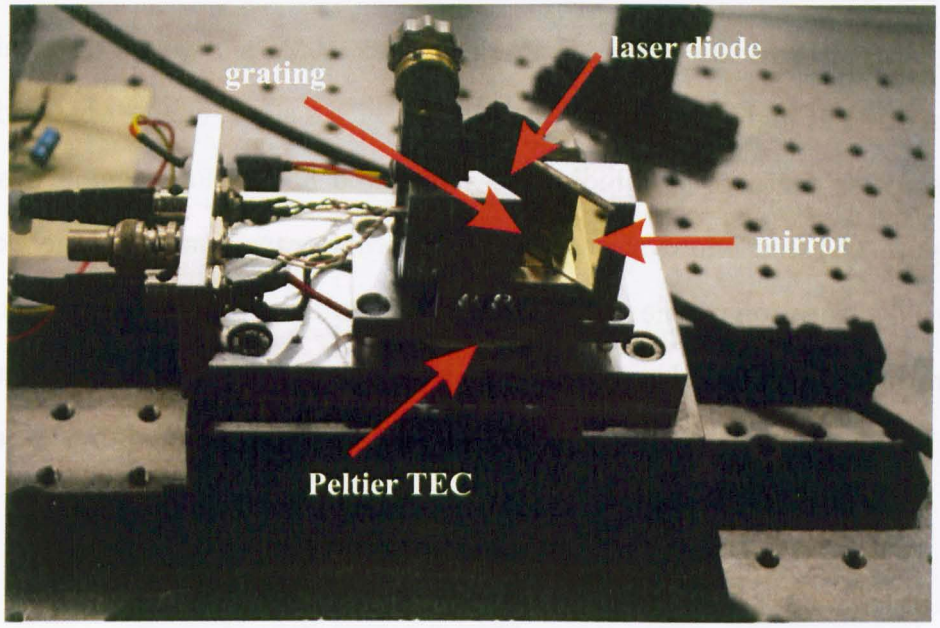

Figure 4.7: Photograph of the ECDL. In the picture the mirror and the diode laser in the collimation tube is visible. The grating is mounted on the aluminium arm seen in the first plan. The ECDL is mounted on a TEC that is placed on the aluminium bar fixed to the optical table.

To ensure the wavelength stability, the temperature of the extended cavity and the diode laser has to be kept constant and stable. This is essential, as any changes in the temperature within the extended cavity may cause the cavity to expand or contract, and the change in the length of the cavity modifies its resonant wavelength. The stabilisation is performed by mounting the laser diode and the extended cavity elements on a Peltier thermoelectric cooler (TEC). The temperature of the ECDL is monitored with a 100kΩ thermistor and controlled by a Thorlabs' TED-200C temperature controller. The extra heat produced by the TEC is dissipated by an aluminum bar that is fixed to the optical table (see figure 4.7).

4.2.3 Laser frequency stabilisation on an atomic transition

To lock the laser to the required frequency any drifts have to be controlled and corrected. One needs an error signal that is fed back to the laser, added to the driving current or to the voltage that controls the PZT, and which discriminates between drifts at higher and lower frequencies. Such a signal can be obtained from the absorption features of rubidium. A saturated absorption scheme was used (see Figure 4.8) that allows to resolve the hyperfine transitions from the Doppler broadened absorption profile – the Doppler broadening of rubidium atoms at room temperature is of the order of 0.5 GHz, while the splitting hyperfine structure peaks is of the order of hundred MHz (see figure 4.5). To obtain saturated

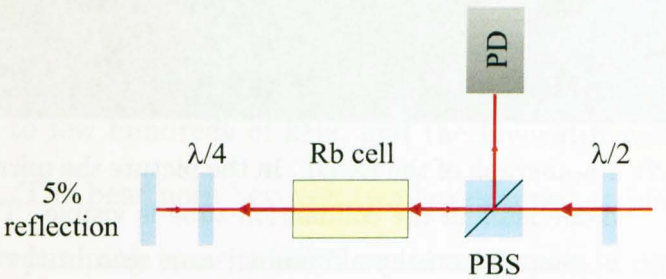

Figure 4.8: Saturation absorption scheme. Laser light coming from a laser is transmitted through cell containing rubidium vapour and then reflected back to obtain a Doppler-free signal on the photodiode PD.

absorption spectrum a strong pump beam is sent through the vapour cell. This beam is resonant only with the atoms whose Doppler shift is equal and opposite to the laser detuning, and it modifies the ground state population in the cell as atoms are transferred to excited state. If the counter-propagating weak probe beam is added its absorption will be affected. The probe beam generally interacts with a different velocity group of atoms, unless the beam is exactly tuned to an atomic transition, when both beams interact with the zero velocity group of atoms. In this case, the probe beam 'sees' fewer atoms as the population distribution of the ground state was modified by the pump beam. If the pump beam has an intensity

comparable with the rubidium saturation intensity, the observed transmission of the probe beam results in the features of hyperfine transitions appearing on the Doppler broadened absorption profile as reduced absorption. Figure 4.9 shows

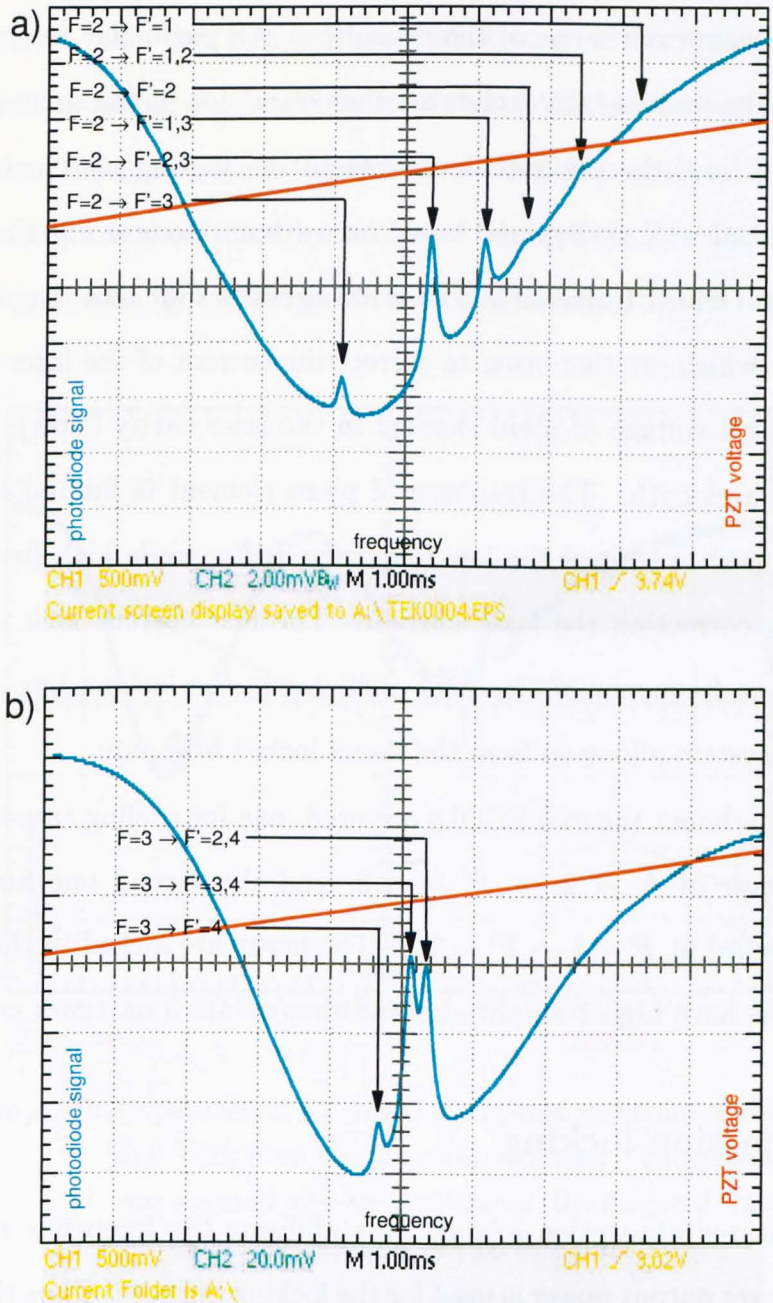

Figure 4.9: Experimental saturated absorption spectrum of the ^{87}Rb (a) and ^{85}Rb (b) trapping transitions in room temperature vacuum cell. The diagonal trace is the piezo-electric transducer (PZT) voltage. The $F \rightarrow F'$ transitions and cross-over peaks are indicated.

the saturated absorption profiles obtained for the Rb D_2 line. The trace in figure a) shows the scan over the $5s_{1/2} \rightarrow 5P_{3/2}$ transition for ^{87}Rb and scan b) for ^{85}Rb. In both cases the $F \rightarrow F'$ transitions are visible, as well as cross-over peaks, that occur at the frequency midway between two $F \rightarrow F'$ and $F \rightarrow F''$ transitions as the pump beam excites one of the transitions of a particular velocity group of atoms, while the probe beam excites another transition of the same group.

The signal form the photodiode is sent to the locking electronics made by the OU Electronics Workshop and based on a system designed at the Clarendon Laboratory at Oxford University. The error signal is split into two components: fast and slow which are then used to correct the current of the laser diode (fast) or to the control voltage of piezo element in the laser cavity (slow), and in turn control the wavelength. The response of piezo element is limited to few hertz so it can be used to control the low frequency drifts, while high frequencies are controlled by correcting the laser current. The fast current lock is limited to few kHz by the frequency of the local oscillator in the locking box circuit. The stabilisation system allows to keep the lasers locked for hours.

In the experiment the two ECDLs are used, one for cycling transition, locked to the crossover of $F = 2 \rightarrow F' = 2, 3$; and the second one for repumping transition, locked at $F = 1 \rightarrow F' = 1, 2$. The lasers are locked to the crossovers, as those peaks have higher amplitudes and thus create a narrower error signals.

4.2.4 Injection locking

Using a saturated absorption scheme for stabilising the frequency requires that some of the laser output power is used for the locking purpose. Thus the the power that can be delivered from ECDL to the experiment is of the order of 20 mW only. To get more power and still have narrow linewidth laser, the frequency stabilised laser is used to injection lock a second one (so-called master/slave configuration). The frequency of a second diode laser, slave, can be stabilised

by injecting a small amount of light from another source, master, into the laser cavity. The light injected from the master laser forces the slave to oscillate at the same frequency and to have the same spectral characteristic. Using this technique a well stabilised and narrow linewidth laser light can be generated without any loss of the power. Another Sanyo DL-7140-201 laser diode was used as a slave laser and it was mounted on the Peltier module to stabilise the temperature. The output power of the slave laser is therefore over 40 mW even if run at low current, and its wavelength is monitored by saturated absorption (see figure 4.10). The performance and stability of the injection lock also allows to run the laser locked for hours.

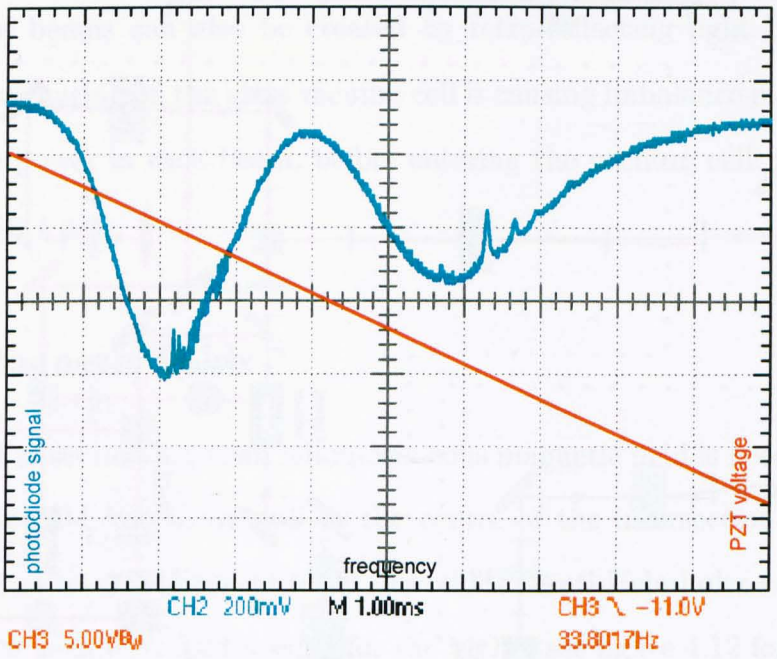

Figure 4.10: Experimental saturated absorption spectrum of the ^{85}Rb and ^{87}Rb from the injection lock laser. The master laser was scanned over the resonances (the diagonal trace) and the slave laser reproduces this this trace.

4.2.5 The optical arrangement of a MOT

The rubidium source is contained in a 10×6×6 cm glass cell with 6 mm thick walls, kept at the ultra-high vacuum pressure of few 10^{-9} Torr by an ion pump.

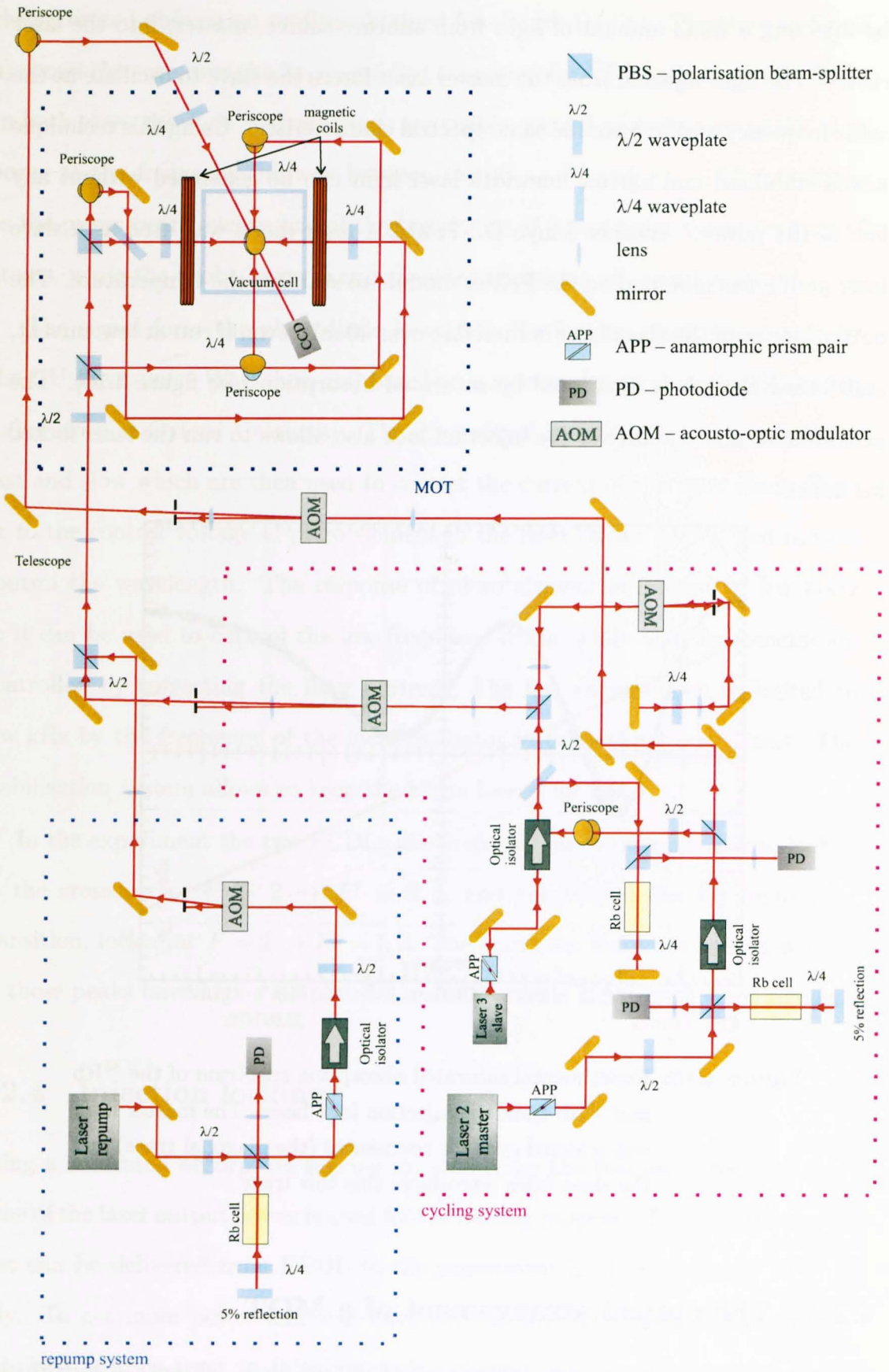

Figure 4.11: Arrangement of the optics on the optical table for laser cooling and trapping.

The scheme of the optics and the setup used for laser cooling and trapping is presented in figure 4.11. As explained in section 4.2.1, the laser used for cooling needs to be red detuned from the chosen atomic transition: for this purpose acousto-optic modulators (AOMs) are used to shift the beams with respect to the lock frequency. The cooling light is delivered from the slave laser and the re-pumping light comes from one of the ECDLs. The two beams are then mixed on a polarisation beamsplitting (PBS) cube and expanded to create beams of diameter 1 cm for the MOT.

The beam is then divided into 6 beams on beam-splitters to provide 3 pairs of counter-propagating beams for the MOT with polarisations set to σ^+/σ^-. The pairs of beams can also be created by retro-reflecting light but a lack of antireflection coating on the glass vacuum cell is causing imbalance in the reflected beams. The power in each beam, before entering the vacuum cell, is 1 mW and beam waist is 1 cm.

4.2.6 Magnetic fields

As discussed in section 4.1.4, an inhomogeneous magnetic field is needed to create a MOT. The field has to be null at the centre of the intersection of the laser beams and has to grow linearly in all directions. Anti-Helmholtz coils are used to prepare the magnetic field needed for the MOT (see figure 4.12 for the scheme

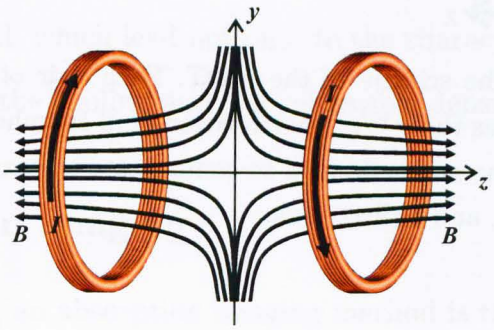

Figure 4.12: Magnetic field produced by a pair of coils with currents in opposite directions: anti-Helmholtz configuration.

of magnetic field). They are made of 70 turns each, have a diameter of 7 cm and are separated by 8 cm. The inductance of the coils is about 0.5 mH and the resistance is 1 Ω. For a typical current of 4 A they produce a 9.7 G/cm magnetic field gradient in the axial direction. The coils are arranged in such a way that the axial direction (z-axis) is parallel to the optical table and the image in figure 4.13 shows alignment of the MOT. The three pairs of Helmholtz coils (blue, green and red) are also used to compensate for spurious and earth magnetic fields, to ensure that the magnetic field is zero at the centre of the trapping region. In general those coils are used to set a uniform magnetic field when the experiment requires it.

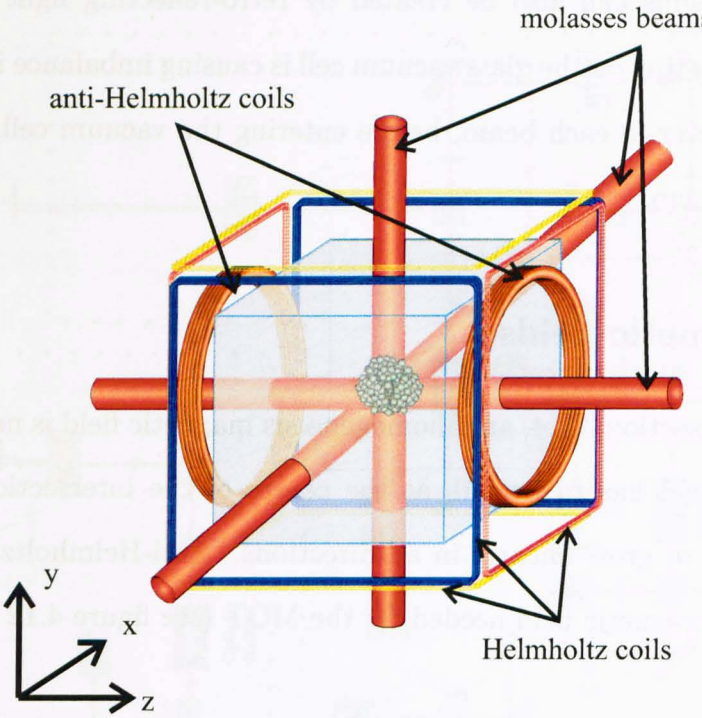

Figure 4.13: The scheme of the MOT. Each pair of molasses beams has the σ^+/σ^- polarisation, and Helmholtz coils produce the magnetic field to compensate the external fields in x, y, and z directions.

After the first MOT was achieved, work was carried out to optimise and characterise the efficiency of laser cooling and trapping. A typical experimental

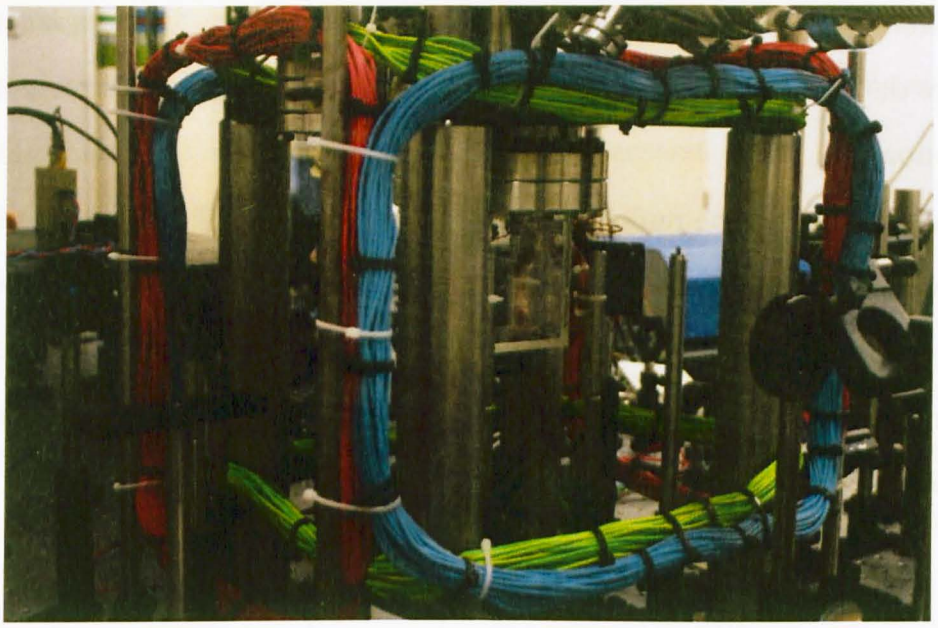

Figure 4.14: Photograph of the vacuum cell.

sequence includes a 2 seconds of trapping atoms in a MOT with 1.5Γ red-detuning of the laser beams, followed by a 10 ms molasses stage (9Γ detuning).

4.3 Characterisation of the MOT

The important parameters to characterise the atoms captured in the MOT are the number of atoms, size of the cloud, number density and temperature of the atoms. These parameters can be monitored by performing measurements based on observing the fluorescence of the atoms or by recording the absorption of resonant light through the cloud. In the following section the absorption measurements are described, which lead not only to the characterisation of the cloud but also to optimising the cooling and the achievable density of the cloud.

4.3.1 Absorption imaging

The advantage of using an absorption imaging method is that the imaging times can be much shorter then for fluorescence imagining, in the range of few microseconds compared to milliseconds for fluorescence imaging. Thus the movement of

atoms during the imaging process is negligible. Absorption imaging is used to measure the number of atoms, size of the cloud and the density and temperature of the atoms.

A beam tuned to the resonance $5S_{1/2},\ F = 2 \rightarrow 5P_{3/2},\ F' = 3$ is sent through the cloud of atoms that absorbs part of the light and reradiates it spontaneously so the shadow cast of atoms can be imaged on the CCD camera. When the resonant beam of the intensity I_0, with $I_0 \ll I_{sat}$, is propagating through an absorbing medium the intensity after absorption is given by Beer's law:

$$I(\xi,\zeta) = I_0(\xi,\zeta)e^{-\sigma \int_{\eta min}^{\eta max} n(\xi,\zeta,\eta)} \tag{4.9}$$

Here it is assumed that the beam travels in the direction of the η-axis of an η, ξ, ζ cartesian coordinate system, and the absorbing medium has thickness $\eta_{max} - \eta_{min}$. $I(\xi,\zeta)$ is the intensity of light after the absorption, σ is the absorption cross-section and $n(\xi,\zeta,\eta)$ is the number density of the atomic cloud. The shadow cast by the atomic cloud is imaged onto the CCD camera, so each image shows the intensity profile in the (ξ,ζ) plane. In the experiment $I(\xi,\zeta)$ and $I_0(\xi,\zeta)$ are obtained while recording two images: one with atoms (signal, I) and the other without (background, I_0). Typical images are presented in figure 4.15.

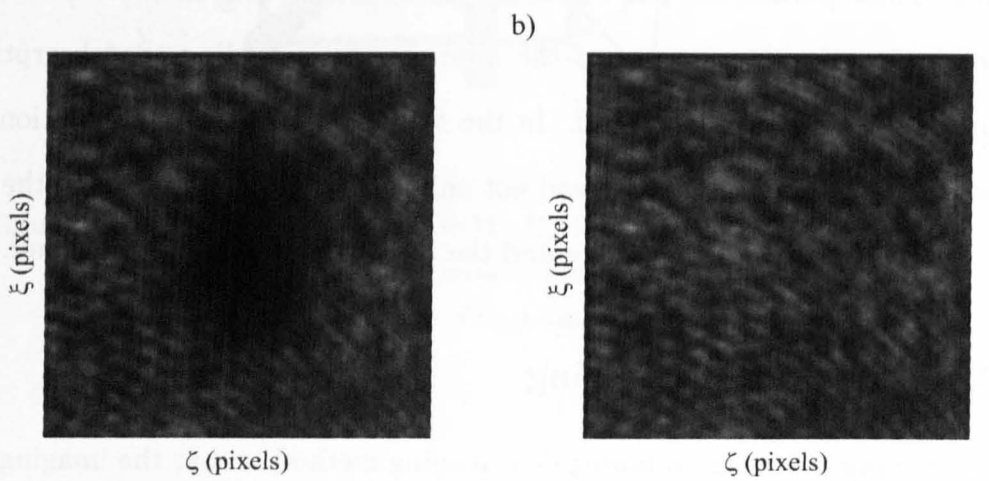

Figure 4.15: Absorption imaging pictures: a) with atoms, b) without atoms.

Quantitative information about the cloud of atoms can be obtained by processing the images $I(\xi, \zeta)$ and $I_0(\xi, \zeta)$. These intensity profiles can be modelled assuming that the spatial atomic distribution is Gaussian

$$n(\eta, \xi, \zeta) = \frac{N}{(2\pi)^{3/2} \sigma_\eta \sigma_\xi \sigma_\zeta} \exp\left(-\frac{\eta^2}{2\sigma_\eta^2} - \frac{\xi^2}{2\sigma_\xi^2} - \frac{\zeta^2}{2\sigma_\zeta^2}\right) \tag{4.10}$$

where N is total number of atoms in the cloud and σ_i are widths of the cloud, and defining the optical density, OD, as $OD = \ln\left(\frac{I_0(\xi,\zeta)}{I(\xi,\zeta)}\right)$. It follows that the profile of the 2-D shadow cast by the atoms is given by a 2-D Gaussian profile:

$$f(\xi, \zeta) = max_{OD} \exp\left(-\frac{(\xi - \xi_0)^2}{2\sigma_\xi^2} - \frac{(\zeta - \zeta_0)^2}{2\sigma_\zeta^2}\right) \tag{4.11}$$

where ξ_0, ζ_0 are centres of the cloud, σ_i are the Gaussian widths of the cloud and max_{OD} is the maximum value of the OD derived from the image. As $f(\xi, \zeta)$ is a 'two-dimensional' atomic density distribution max_{OD} has the dimension of m^{-2}.

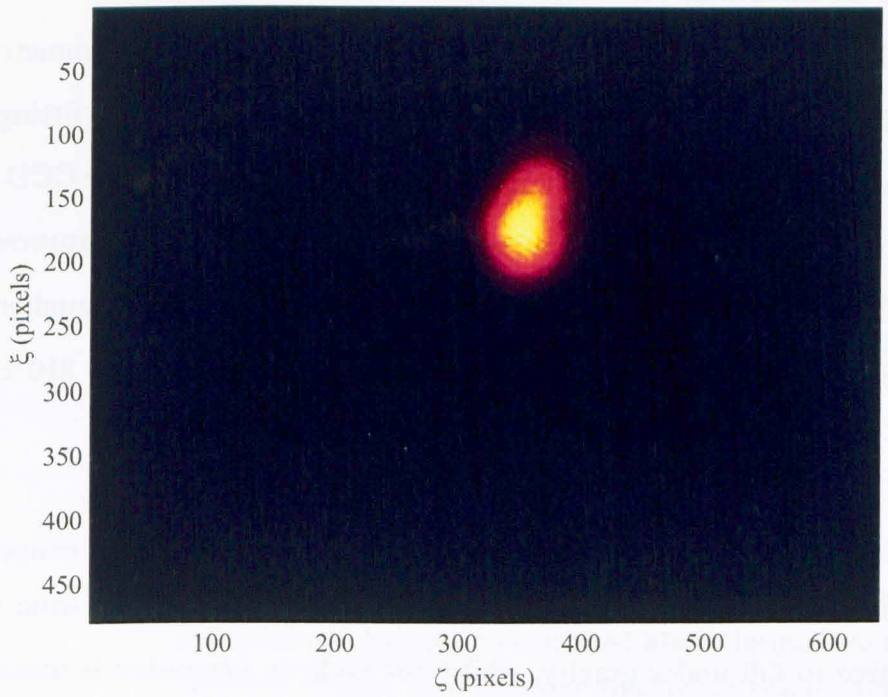

Figure 4.16: Image of the cold atoms cloud in false colours after the processing procedure. Dimensions are in pixels.

To process the images a 2-D optical density map is obtained from the signal and background images. For the images shown in figure 4.15 the OD map (in false colours) is presented in figure 4.16. Using equation 4.11 the following parameters can be obtained: widths in ξ and ζ directions (σ_ξ, σ_ζ), position of the centre of the cloud (ξ_0, ζ_0) and the maximum value of optical density (max_{OD}). From this parameters one can extract the values of atomic density and spatial distribution of the atoms in the trap after performing the calibration of the magnification of the imaging system.

4.3.2 Measurement of the number of atoms and the cloud size

By fitting the Gaussian profile in eqn. 4.11, the total number of atoms in the cloud can be calculated, $N = 2\pi\, max_{OD}\, \sigma_\xi\, \sigma_\zeta$. Knowing this number and the size of the cloud the number density can be calculated from the formula $n_0 = N/(2\pi)^{3/2}\sigma_\xi^2\sigma_\zeta$. Here it is assumed that the widths of the cloud in the ξ and η directions are the same. This assumption is justified as the cloud has cylindrical symmetry about the ζ axis due to the shape of the magnetic field of the MOT. The fitting is done using a Matlab script written to analyse the images captured by the CCD camera. In the experiment the typical values of total number of atoms captured in the MOT followed by 10 ms molasses stage is $3.0 \pm 0.3 \times 10^6$ with number density $6.4 \pm 0.6 \times 10^9$ cm^{-3}. The typical size of the atomic cloud is $\sigma_\xi = 310 \pm 10\mu$m.

4.3.3 Temperature of atoms

To measure the tempearture of the atoms, the cloud is released from the trap and let free to fall under gravity, whilst the ballistic expansion is monitored at different times to measure the velocity of atoms. The velocity of the expanding atoms has a Maxwell-Boltzman distribution, so the evolution of the width of the

Gaussian cloud in one dimension, released at time $t = 0$, is given by:

$$\sigma_i^2(t) = \sigma_{i0}^2 + \frac{k_B T_i}{m} t^2 \tag{4.12}$$

where $i = \xi, \zeta, \eta$; k_B is the Boltzman constant and m is the atomic mass of rubidium. From this equation the temperature of the cloud, T_i, can be extracted. The dependence of the size of the cloud squared, σ_i^2, on time squared, t^2, is linear as figure 4.17 shows, where the size of cloud in two dimensions was measured at different times after realising the atoms from the trap. In the optimal experimental sequence, where the atoms are trapped in a MOT and then further cooled in a molasses for 10 ms, the temperature of the atoms is 7.5±0.6 μK. This temperature is well below the Doppler limit for laser cooling and gives the speed of the atoms of 0.1 cm/s.

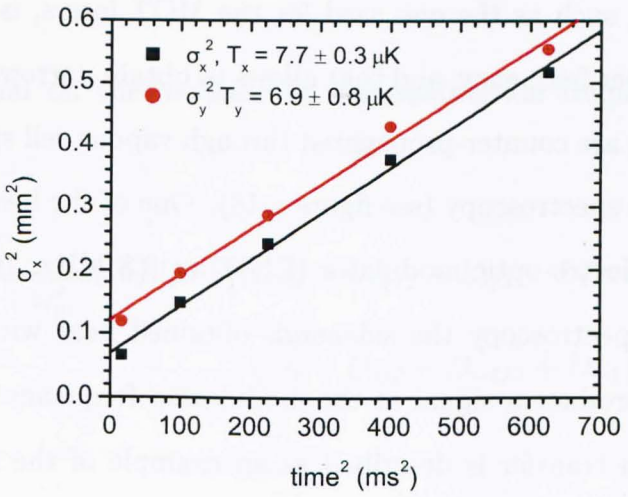

Figure 4.17: Measurement of the temperature of the cloud in two directions. The graph shows the dependence of the squared size of the cloud on the time squared where the gradient of the fitted straight lines is proportional to the temperature of the atoms.

4.4 Rydberg excitation laser system

This section will describe the laser system used in EIT experiments. As shown in section 2.2, figure 2.4, two laser sources are required for this experiment: one laser corresponds to the probe, at 780 nm, and the other to coupling, at 480 nm, the beam in the EIT ladder system. The same laser system (780 nm + 480 nm) will be also used in future for the coherent excitation to Rydberg states.

A detailed description of the 480 nm source will be given (the *blue* laser), as well as the technique used to phase lock the two lasers, which relies on a scheme based on EIT first demonstrated by Abel *et al.* (2009).

4.4.1 *Red* laser system

The laser used as 780 nm source, the *red* laser, is a grating-stabilised diode laser locked using the frequency modulation transfer lock (FMTL) as first was proposed by Cornish's group (McCarron *et al.*, 2008).

The advantage of FMTL scheme over the lock based on the saturated absorption spectroscopy, such as the one used for the MOT lasers, is that the laser is modulated at higher frequency, and that allows to obtain narrower laser width. In FMTL two beams are counter-propagated through vapour cell similarly as in saturated absorption spectroscopy (see figure 4.18). One of the beams, the pump, is modulated with electro-optic modulator (EOM) at 9.8 MHz. In frequency modulation transfer spectroscopy the sidebands obtained beat with probe beam in the Rb cell and produce a signal at the modulation frequency. The mechanism of the modulation transfer is described as an example of the four-wave mixing (McCarron *et al.*, 2008) where the two frequency components of the pump beam combine with the counter propagating probe beam via $\chi^{(3)}$ (the third order susceptibility). This generates a fourth wave as a sideband in the probe beam. On the fast A.C. photodiode the beating of the probe sidebands with the probe is detected.

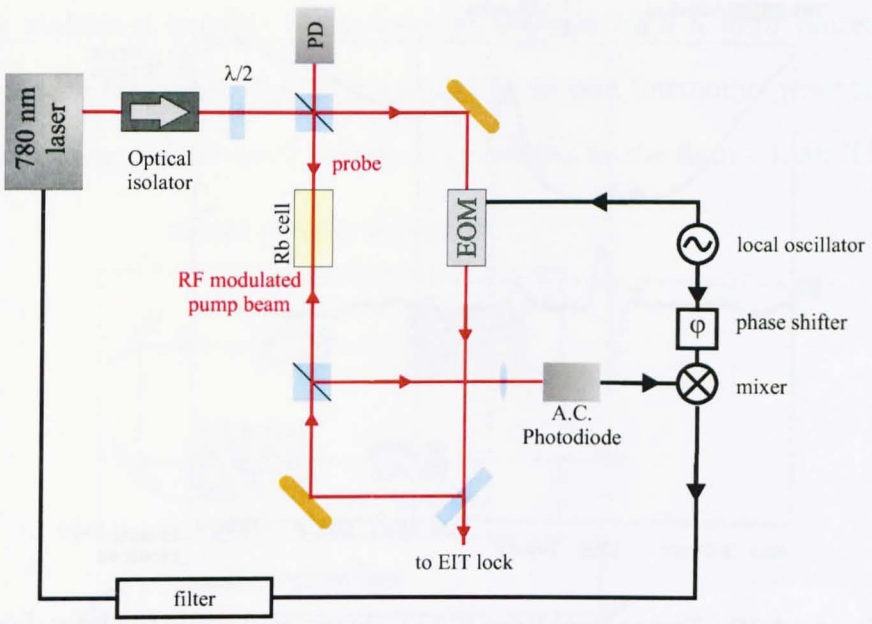

Figure 4.18: Schematic diagram of the modulation transfer spectroscopy lock setup. PD – photodiode, EOM – electro-optic modulator, cubes represent polarising beamsplitters. Signal from fast A.C. photodiode mixed with the local oscillator reference signal and sent to the low-pass filter to recover the error signal. The additional photodiode (PD) is used to monitor the saturated absorption signal.

The beat signal on the detector at the modulation frequency ω_m has the following form:

$$s(\omega_m) = \frac{C}{\sqrt{\Gamma^2 + \omega_m^2}} J_0(\delta) J_1(\delta) \left[(L_{-1} - L_{-1/2} + L_{1/2} - L_1) \cos(\omega_m t + \varphi) + \right.$$
$$\left. + (D_1 - D_{1/2} - D_{-1/2} + D_{-1}) \sin(\omega_m t + \varphi) \right] \tag{4.13}$$

where $J_n(\delta)$ is the Bessel function of order n, $L_n = \Gamma^2/(\Gamma^2 + (\Delta - n\omega_m)^2)$, $D_n = \Gamma(\Delta - n\omega_m)/(\Gamma^2 + (\Delta - n\omega_m)^2)$, and Γ is the natural linewidth, Δ is the frequency detuning from line center and φ is the detector phase with respect to the modulation field applied to the pump laser. The constant C represents all the other properties of the medium and the probe beam (McCarron *et al.*, 2008).

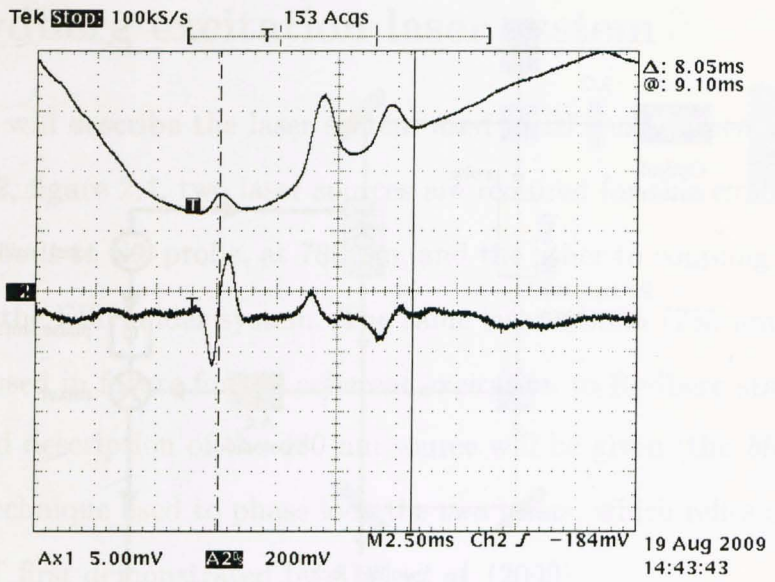

Figure 4.19: Error signal from FMTL (lower line) while the laser diode current was ramped around $5S_{1/2}$, $F = 2 \rightarrow 5P_{3/2}$, $F = 3$ transition. Upper line shows the saturated absorption spectrum where crossovers to $F = 2,3$ and $F = 1,3$ are also visible.

The signal from the photodiode is then mixed with the oscillator and then sent through 100 kHz low pass filter. This is a phase-sensitive detection scheme and it recovers the absorption signal of the resonance. The sine terms in the eqn. 4.13 present the quadrate component of the signal and cosine term the in-phase component (McCarron *et al.*, 2008). Thus by changing the phase of the reference signal it is possible to recover the absorption and dispersion components of the resonance. The laser is locked on the $5S_{1/2}$, $F = 2 \rightarrow 5P_{3,2}$, $F = 3$ transition by feeding the error signal (dispersion component) to the laser. Figure 4.19 shows the error signal for FMTL.

4.4.2 *Blue* laser system

The *blue* laser system is a frequency doubled high power commercial laser system TA/DL-SHG 110 manufactured by Toptica with the output power of 250 mW and tunability over the range from 479 nm to 487 nm. The Toptica system comprises

a grating stabilised tunable diode laser at 960 nm with a high power tapered amplifier and a frequency doubling system for second harmonic generation. The schematic drawing of the laser system is presented in the figure 4.20. The mode-

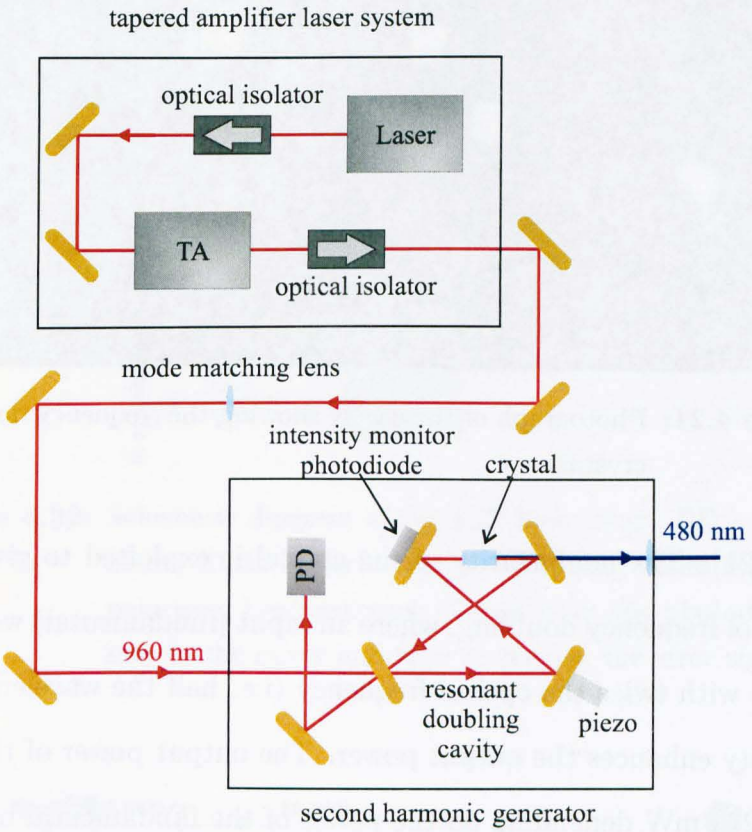

Figure 4.20: Scheme of the Toptica second harmonic generator laser system. It consists of two parts: the tapered amplifier (TA) system generating the fundamental beam at 960 nm and the second harmonic generator with nonlinear crystal.

hop free range of the diode laser is 16 GHz and the tuning can be done by adjusting both the current and piezo position using the electronic controllers provided with the laser. For long range tuning, which is necessary for changing laser frequency to different Rydberg transitions, the piezo element controlling the grating can be moved manually. The output beam from the laser is fed into the tapered amplifier, which gives an output power of up to 1W power.

The amplified fundamental beam is sent to the second-harmonic generation stage (SHG), which consists of a resonant doubling cavity and a nonlinear crystal

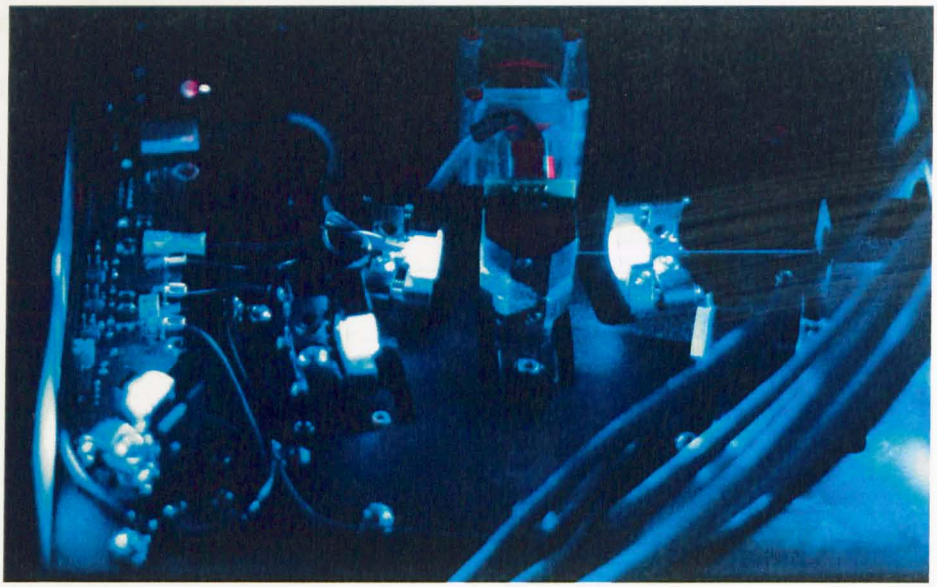

Figure 4.21: Photograph of the cavity showing the frequency doubling crystal.

(see figure 4.21). The nonlinearity of the crystal is exploited to give rise to the phenomenon of frequency doubling, where an input (fundamental) wave generates another wave with twice the optical frequency (i.e. half the wavelength) and the resonant cavity enhances the output power. The output power of the SHG laser reaches 250–270 mW depending on the power of the fundamental beam.

To address specific Rydberg states the laser has to be both very stable and narrow, as the linewidth of the Rydberg transitions is of the order of few kHz. The frequency stabilisation system is implemented on the basis of the scheme described in Abel *et al.* (2009); the lock signal for the 480 nm laser is derived from the EIT feature (see section 2.2.2) observed in a room-temperature rubidium vapour cell.

The probe beam, 780 nm, and coupling beam, 480 nm, are counter-propagated through a magnetically shielded rubidium cell to obtain an EIT signal. The probe beam is modulated at 9.8 MHz by the EOM to give the sidebands above and below the EIT feature. Those sidebands beat with the probe beam which produce a signal at the modulated frequency at the detector. This signal is detected using a fast photodiode and then mixed with an oscillator to produce the error signal

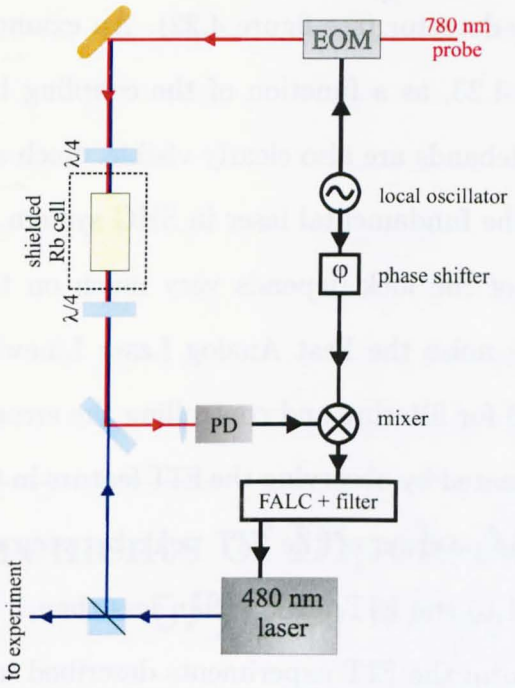

Figure 4.22: Schematic diagram of the EIT lock setup. PD – photodiode, EOM – electro-optic modulator, cubes represent polarising beamsplitters. Signal from the photodiode is sent to the mixer and filter to recover the error signal.

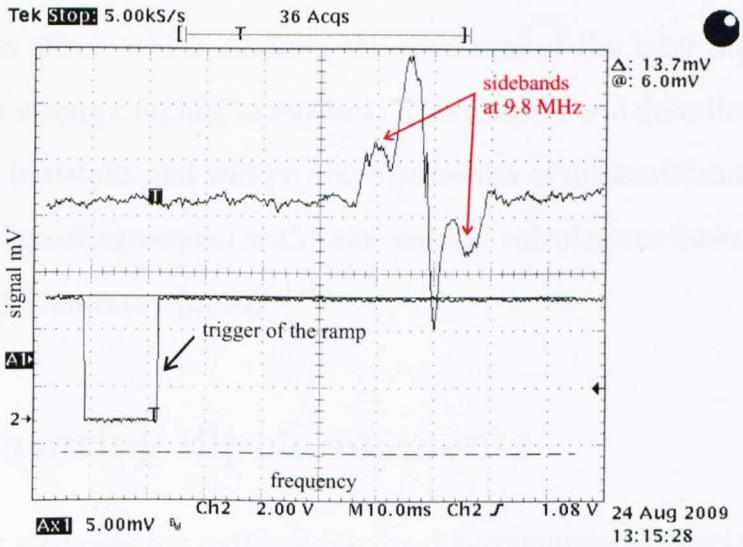

Figure 4.23: EIT error signal with clearly visible sidebands. Probe (780 nm) laser was locked and the coupling (480 nm) laser was scan over the EIT line for the $24D_{5/2}$ Rydberg state. Power in the blue laser was 4.6 mW. Lower trace shows trigger signal for the ramp of the blue laser frequency.

from a phase sensitive detector (see figure 4.22). An example of the error signal is presented in figure 4.23, as a function of the coupling beam frequency. The features due to the sidebands are also clearly visible. Such an error signal is then fed to the current of the fundamental laser in SHG system.

The performance of the lock depends very much on the noise of the error signal. To reduce the noise the Fast Analog Laser Linewidth Control (FALC) from Toptica was used for filtering and controlling the error signal. The stability of the lock can be estimated by observing the EIT feature in the cold atoms sample for the variation of the position of the EIT peak between scans (see chapter 5). The laser stays locked to the EIT peak within less then 1 MHz for a few hours, which enables to perform the EIT experiments described in the next chapter.

CHAPTER 5

Measurements of Dipole Moments for $5P_{3/2}$ to $nD_{5/2}$ Transitions

This chapter presents the measurements of the dipole moments for transitions between the first excited state of rubidium, $5P_{3/2}$, and Rydberg $nD_{5/2}$ states, for several values of n. The dipole moments are measured by exploiting the Autler-Townes effect, which modifies the spectrum of the laser interaction with the system for strong coupling intensities. This chapter will describe the measurement method in details and will present the results of measurements, which were found to be in good agreement with semiclassical calculations based on model by Dyachkov and Pankratov (1994).

5.1 Measuring dipole moments

Dipole matrix elements are required for the determination of spectroscopic properties of excited atoms like oscillator strengths, polarisabilities and radiative lifetimes. Application of Rydberg states in quantum information and local blockade effect exploit the interaction between neighbouring Rydberg states that is governed by these radial matrix elements. In the coherent interactions in mesoscopic

ensembles of ultracold Rydberg atoms with laser excitation (Reetz-Lamour *et al.*, 2008; Gaëtan *et al.*, 2009) the dipole matrix elements between ground, first excited and Rydberg states determine the Rabi oscillations observed.

There is no exact analytical solution for the calculation of radial matrix elements for alkali atoms, as can be found for hydrogen (Bethe and Salpeter, 1977), however, many theoretical models have been developed. Despite this, there is a lack of experimental data on dipole matrix elements for rubidium, and in this chapter the measured dipole matrix elements for $5P_{3/2} \rightarrow nD_{5/2}$ with $20 \leq n \leq 48$ transitions are presented.

The scheme employed for the direct measurement of dipole moments exploits the dependence of the Rabi frequency on the dipole moment which can be derived from the measurements of the Autler-Townes splitting.

5.1.1 The method and experimental scheme

Recall that the Rabi frequency for an atomic transition from state $|a\rangle$ to $|b\rangle$ is defined as

$$\Omega = -\frac{E}{\hbar}\mu_{ab} \tag{5.1}$$

where E is the amplitude of the electric field of the laser light and μ_{ab} is the dipole matrix element for the transition $|a\rangle \rightarrow |b\rangle$. The relation between laser power and electric field amplitude for a Gaussian beam is $I = \frac{2P}{\pi w_0^2} = \frac{c\epsilon_0}{2}E^2$, where w_0 is the waist of the laser beam, c and ϵ_0 are speed of light and vacuum permittivity respectively. Equation (5.1) can then be rearranged as:

$$\Omega = -\mu_{ab}\frac{2}{\hbar\sqrt{\pi w_0^2 c\epsilon_0}}\sqrt{P} = a\mu_{ab}\sqrt{P}. \tag{5.2}$$

This shows the linear dependence of the Rabi frequency on the square root of laser power with linear coefficient directly related to the dipole moment.

The Rabi frequency can be measured by exploiting the Autler-Townes effect (see section 2.2.2) at the different values for the laser power, so that the linear trend of equation 5.2 can be reconstructed and the dipole moments measured. The employed two-photon excitation scheme is presented in figure 5.1. A weak probe laser (780 nm), with Rabi frequency Ω_p, is driving the transition between the ground state $|1\rangle = |5S_{1/2}\rangle$ and excited state $|2\rangle = |5P_{3/2}\rangle$, while a strong coupling laser (480 nm) is tuned to drive the $|2\rangle = |5P_{3/2}\rangle \rightarrow |3\rangle = |nD_{5/2}\rangle$ transition with Rabi frequency Ω_c. The weak probe and strong coupling beams guarantee that the population of states other than $|1\rangle$ can be neglected and the probe absorption can be described by eqn. 2.34. Two effects, described in chapter 2, arise in this scheme: EIT and AT, depending on the Rabi frequency of the coupling beam.

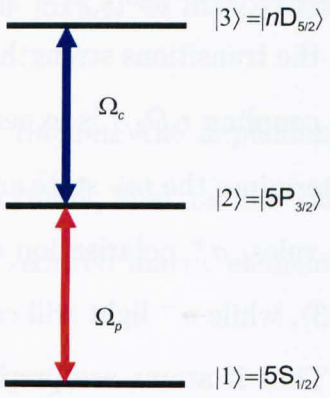

Figure 5.1: Schematic energy levels for 3-level system in ^{87}Rb. Ω_p is the Rabi frequency of probe beam (780nm) and Ω_c is the Rabi frequency of coupling beam (480nm).

To maximise the transition strength and to make the analysis of the experimental results as simple as possible, it is necessary to prepare the sample in an appropriate state so the single transition can be driven. The atoms are prepared in the $|5S_{1/2},\ F = 2,\ m_F = 2\rangle$ state and the probe light is σ^+ polarised so that it drives the transition $|5S_{1/2},\ F = 2,\ m_F = 2\rangle \rightarrow |5P_{3/2},\ F = 3,\ m_F = 3\rangle$, whilst the coupling beam, again σ^+ polarised, couples $|5P_{3/2},\ F = 3,\ m_F = 3\rangle$ to $|nD_{5/2},\ F = 4,\ m_F = 4\rangle$ (see figure 5.2).

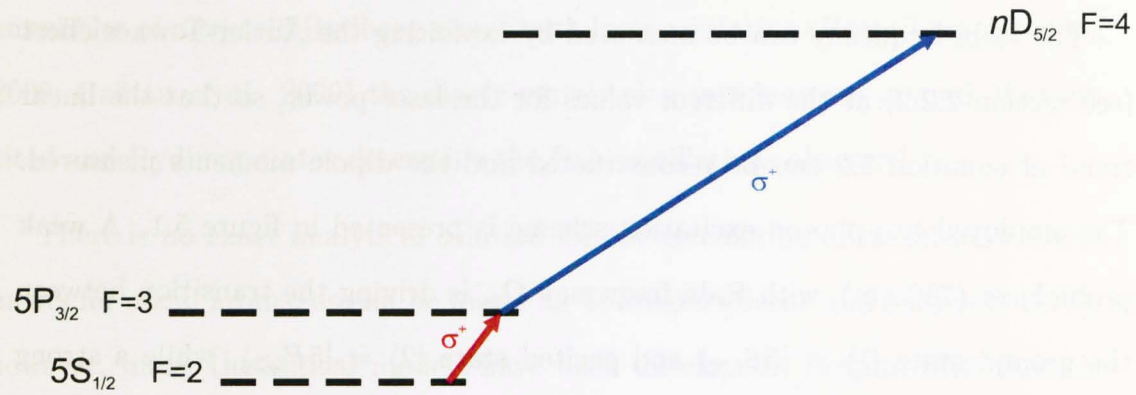

Figure 5.2: Schematic energy levels for ^{87}Rb excitation from $|5S_{1/2}, F = 2, m_F = 2\rangle$ using σ^+/σ^+ light.

It is noteworthy that it is possible to control the excitation path easily by varying the frequency and polarisation of the coupling beam and the diagram in figure 5.3 shows the possible combinations. By changing the frequency of the beam one is allowed to choose between $nD_{5/2}$ and $nD_{3/2}$ states (separation of the order of few GHz). However, the transitions strengths for $J = 3/2$ state are much weaker then for $J = 5/2$, so coupling $nD_{3/2}$ is experimentally more challenging. The choice of polarisation determines the m_F state addressed. As seen from figure 5.3, because of the selection rules, σ^+ polarisation will drive a single transition from $|5P_{3/2}, F = 3, m_F = +3\rangle$, while σ^- light will couple to several upper states with different values of F. Thus if atoms are prepared in the $F = 2, m_F = 2$ state by tuning the laser to transition to desired J state and choosing correct

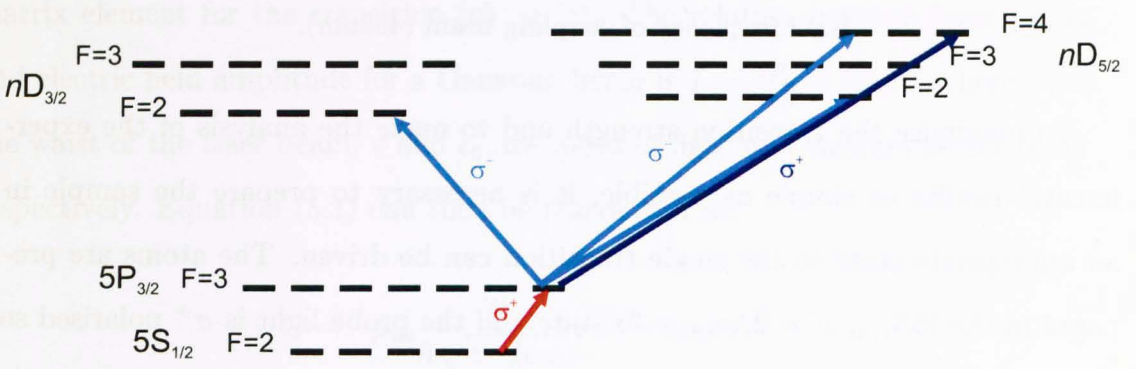

Figure 5.3: Schematic energy levels and possible transitions when σ^+ and σ^- polarisation of laser is used. Each line in F state represents one m_F state, $m_F = -F, \ldots, 0, \ldots, F$.

polarisations of the lasers the three-level system can be created, and EIT and AT can be observed.

5.1.2 Reduced matrix elements

In the experiment the laser is much narrower then the hyperfine splitting of the $5P_{3/2}$ state (hundreds MHz) and atoms are prepared in one m_F state as described above. Therefore, the dipole moment measured in the experiment has spherical components μ_q, $q = 0, \pm 1$, which have matrix elements:

$$\mu_q^{exp} = \langle 5P_{3/2}, F, m_F | er_q | nD_{5/2}, F', m'_F \rangle. \tag{5.3}$$

From this the dipole moment $\vec{\mu}^{all} = \langle 5P_{3/2} || e\vec{r} || nD_{5/2} \rangle$ (with $\vec{r}$ having the components r_q, $q = 0, \pm 1$) of the $|5P_{3/2}\rangle \rightarrow |nD_{5/2}\rangle$ transition can be calculated as presented below.

Applying Wigner-Eckart theorem the dependence on m_F can be extracted from 5.3 using the three-J symbol, that factors these matrix elements into an angular factor multiplying a reduced matric element

$$\langle 5P_{3/2}, F, m_F | er_q | nD_{5/2}, F', m'_F \rangle =$$

$$= (-1)^{F'+m_F-1} \sqrt{2F+1} \begin{pmatrix} F' & 1 & F \\ -m'_F & q & m_F \end{pmatrix} \langle 5P_{3/2}, F || e\vec{r} || nD_{5/2}, F' \rangle. \tag{5.4}$$

Here $\langle 5P_{3/2}, F || e\vec{r} || nD_{5/2}, F' \rangle$ is the reduced matrix element, and $\begin{pmatrix} F' & 1 & F \\ -m'_F & q & m_F \end{pmatrix}$ is a three-J symbol related to Clebsch-Gordan coefficients (Brink and Satchler, 1994).

From this reduced matrix element F can be decoupled into J and I by the use of six-J symbol. This can be done because the electric dipole Hamiltonian couples only to the J angular momentum. So using the six-J symbol the last

term of (5.4) takes a form (Brink and Satchler, 1994):

$$\langle 5P_{3/2}, F||e\vec{r}||nD_{5/2}, F'\rangle =$$
$$= (-1)^{F'+J+1+I}\sqrt{(2F'+1)(2J+1)}\begin{Bmatrix} J & J' & 1 \\ F' & F & I \end{Bmatrix}\langle 5P_{3/2}||e\vec{r}||nD_{5/2}\rangle. \tag{5.5}$$

Combining (5.4) and (5.5) one obtains:

$$\langle 5P_{3/2}, F, m_F|er_q|nD_{5/2}, F', m'_F\rangle = (-1)^{2F'+J+I+m_F}\sqrt{(2F+1)(2F'+1)(2J+1)}\times$$
$$\times\begin{Bmatrix} J & J' & 1 \\ F' & F & I \end{Bmatrix}\begin{pmatrix} F' & 1 & F \\ -m'_F & q & m_F \end{pmatrix}\langle 5P_{3/2}||e\vec{r}||nD_{5/2}\rangle. \tag{5.6}$$

Whilst the hyperfine structure of the Rydberg state cannot be resolved, the polarisation of the laser (σ^+) restricts the final state to one possibility, with $F' = 4$, $m'_F = 4$ (see figure 5.1). Substituting the values into (5.6) one obtains the angular coefficient; the values of parameters are: $J = 3/2$, $J' = 5/2$, $F = 3$, $F' = 4$, $I = 3/2$, $m_F = 3$, $m'_F = 4$ and $q = 1$, so the angular coefficient is $\sqrt{\frac{2}{3}}$, and equation 5.2 is being converted into:

$$\Omega = -\frac{1}{\hbar w_0}\sqrt{\frac{8P}{3\pi c\epsilon_0}}\langle 5P_{3/2}||e\vec{r}||nD_{5/2}\rangle. \tag{5.7}$$

5.2 The experiment

To perform the experiment two laser beams are needed, as was mentioned in previous sections: a weak probe beam at 780 nm and a strong coupling beam at 480nm. The scheme of the experimental arrangement is shown in figure 5.4. The probe beam is delivered from the diode laser used for the MOT, so it is stabilised to the crossover of the $5S_{1/2}$, $F = 2 \rightarrow 5P_{3/2}$, $F' = 2, 3$ transition. It is

then shifted using a double-pass and a single pass AOMs to the $5S_{1/2}$, $F = 2 \rightarrow 5P_{3/2}$, $F' = 3$ transition and σ^+ polarised. The double pass AOM enables the scan over the resonance within ± 25 MHz. The coupling beam is delivered directly from the Toptica system, tuned to the $|5P_{3/2}, F = 5\rangle \rightarrow |nD_{5/2}\rangle$ transition and again is σ^+ polarised. To switch on/off the coupling beam an AOM is used.

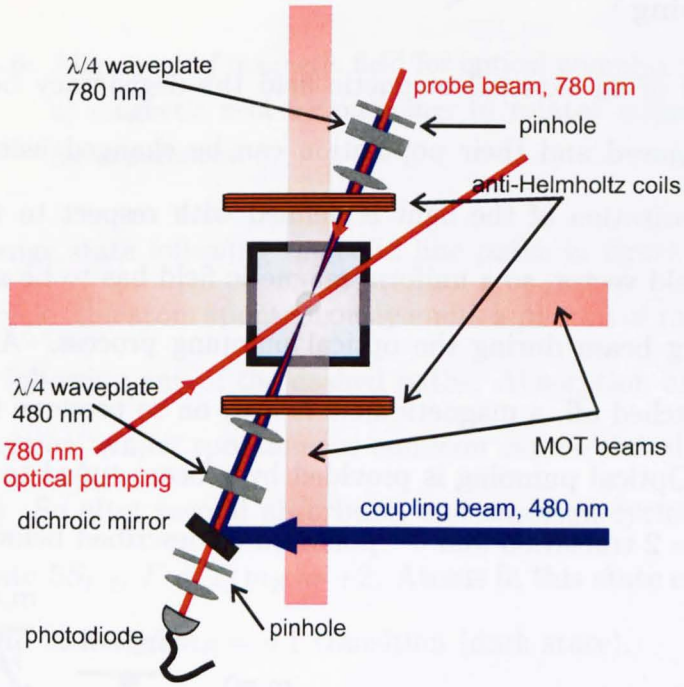

Figure 5.4: Schematic diagram of the setup for EIT experiments in the MOT.

The beams are counter-propagating through the vacuum chamber and aligned so they hit the centre of the cloud. The coupling beam is focused to a beam waist of 0.18 mm over the cloud (see section 5.2.5). The maximum power of the coupling beam varies from 70 to 85 mW for different wavelengths (n) and is determined by the power of the fundamental laser in the SHG laser (see section 4.4) and the power delivered to the atomic sample is controlled by the AOM. A dichroic mirror is used to combine the coupling beam with the probe beam, and used to route the probe beam for imaging on the photodiode.

5.2.1 Preparation of the sample

To prepare the atoms in the $|5S_{1/2}, F = 2, m_F = 2\rangle$ state approximately 3×10^6 atoms at a temperature of 6 μK are loaded in a MOT, with the population distributed amongst all m_F states as they are degenerated in absence of magnetic field. To transfer atoms to the desired m_F state optical pumping must be used.

Optical pumping

In the presence of an external magnetic field the degeneracy between Zeeman substates is removed and their population can be changed using σ^+ polarised light. The polarisation of the light is defined with respect to the direction of the magnetic field vector, so a uniform magnetic field has to be aligned with the optical pumping beam during the optical pumping process. After the optical pumping is switched off, a magnetic field is kept on to preserve the polarisation of the atoms. Optical pumping is provided by a beam tuned to the $5S_{1/2}$, $F = 2 \rightarrow 5P_{3/2}$, $F' = 2$ transition and σ^+ polarised as described below.

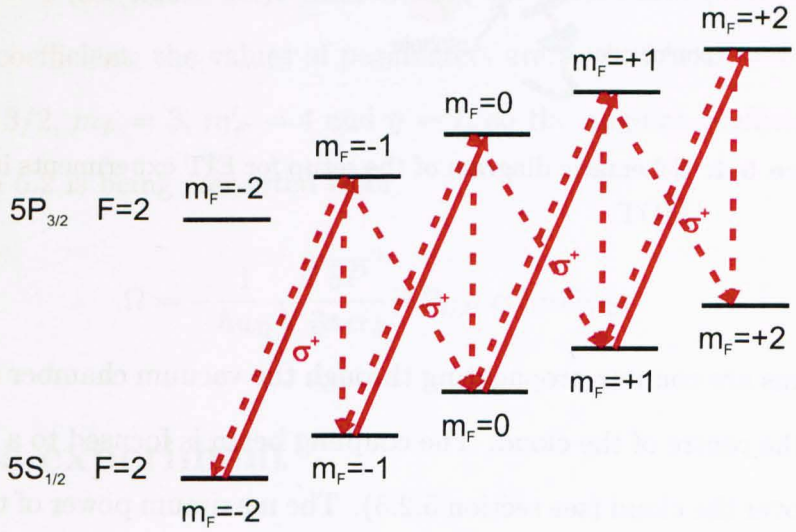

Figure 5.5: Atomic levels of $F = 2$ states of rubidium. Solid arrows represent allowed transitions for σ^+-polarised light, dashed arrows transitions to which atoms can spontaneously decay.

If two hyperfine levels $F = 2$ of $5S_{1/2}$ and $5P_{3/2}$ states of rubidium are considered and circularly polarised σ^+ light is applied then the atoms will absorb

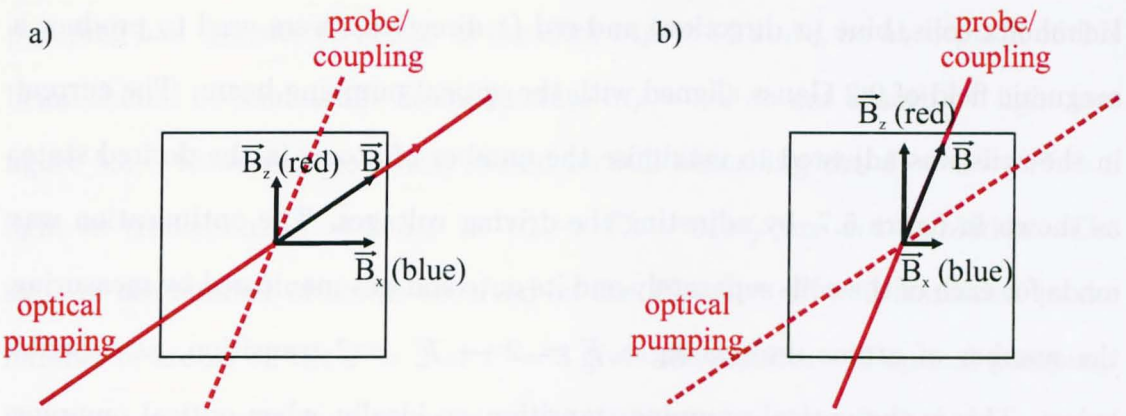

Figure 5.6: Alignment of magnetic field for optical pumping pumping: a) magnetic field for pumping; b) rotated magnetic field for experiment.

photons and change state following the solid line paths in figure 5.5. Following one absorption cycle, the atom spontaneously emits a photon of random polarisation and decays following any of the dashed paths. Absorption always promotes $\Delta m_F = +1$ transition, whilst spontaneous emission can be linked to $\Delta m_F = \pm 1$ or 0 (σ^+, σ^-, π). So after several absorbtion and emission cycles the atom will end up in the state $5S_{1/2}$, $F = 2$, $m_F = +2$. Atoms in this state cannot absorb a σ^+ photons due to lack of $\Delta m_F = +1$ transition (dark state).

Ideally, the optical pumping beam should overlap with the probe/coupling beams for EIT-AT experiment and during the experiment the magnetic field is on to keep atoms in the $m_F = +2$ state. However, due to experimental constrains, it was not possible to align the optical pumping beam with the probe/coupling beam, and the scheme shown in figure 5.4 was applied. Atoms were pumped to $m_F = +2$ state by the optical pumping beam and then the magnetic field was rotated (see fig 5.6) to align the polarisation of atoms with probe and coupling beams and keep them in the $m_F = +2$ state for the experiment. In order to set the magnetic field 3 pairs of coils were used in Helmholtz configuration. Using those three pairs of coils an arbitrary magnetic field can be created. The value and direction of the magnetic field was estimated based on the geometry of the alignment of the beams to be parallel to the probe/coupling beams. Two of the

Helmholtz coils, blue (x direction) and red (z direction), were used to produce a magnetic field of 0.2 Gauss aligned with the optical pumping beam. The current in the coils was adjusted to maximise the number of atoms in the desired state, as shown in figure 5.7, by adjusting the driving voltages. The optimisation was made for each of the coils separately and its outcome was monitored by measuring the number of atoms undergoing a $F = 2 \rightarrow F' = 2$ transition, as describe below. This is the optical pumping transition, so ideally, when optical pumping is maximised, no atoms should be observed as the $F = 2$, $m_F = +2$ state is dark to σ^+ light. Values of the driving voltages were found for which the number of observed atoms still interacting with σ^+ light was minimised.

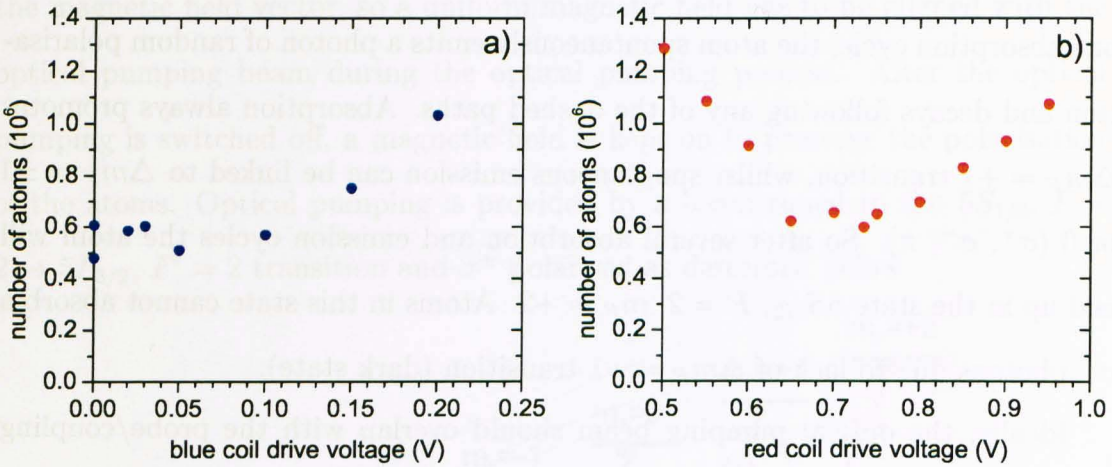

Figure 5.7: Finding optimal magnetic field for optical pumping: a) adjusting blue coil (x direction in the MOT), and b) red coil (z direction in the MOT). The graphs present the number of atoms detected on the $F = 2 \rightarrow F' = 2$ transition after performing the optical pumping pulse for different values of the driving voltage of magnetic coils. The minimum in the number of atoms indicates that the magnetic field is optimised.

To test and confirm the efficiency of the optical pumping, absorption imaging on two transitions $F = 2 \rightarrow F' = 2$, which is the optical pumping transition, and $F = 2 \rightarrow F' = 3$, which is the MOT cycling transition is performed. When the cloud is imaged with σ^+ polarised $F = 2 \rightarrow F' = 2$ light after the optical

pumping had transferred atoms to the dark $m_F = +2$ state, no absorption of this beam should be seen as the atoms in state $m_F = +2$ do not absorb σ^+ light (see figure 5.5). However, the atoms should be still absorbing the $F = 2 \rightarrow F' = 3$ light as transitions $F = 2, m_F = +2 \rightarrow F' = 3, m'_F$ are not forbidden. The ratio of the number of atoms observed on the $F = 2 \rightarrow F' = 2$ transition to the number of atoms on the $F = 2 \rightarrow F' = 3$ gives the efficiency of optical pumping. Furthermore atom losses were monitored by observation of the fluorescence signal.

As it was mentioned before, the optical pumping beam is not overlapping with the probe and coupling beams used for EIT. Thus, in order to have the atoms in the m_F state required for the EIT experiment, the magnetic field has to be rotated adiabatically (see figure 5.6). To maintain the polarisation of atoms the rotation has to be slow enough for the atoms to follow the change, as the change in the magnetic field vector causes coupling with other Zeeman states by introducing some transverse field. The population does not stay the same unless the variation in the transverse field over a Larmor period is much less then the amplitude of the magnetic field.

To test the efficiency of the rotation of the magnetic field and the preservation of the polarisation of the atoms after the rotation the following procedure was carried out: atoms were optically pumped, the field was rotated and it was left on for the time in which the experiment would have been carried out. Following this the original pumping field was restored to image the number of atoms on the pumping transition. Different times and ways of rotation were tested as shown in table 5.1. Firstly, the change between magnetic fields shown in figures 5.6a (the field for optical pumping) and 5.6b (for the experiment), was made by ramping the driving voltages of the magnetic coils between the values for those two fileds. The ramping time was set to 1 and 2 ms and the number of atoms optically pumped in this process was only about 60%. It was found that the best condition is to switch the field without ramping. This could be explained in terms

number of atoms on pumping transition	fluorescence signal	sequence			
		rotation of $\vec{B}$	experiment	rotation of $\vec{B}$	
1.22×10^6	3.05×10^8	1 ms ramp	1 ms	1 ms ramp	image
1.17×10^6	3.23×10^8	2 ms ramp	1 ms	2 ms ramp	image
1.55×10^6	3.02×10^8	1 ms ramp	0.005 ms	1 ms ramp	image
2.52×10^6	3.07×10^8	1 ms ramp	1 ms	none	image
0.63×10^6	3.13×10^8	change	2 ms	change	image
0.56×10^6	2.99×10^8	change	1 ms	change	image

Table 5.1: Optimisation of the rotation of the magnetic field. The number of atoms detected on the $F = 2 \rightarrow F' = 2$ transition after performing the optical pumping pulse and various sequences of rotation of the field.

of the eddy currents in the magnetic coils, that are induced by the fast change of the magnetic flux during the switch off of the coil current. These currents will produce a time and spatially varying magnetic field that dies out in time. The coils have the resistance $R = 1\ \Omega$ and inductance $L = 0.5$ mH, which gives a current decay time $L/R = 0.5$ ms, which makes the change of the magnetic field adiabatic. With this optimised sequence 80% of atoms could be prepared in the desired state $|5S_{1/2}, F = 2, m_F = 2\rangle$.

5.2.2 Obtaining spectra

Once the atoms were prepared in the $|1\rangle = |5S_{1/2}, F = 2, m_F = 2\rangle$ state, the coupling and probe beams were turned on. The probe beam addressed the $|1\rangle \rightarrow |2\rangle = |5P_{3/2}, F' = 3, m'_F = 3\rangle$ transition and the coupling beam was tuned to $|2\rangle \rightarrow |3\rangle = |nD_{5/2}, F'' = 4, m''_F = 4\rangle$. The probe beam was swept through the resonance covering 50 MHz range in 1 ms using an AOM. The signal of the probe beam transmitted through the sample was measured on the photodiode and the trace was recorded on a digital oscilloscope. The intensity of the probe beam was set to $0.012I_{sat}$ to assure a low probe beam intensity and the maximum power for

the coupling beam varied from 70 to 85 mW for different wavelengths (n) giving a maximum peak intensity of 70 to 85 W/cm^2.

The photodiode measured the power of the transmitted light, after it passed through the sample. Recalling section 4.3.1, when the intensity of the probe beam is much weaker then saturation intensity, $I/I_{sat} \ll 1$, the Beer–Lambert law gives

$$I_{sig}(x,y) = I_{780}(x,y) \exp\left(-\int_{z_{min}}^{z_{max}} \sigma n_{3D}(x,y,z)dz\right), \tag{5.8}$$

where n_{3d} is the atomic density distribution and σ is the absorption cross section, which gives the probability of an atom to be excited by a photon. The directly measured quantities were the transmitted intensities with and without atoms, labelled as I_{sig} and I_{780} respectively. The integral gives the cross section, σ, multiplied by the 2-D cloud profile, n_{2D}, thus, the recorded signal can be processed in the following way

$$\ln I_{sig}(x,y) - \ln I_{780}(x,y) = -\sigma n_{2D}(x,y). \tag{5.9}$$

However, the signal on the photodiode is being integrated over x and y, so eventually the spectrum that is being obtained has the form

$$\ln I_{sig} - \ln I_{780} = -\int \sigma n_{2D}(x,y)dxdy. \tag{5.10}$$

Typical scans, I_{sig} and I_{780}, obtained from the photodiode are presented in figure 5.8. Figure 5.8b shows the variations in the intensity of the probe beam during the scan when no atoms were trapped into MOT (magnetic field was off), the I_{780}. Those variations are caused by the dependence of efficiency of the AOM on the driving RF frequency and the variation of the power of the oscillations with frequency. To obtain a normalised signal eqn. 5.10 is used, and the spectrum is obtained as $\ln \frac{I_{sig}}{I_{780}}$ as in figure 5.8c.

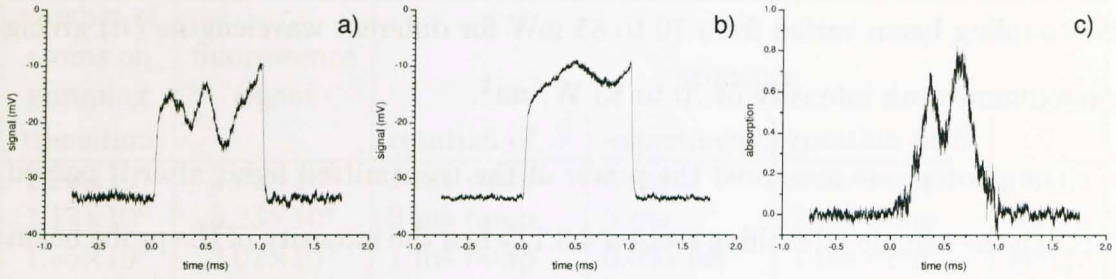

Figure 5.8: Sample raw scans from photodiode: EIT transmission spectrum for $20D_{5/2}$ I_{sig} (a), a background scan I_{780} (b), and obtained spectrum $\ln \frac{I_{sig}}{I_{780}}$ (c).

5.2.3 Characterisation of $|1\rangle \rightarrow |2\rangle$ transition

The first step in collecting the data is to record the absorption of the probe beam without the coupling beam, the $|1\rangle \rightarrow |2\rangle$ transition, referred later as a two-level transition, from which important parameters for this transition (like width and central frequency) can be extracted, that are fed into the fit to obtain the lineshape of EIT spectrum. The intensity of the absorbed light in this transition is described by a Lorentzian function:

$$I_a = A \frac{I/I_{sat}}{1 + I/I_{sat} + 4((\Delta_{12} - x_0)/\Gamma)^2}. \tag{5.11}$$

Here I is the intensity of the laser and $I_{sat} = 1.669$ mW/cm^2 is the saturation intensity for the $|F = 2, m_F = \pm 2\rangle \rightarrow |F' = 3, m'_F = \pm 3\rangle$ transition, Γ is the transition linewidth and Δ_{12} is laser detuning. The parameters that are obtained from the fit are the amplitude A, Γ and central frequency x_0.

An example of two-level absorption spectrum is shown in figure 5.9 together with fitted Lorentzian from equation (5.11). The obtained value of the two-level transition linewidth is 8.5±0.3 MHz for individual scans, and varies from 7.9±0.1 MHz to 10.8±0.1 MHz for averaged scans. This is much greater then expected 6.06 MHz (Gutterres *et al.*, 2002), and although a study of the broadening was not performed in detail two factors could most likely contribute towards it. One is the instability of the frequency of the probe laser, which is measured to be on

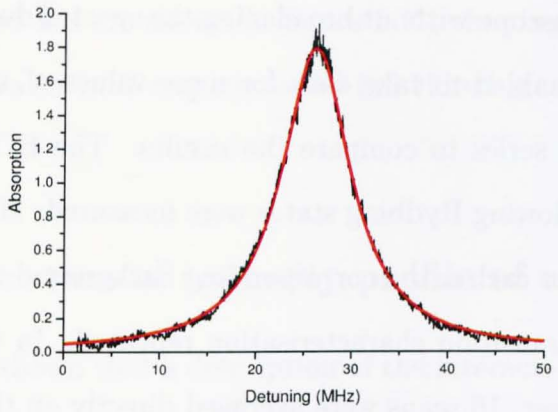

Figure 5.9: Absorption spectrum of two-level system. Black curve is experimental data (after removing background) and red line is a Lorentzian fit.

the order of few hundred kHz, and the second, and more significant, is the bandwidth of the photodiode. As the probe signal is weak, the high-gain photodiode is used with relatively low bandwidth (35 kHz), and thus the recorded signal is broadened. The other sources of the broadening like inhomogeneous magnetic field, Doppler broadening and collisional broadening are almost negligible. However, this discrepancy in the value of the linewidth of $|1\rangle \rightarrow |2\rangle$ transition does not affect the later analysis.

5.2.4 Electromagnetically induced transparency

The scans of EIT spectrum were obtained for different $nD_{5/2}$ states, where n was set to 20, 24, 30, 35, 37, 40 and 42. For each n, the power of the coupling beam was varied from 10 up to 90 mW. This gives from 6 to a dozen of scans from which Ω_c can be extracted. To achieve good statistics 10 scans were taken for each value of the power of the coupling laser. Examples of individual scans are presented in figure 5.10.

A series of measurements were taken by performing a set of individual scans and averaging the obtained parameters *a posteriori*. Later, an improvement on the locking and stabilisation of the blue laser allowed to average the EIT scans

directly on the oscilloscope without broadening the spectra due to laser frequency fluctuations. This enabled to take data for more values of n and also for some n from the previous series to compare the results. The EIT spectra involving transitions to the following Rydberg states were measured: 20, 22, 26, 28, 30, 35, 37, 40, 44 and 48. For each n the corresponding background trace was also taken and the $|1\rangle \rightarrow |2\rangle$ transition characterisation repeated. In this series, for each power of coupling laser, 16 scans were averaged directly on the oscilloscope.

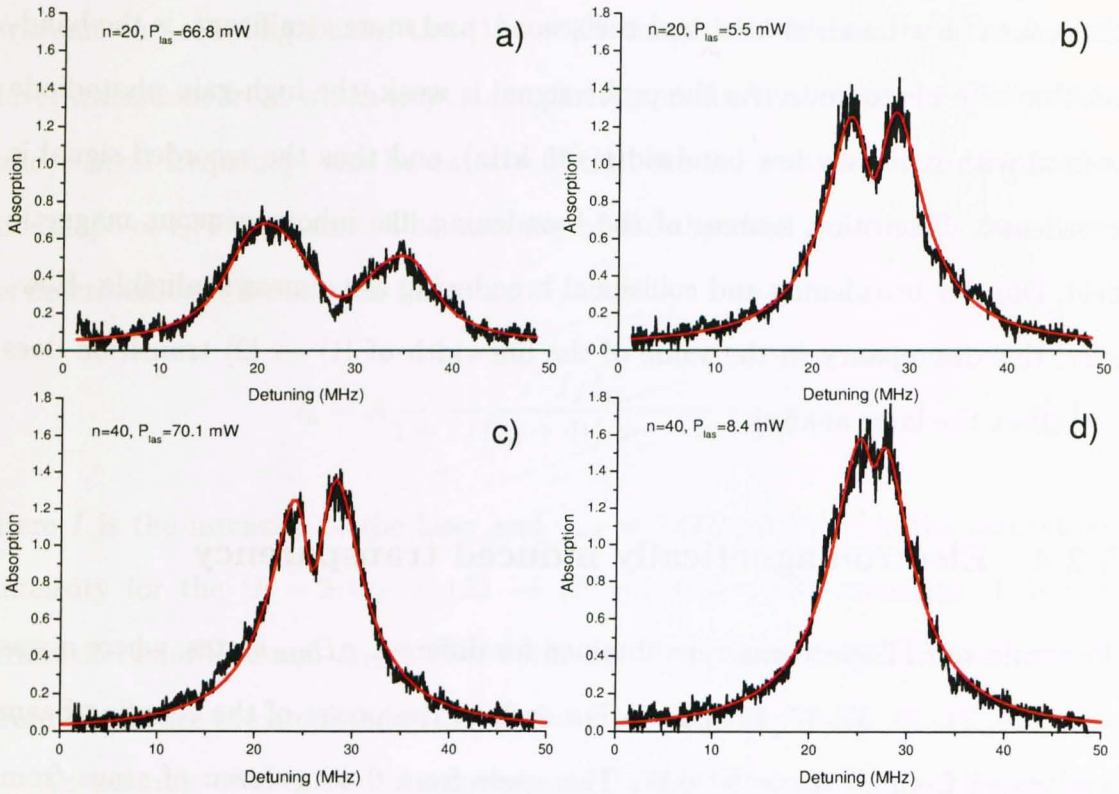

Figure 5.10: Individual EIT scans. Black line shows the experimental curve of absorption profile (after subtracting the background), red curves are profile fits from equation (5.14). Each spectrum is obtained from single scan for different $nD_{5/2}$ state and different power of the coupling beam: a) $20D_{5/2}$ with 66.8 mW in the coupling beam; b) $20D_{5/2}$ with 5.5 mW; c) $40D_{5/2}$ with 70.1 mW; d) $40D_{5/2}$ with 8.4 mW.

Sample scans and fits are shown in figure 5.11, showing an improvement of the signal to noise ratio with respect to the individual scans, thus allowing far more accurate fits.

5.2.5 Consideration of intensity profile of coupling beam

In Chapter 2 it was shown that a description of the interaction of probe and coupling beam with atoms can be obtained by solving the three level Bloch equation. The probe absorption profile is then characterised by the following parameters: Rabi frequencies Ω_p and Ω_c, linewidth of the $|1\rangle \rightarrow |2\rangle$ transition (Γ_{21}), the decoherence of the state $|3\rangle$ (γ_3) and the central frequencies (Δ_p and Δ_c), and is given by the eqn. 2.34. However, the above approach assumes that the intensity of the

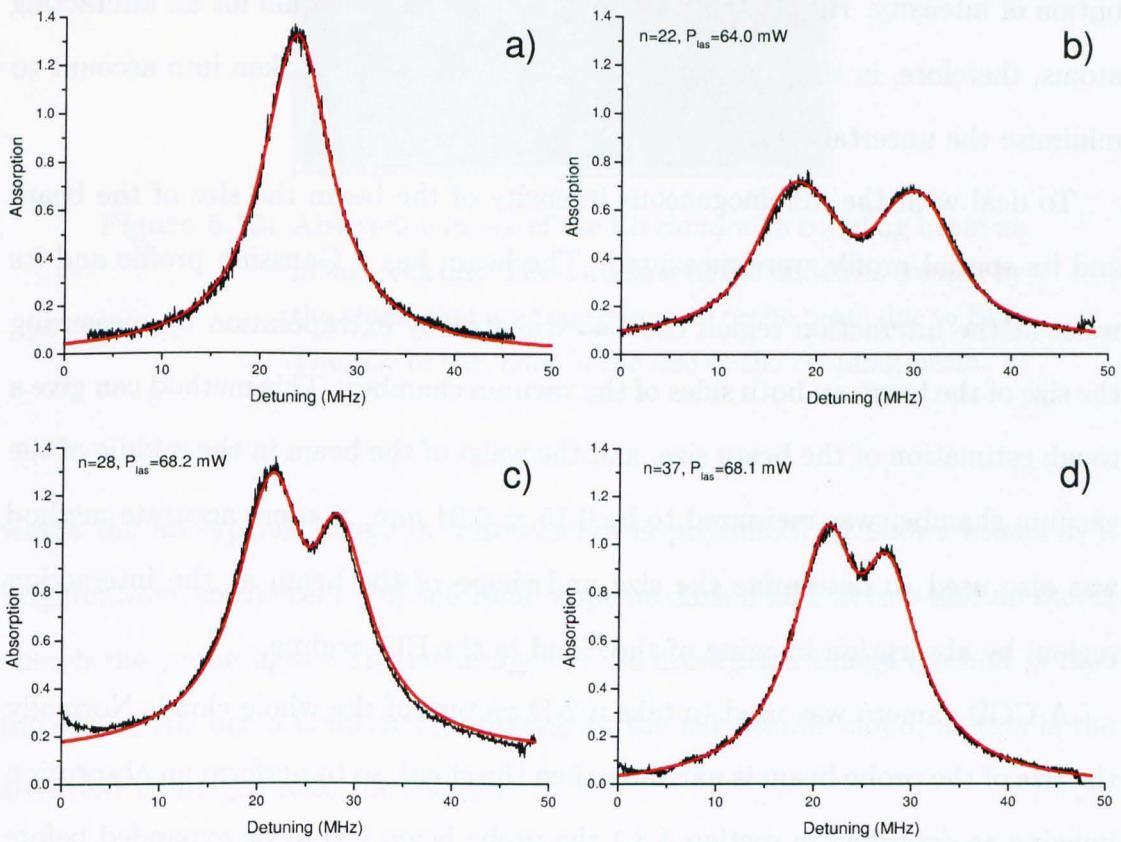

Figure 5.11: Sample two-level (a) and EIT scans (b-d) obtained from averaging 16 scans on the oscilloscope (black lines). Lorentzian (a) and three-level interaction function (5.14) were fitted (red lines) as described in the text.

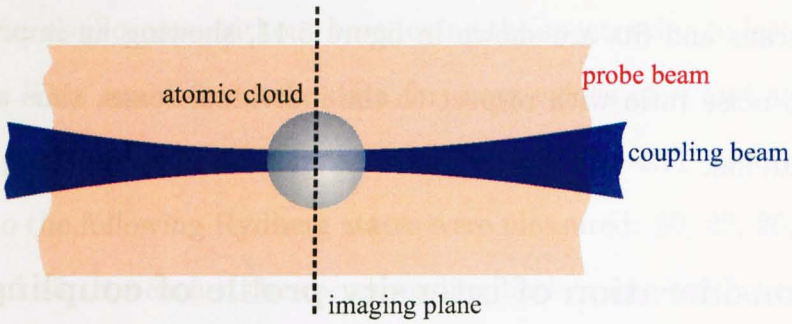

Figure 5.12: Scheme for coupling beam waist measurement. Probe beam is expanded so atomic cloud cast a shadow on a CCD camera. When both probe and coupling beams are tuned to resonances EIT will occur over the coupling beam area.

coupling beam is uniform over the whole interaction region. In the experiment the blue laser is focused on the cloud and therefore has a Gaussian spatial distribution of intensity. Hence, the Rabi frequency, Ω_c, is not equal for all interacting atoms, therefore, in the analysis of the data this has to be taken into account to minimise the uncertainties.

To deal with the inhomogeneous intensity of the beam the size of the beam and its spatial profile were measured. The beam has a Gaussian profile and its waist at the interaction region can be estimated by extrapolation by measuring the size of the beam on both sides of the vacuum chamber. This method can give a rough estimation of the beam size, and the waist of the beam in the middle of the vacuum chamber was measured to be 0.15 ± 0.04 mm. A more accurate method was also used to determine the size and shape of the beam at the interaction region, by absorption imaging of the cloud in the EIT regime.

A CCD camera was used to take a 2-D picture of the whole cloud. Normally the size of the probe beam is narrower then the cloud, so to perform an absorption imaging as described in section 4.3.1 the probe beam has to be expanded before the vacuum cell. The atomic cloud cast a shadow that is imaged on the camera.

To measure the size of the coupling beam at the exact interaction area the following procedure was used. The probe and coupling lasers are exactly at the

two-photon resonance and are aligned with the cloud as in figure 5.12. In this case EIT occurs and atoms that are in the area where the coupling beam crosses the cloud should be fully transparent for the probe beam. If the centre of the atomic cloud is imaged on the camera the atoms that are transparent due to EIT should reflect the profile of the coupling beam. This can be seen in figure 5.13

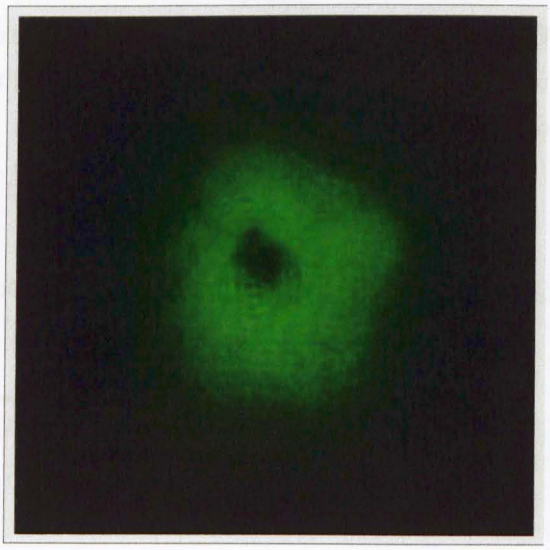

Figure 5.13: Absorption image of the Rb cloud with coupling beam on in false colours. The dark spot in the middle is created by the atoms that are transparent to probe beam due to EIT. The size of the 'hole' is the size of the coupling beam.

where the absorption image in false colours is presented. It shows atoms as a brighter area, so the centre of the cloud appears dark if EIT occurs and no atoms absorb the probe light. The advantage of the absorption image method is that the size of the beam is measured directly at the the atomic cloud, as this is the area that is imaged onto the camera.

The coupling beam is Gaussian, so the hole 'burnt' in the cloud should reflect this profile. To see and fit this profile a row from image in 5.13 was taken and plotted in fig 5.14. This slice cuts the cloud through the centre of the dark spot

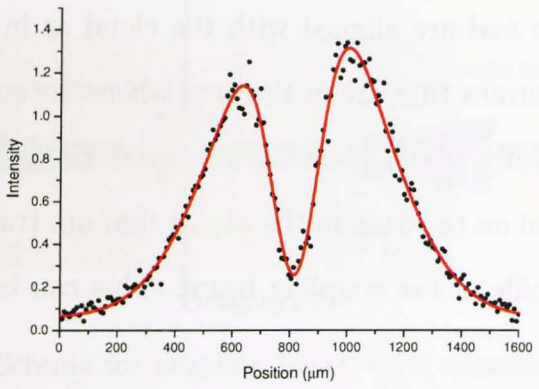

Figure 5.14: Cut through the cloud at centre of the hole with the fit taking into account the profile of the cloud and the profile of the coupling beam.

and gives a cloud profile that shows the dip caused by the coupling laser:

$$I_p(x) = I_{offset} + \overbrace{Ae^{-\frac{(x-x_c)^2}{2\sigma_c^2}}}^{(1)} \overbrace{\left(1 - Be^{-\frac{2(x-x_b)^2}{w_b^2}}\right)}^{(2)} \tag{5.12}$$

where (1) is the profile of the cloud and (2) of the beam. A and B are amplitudes and σ_c is the size of the cloud, σ_b the beam waist and x_c and x_b represent the position of the centre of the cloud and the beam. From the fit the beam waist was measured to be 0.18±0.016 mm. When taking a slice cut in the perpendicular direction it was found out that the coupling beam has elliptical shape and the fitting function of the slice cuts was replaced by the 2-D function fitting the whole 2-D image. From this the beam waists were measured to be $w_x = 175 \pm 23$ μm and $w_y = 243 \pm 39$ μm. The values for the cloud width and centre are obtained from fitting the cloud profile when the blue laser is not on, and were found to be $\sigma_c = 240 \pm 5$ μm, $x_c = 922 \pm 3$ μm, $A = 1.67 \pm 0.08$.

Once the spatial profile of the beam was imaged and measured it was taken into account in the analysis of the EIT/AT signal. For fixed laser intensity the

absorption cross section is given by

$$\sigma = \frac{hf\Gamma^2}{4I_{sat}} \left[\left((\Gamma - 2i\Delta_p) + \frac{\Omega_c^2}{\gamma_3 - 2i(\Delta_p + \Delta_c)} \right)^{-1} + c.c. \right] \tag{5.13}$$

which is derived from section 2.2.1.

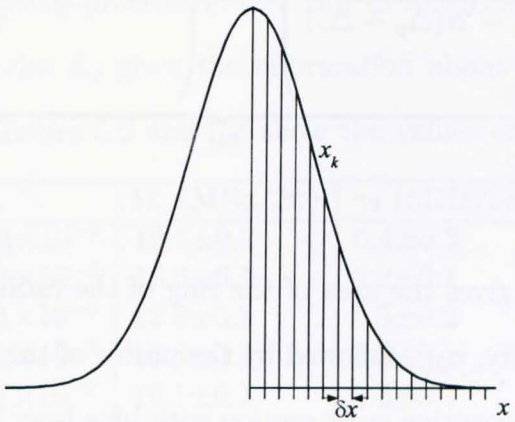

Figure 5.15: The intensity profile of the beam is divided into bins for calculation of the EIT profile.

However, the intensity is not spatially uniform, so atoms at different positions interact with a different range of intensity. Taking this into account is non-trivial and an analytic solution to equation 5.10 cannot be found. Thus the EIT signal is numerically evaluated by considering the contributions from areas of equal intensity and integrating over the beam profile. Figure 5.15 shows a 1-D representation of the discrete binning of the beam, where each division corresponds to a ring of radius x_k with the width δx. In this way the signal is reconstructed by summing the contributions to the EIT signal corresponding to an averaged Rabi frequency over the ring. The number of bins in which the beam is divided is given as $n = \frac{x_{max}}{\delta x} - 1$ and the radius of each ring is $x_k = \left(k + \frac{1}{2}\right) \delta x$. To obtain the shape of the signal the sum of all those contributions is calculated for $x_{max} = 150$ μm with $\delta x = 15$ μm, to give the total signal arriving to the photodiode through the pinhole:

$$I = \sum_{k=0}^{n} \frac{A}{2\Gamma} \overbrace{\pi\left(2x_k\delta x + \delta x^2\right)}^{(1)} \overbrace{\exp\left(-\frac{x_k^2}{2\sigma_x^2}\right)}^{(2)} \overbrace{\exp\left(-\frac{2x_k^2}{w_{780}^2}\right)}^{(3)} \times$$
$$\times \underbrace{\left(\left(\Gamma - 2i\Delta_p + \frac{\left(\Omega_c e^{-\frac{x_k^2}{2w_{480}^2}}\right)^2}{\gamma_3 - 2i(\Delta_p + \Delta_c)}\right)^{-1} + \left(\Gamma + 2i\Delta_p + \frac{\left(\Omega_c e^{-\frac{x_k^2}{2w_{480}^2}}\right)^2}{\gamma_3 + 2i(\Delta_p + \Delta_c)}\right)^{-1}\right)}_{(4)} \tag{5.14}$$

The first term (1) gives the area of the ring of the radius x_k. The next term (2) is the atomic density, n_{2D}, followed by the profile of the probe beam (3). The final term (4) is the absorption cross section with blue laser intensity dependence.

The parameters that are needed to model the signal are A – amplitude, Ω_c – Rabi frequency, σ_x – width of atomic cloud, waists of lasers: w_{780} – probe, and w_{480} – coupling, Γ – linewidth of probe transition, γ_3 – decoherence and Δ_p, Δ_c – central frequency of probe beam and EIT/AT feature. Beam waists and atomic cloud width are known from previous measurements, and the parameters that depend only on the $|1\rangle \rightarrow |2\rangle$ (i.e. Γ, Δ_p) are obtained from fitting the two-level absorption scans as shown in the previous section (5.2.3) and then fed into the fit function for the EIT scans. This decreases the number of free parameters in the fit.

5.2.6 Measurements of the Rabi frequency

The scans were taken for $20 \leq n \leq 48$ and for each n several values of coupling laser power were chosen. Each scan was fitted using the procedure described in previous section with equation 5.14.

There are 4 parameters that are to be fitted in this procedure: A – amplitude, Ω_c – Rabi frequency, γ_3 – decoherence and Δ_c – central frequency of EIT fea-

ture. All the fitting procedures were done using scripts written in Mathematica that allowed initialisation of all parameters and gave visualisation of the data (Appendix A). The initialisation of the parameters is critical to assure that the fitting procedure will converge. The initial value of Rabi frequency was calculated based on the power of the coupling laser. To find the best initialisation value of γ_3 few iterations of fitting procedure were run to find the variation of obtained γ_3. The variation of the Δ_c gives the information about long time stability of the coupling laser. Tables 5.2 and 5.3 show the values of fitted parameters for

n	A	Ω_c (MHz/2π)	γ_3 (MHz/2π)	Δ_c (MHz)
20	$20.6\pm0.03\times10^{-3}$	19.7±0.2	6.4±0.3	-2.60±0.10
22	$1.95\pm0.01\times10^{-3}$	16.6±0.1	5.2±0.1	2.86±0.04
26	$1.72\pm0.01\times10^{-3}$	12.9±0.1	5.5±0.2	0.83±0.06
28	$2.22\pm0.01\times10^{-3}$	10.6±0.1	4.3±0.1	-1.43±0.05
30	$1.91\pm0.01\times10^{-3}$	10.1±0.1	3.8±0.1	0.49±0.06
35	$2.08\pm0.01\times10^{-3}$	7.3±0.1	3.7±0.1	-0.44±0.05
37	$2.36\pm0.01\times10^{-3}$	7.3±0.1	4.9±0.2	-0.98±0.06
40	$2.36\pm0.01\times10^{-3}$	6.9±0.1	5.1±0.1	0.82±0.04
44	$1.29\pm0.01\times10^{-3}$	5.3±0.1	2.9±0.2	0.16±0.08
48	$1.71\pm0.01\times10^{-3}$	4.8±0.1	3.3±0.2	-0.48±0.06

Table 5.2: Fitted parameters with statistical uncertainties for EIT scans for coupling laser power ~50 mW for different n.

P (mW)	A	Ω_c (MHz/2π)	γ_3 (MHz/2π)	Δ_c (MHz)
70.8	$1.73\pm0.01\times10^{-3}$	19.1±0.1	5.4±0.1	2.44±0.04
64.0	$1.82\pm0.02\times10^{-3}$	18.6±0.1	5.7±0.1	-0.47±0.03
60.9	$1.85\pm0.01\times10^{-3}$	17.8±0.1	5.1±0.1	0.83±0.03
48.1	$1.95\pm0.01\times10^{-3}$	16.6±0.1	5.2±0.1	2.86±0.04
37.9	$1.93\pm0.01\times10^{-3}$	14.4±0.1	4.5±0.1	1.04±0.04
28.9	$2.00\pm0.01\times10^{-3}$	12.1±0.1	4.5±0.1	0.79±0.05
15.3	$2.12\pm0.01\times10^{-3}$	10.0±0.1	4.3±0.2	1.90±0.09
10.2	$2.27\pm0.01\times10^{-3}$	7.8±0.2	4.6±0.3	2.13±0.09
4.6	$2.59\pm0.01\times10^{-3}$	4.8±0.2	4.0±0.4	0.6±0.1

Table 5.3: Fit parameters for EIT scans for n=22 for different coupling laser power.

selected traces. Table 5.2 shows the variation of parameters with the principal quantum number n for the coupling laser power 50 mW. It can be noticed that

obtained values of γ_3 slightly depend with n, and is higher for low n. In table 5.3 values of the parameters for $n = 22$ are presented. Here, γ_3 shows a slight dependence on the power of the coupling beam. The values of Ω_c show the dependence on both n and coupling laser power and will be treated in more details in the next paragraphs.

There was a slight difference in obtaining the parameters for the two data sets. For averaged scans fits were performed and the uncertainties are taken from the fitting model, while for data set of individual scans fit was obtained for each spectrum and then the averaged values of γ_3 and Ω_c were taken with standard deviations as uncertainties. The high noise level in the individual scans makes the fit more difficult.

5.3 Obtaining dipole moments

Equation 5.7 shows that Rabi frequency is proportional to the square root of power with the linear coefficient proportional to the dipole moment. In this section dipole moments for transitions to $nD_{5/2}$ will be extracted from experimental data exploiting this relation.

5.3.1 Rabi frequency vs. laser power

Figure 5.16 shows the measured Rabi frequencies as a function of $\sqrt{P}$ plotted for all n. The graph clearly shows the linear dependence of the Rabi frequency on the square root of the power of the coupling laser. For each n a linear fit was performed to extract the value of angular coefficient. Table 5.4 shows the values of the parameters of the fitted lines.

The data show two features, firstly the slopes of the lines decrease with n, and secondly the intercept is close to zero. Ideally the intercept should be zero, as for zero laser power the Rabi frequency is zero, and this is zero for all n within the statistical error (see table 5.4).

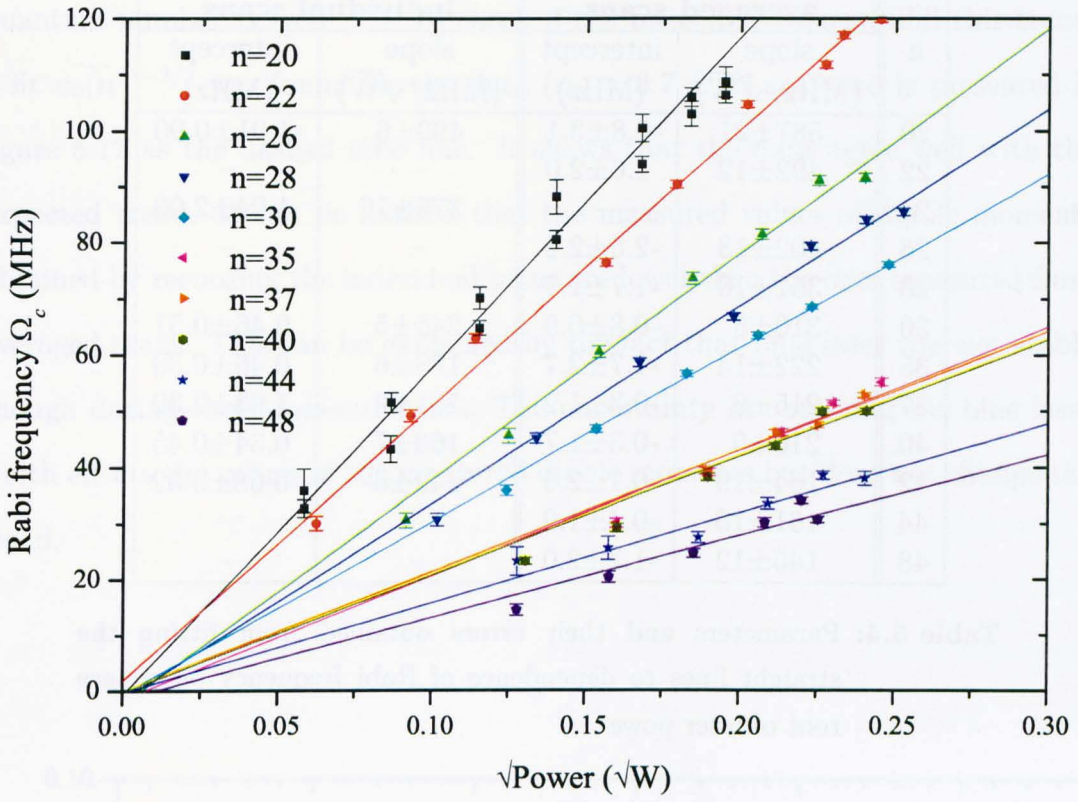

Figure 5.16: Measured Rabi frequencies vs. $\sqrt{P}$. Each point is the Rabi frequency obtained for EIT scan. For each nD state linear fit was found (lines) which gradient is proportional to dipole moment of the $5P_{3/2} \rightarrow nD_{5/2}$ transition.

5.3.2 Dipole moments

Following equation 5.7 the dipole moments for each transition $|5P_{3/2}\rangle \rightarrow |nD_{5/2}\rangle$ can be obtained from the measured gradients in table 5.4. From this follows that

$$\langle 5P_{3/2}||e\vec{r}||nD_{5/2}\rangle = d \times \hbar\sqrt{\frac{3}{8}w_x w_y \pi \epsilon_0 c}, \tag{5.15}$$

where d is the gradient obtained from the fit to the datasets as shown in the previous paragraph and w_x and w_y are the coupling laser waists.

Table 5.5 shows the measured values together with their uncertainties for each Rydberg state. The uncertainties are obtained as standard errors from the fitting procedure. However, from eqn. 5.15, it is clear that the dipole moment depends strongly on the measured value of coupling laser size. The uncertainty

n	averaged scans		individual scans	
	slope (MHz/$\sqrt{\text{W}}$)	intercept (MHz)	slope (MHz/$\sqrt{\text{W}}$)	intercept (MHz)
20	587±21	-0.8±3.1	499±6	-1.01±0.90
22	492±12	1.6±2.0	–	–
24	–	–	376±16	1.04±2.00
26	402±13	-2.5±2.2	–	–
28	351±10	-1.7±1.7	–	–
30	310±5	-0.8±0.9	245±5	0.46±0.51
35	222±14	-1.7±2.7	198±6	0.46±0.39
37	215±6	-0.3±1.2	151±9	1.03±2.30
40	210±9	-0.3±1.7	160±7	0.34±0.45
42	164±10	-0.1±2.0	142±6	-0.68±0.52
44	161±10	-0.4±1.9	–	–
48	146±12	-1.7±2.0	–	–

Table 5.4: Parameters and their errors obtained from fitting the straight lines to dependence of Rabi frequency on square root of laser power.

averaged scans		individual scans	
n	μ_{ab} (ea_0)	n	μ_{ab} (ea_0)
20	0.084±0.006	20	0.072±0.007
22	0.071±0.006	22	–
24	–	24	0.054±0.009
26	0.058±0.006	26	–
28	0.050±0.005	28	–
30	0.044±0.004	30	0.035±0.004
35	0.032±0.004	35	0.028±0.004
37	0.031±0.003	37	0.022±0.004
40	0.030±0.003	40	0.022±0.003
42	0.024±0.003	42	0.021±0.003
44	0.023±0.003	44	–
48	0.021±0.003	48	–

Table 5.5: Measured dipole moments for $5P_{3/2} \rightarrow nD_{5/2}$ transitions.

of evaluation of the beam size is about 15% so for dipole moments for low n it is dominant over the statistical uncertainty from the fits. The dependence of the measured dipole moments on the effective principal quantum number is shown in figure 5.17 for both series of the data – obtained from individual and averaged EIT scans. The dependence of the radial matrix element on the effective principal

quantum number is $(n^*)^{-3/2}$. To check if the measured values fulfill this trend, a fit $n_0(n^*)^{-3/2}$ was found for the data ($n_0 = 6.7 \pm 0.1\, ea_0$) and is presented in figure 5.17 as the dashed blue line. It shows that the data agree well with the expected trend. It can be noticed that the measured values of dipole moments obtained by recording the individual scans are lower then the ones measured from averaged scans. This can be explained by the fact that blue laser was not stable enough during those measurements. The uncertainty in obtaining the blue laser width effects the values of the measured dipole moments but does not change the trend.

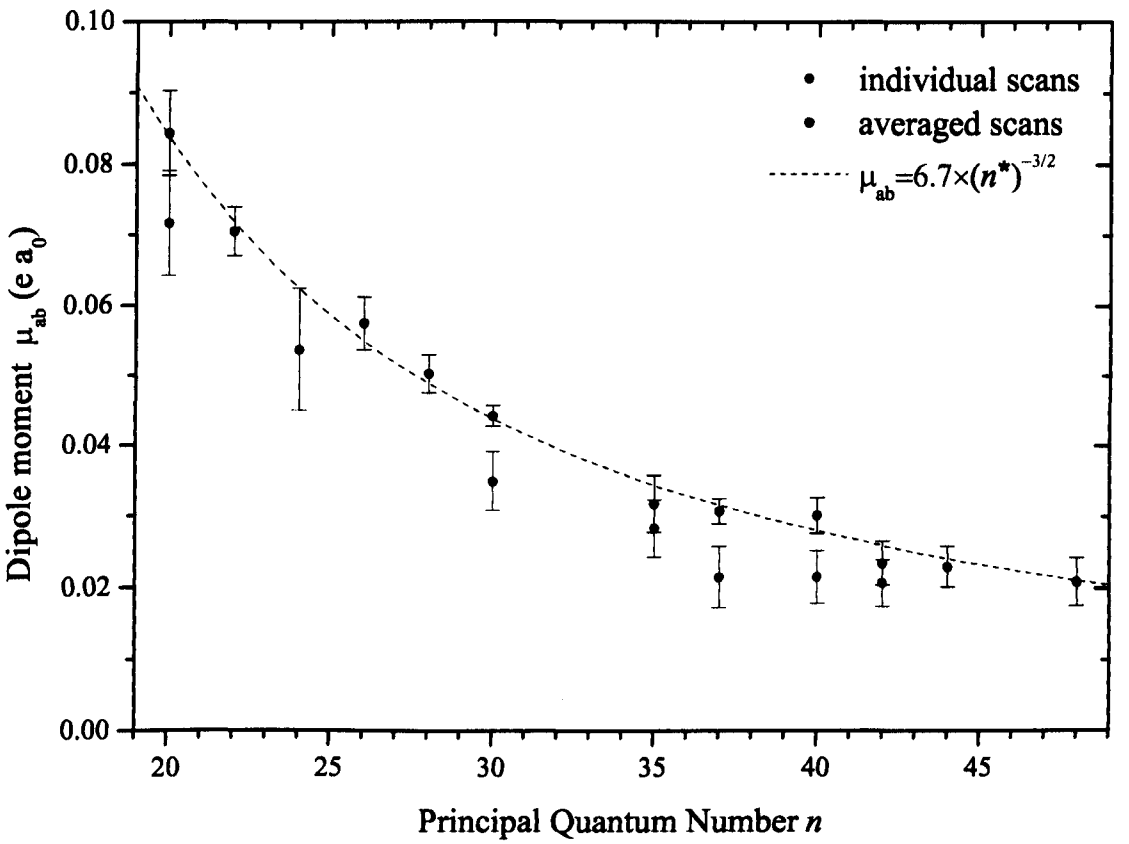

Figure 5.17: Measured dipole moments for $5P_{3/2} \rightarrow nD_{5/2}$ transitions. Black points were obtained from fitting the average of 16 EIT scans while gray points were obtained by recording 10 individual EIT scans and then getting fit parameters.

5.4 Comparing the results to the theory

Radial matrix elements for the transitions between $5P$ state and Rydberg states were calculated by Beterov (2010) using the quasiclassical model by Dyachkov and Pankratov (1994). The radial matrix elements for transitions between Rydberg states of alkali metals are usually calculated by integrating the Schrödinger's equation in Coulomb approximation of using various model potentials (Bates and Damgaard, 1949; Theodosiou, 1984; Gounand, 1979), but for highly-excited states the precision in obtaining the rapidly-oscillating wave functions limits the reliability of these methods. In quasiclassical methods the radial matrix elements are calculated avoiding the direct numerical integration using transcendental functions. This improves both speed and reliability of the calculations. The model

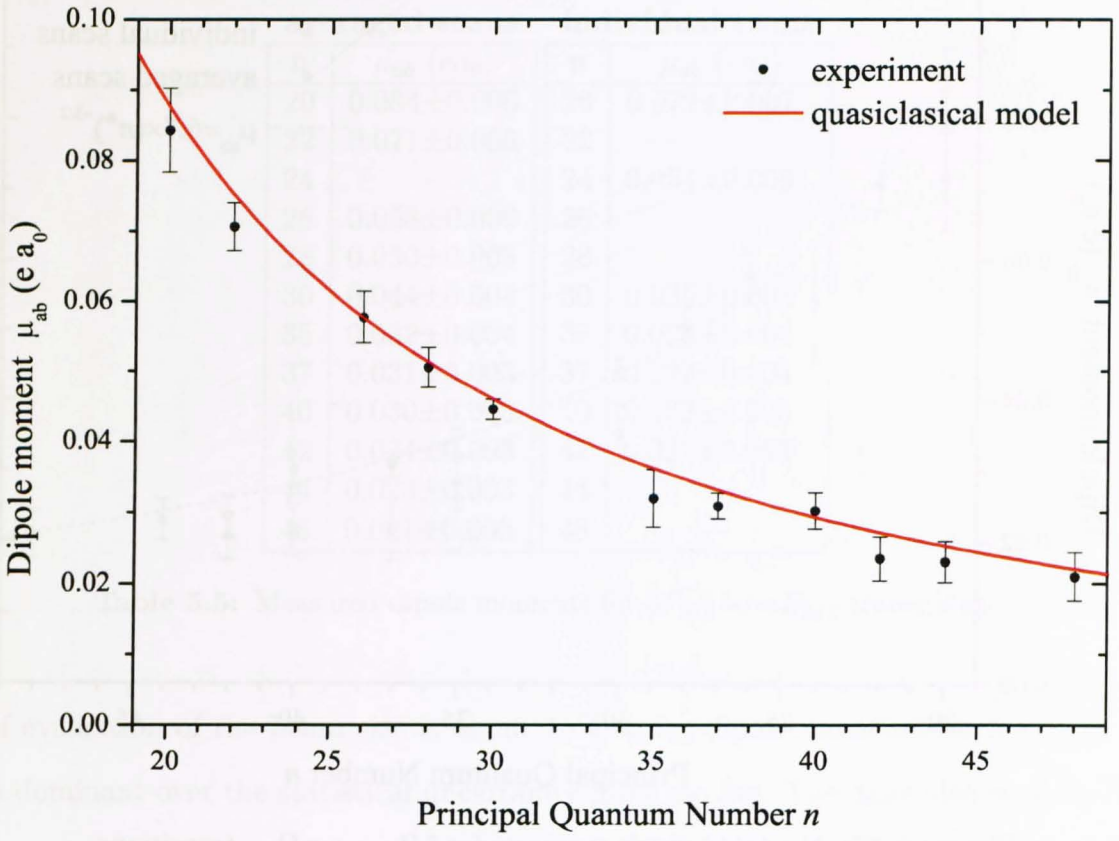

Figure 5.18: Measured dipole moments for $5P_{3/2} \rightarrow nD_{5/2}$ transitions compared to theoretical calculations by Beterov (2010) – red solid line.

proposed by Dyachkov and Pankratov uses the quasiclassical method, where the electron is described in terms of a mean energy and mean effective principal quantum number of the two states for which matrix element is to be calculated. The graph in figure 5.18 shows the comparison of the theoretical and measured values of dipole moments, which are also listed in table 5.6. The values of calculated dipole moments of the transitions to Rydberg states are presented as the thick dashed line. For higher values of n the method is estimated to have 10% uncertainty. It can be seen that measured values agree very with quasiclassical calculations.

n	μ_{ab} (ea_0)	n	μ_{ab} (ea_0)
20	0.085	35	0.035
22	0.073	37	0.032
24	0.063	40	0.028
26	0.056	42	0.026
28	0.049	44	0.024
30	0.044	48	0.021

Table 5.6: Calculated dipole moments for $5P_{3/2} \rightarrow nD_{5/2}$ transitions (Beterov, 2010).

5.5 Conclusion

In this chapter the measurements of dipole moments for transitions to Rydberg states for rubidium were presented. The results were obtained by exploiting the dependence of the shape of AT splitting on the Rabi frequency and the fact that Rabi frequency is proportional to radial matrix elements. A method of fitting EIT/AT scans that takes into account the spatial profile of the coupling beam was used. The measured dipole moments were compared with theoretical calculations by semiclassical method and were found to be in excellent agreement.

CHAPTER 6

Design of a New Vacuum Chamber

The vacuum chamber used for the experiments described in this thesis does not allow to prepare very small ensembles of atoms to investigate the collective states and local blockade effects, which were described in chapter 3. This chapter will briefly describe the design of a new vacuum chamber in which such experiments will be carried out. To perform future experiments the new apparatus has to be capable of detection of Rydberg atoms by field ionisation. An additional requirement is a high spatial resolution, that allows to resolve atoms separated by approximately 50 μm.

6.1 Ideas behind design of a new chamber

The future experiments to be conducted in the laboratory are focused on the observation of the interactions amongst Rydberg atoms in a high-density atomic sample, where a suppression of multiple excitations should be observed, leading to a collective excited state. To perform those experiments high-density atomic ensembles are needed, where the number of trapped atoms is controllable. As shown in Schlosser *et al.* (2001) dipole traps can be exploited and a 'collisional

blockade' mechanism is used to lock the number of trapped atoms to a specific value by simply tuning the loading rate. Multiple traps can be created, each containing a controllable number of atoms sharing a single excitation, and the interactions amongst such prepared clouds can be studied. The new apparatus will be used for experiments that require detection of Rydberg atoms via selective field ionisation. To look at the local blockade or collective state excitation phenomena between closely spaced samples a detection system has to be able to resolve atoms separated by approximately tens μm.

Those three requirements lay behind the development of the new chamber and will be described in more details in the following paragraphs.

6.1.1 Optical system

To confine a controllable number of atoms in high-density sample a dipole trap is used. In a dipole trap the trapping force arises from the dispersive interaction of the induced atomic dipole moment with intensity gradient of the light field and this technique can be used for optical dipole trapping of neutral atoms. A detailed review of optical dipole traps can be found in Grimm *et al.* (2000). The atoms are loaded into the dipole trap following a preliminary cooling stage in a MOT. In order to enable the high collisional rate required to achieve a controllable number of atoms, the trapping volume must be very small and the beam waist has to be on the order of 1 μm. This can be done by using a multi-lens system, like in Schlosser *et al.* (2001), or using just a single lens (Sortais *et al.*, 2007). The optical system for dipole trap has to be designed very carefully and the complexity of a multi-lenses system is due to the need of a high numerical aperture (NA) optical system that should perform at the diffraction limit over a large spectral range, so that both the dipole trap beam (far red detuned from resonance) and the fluorescence light (at resonance) from atoms can be routed through the same lenses. However, commercial large NA aspheric lenses can be used to simplify

the system. The advantage of the single-lens solution is its ease of assembly, it requires, however, to put the lens very close to interaction region, as the focal lengths of such lenses are on the order of few mm.

6.1.2 State-selective field ionisation

The other aspect that has to be taken into account when designing the new chamber is the detection of the Rydberg atoms. As they are very highly excited atoms, the electron is loosely bound and it is very easy to ionise them, so field ionisation is the most common method for detection (Singer *et al.*, 2004; Löw *et al.*, 2007). The ionisation energies of rubidium Rydberg states vary from around 40 meV for n=20 to around 2 meV for n=80. In state-selective field ionisation (SFI) the electric field is applied which ionise only those Rydberg atoms, whose energies are above the given threshold. An electric field introduces a saddle point to the Coulomb potential at an energy of $E_{SP} = -6.12\sqrt{F}(cm^{-1})$, where F is electric field given in V/cm (Gürtler and van der Zande, 2004). All the atoms with energy greater then E_{SP} are ionised as they are coupled to the continuum. If the applied electric field is slowly ramped (at the rate of few hundred V cm^{-1} μs^{-1}) the population of the states is ionised at the classical field ionisation threshold, $F = 1/16n^4$ (in atomic units) (Gürtler and van der Zande, 2004). This gives the values of electric fields of 10 to 2000 V/cm for $n \simeq 80$ to $n \simeq 20$. The ions or electrons produced by field ionisation can then be detected by micro-channel plates detectors (MCPs).

6.1.3 High spatial resolution detection

In the situation where the spatial resolution and sensitivity of detection are very important, as when the position of single ions with an accuracy of few micrometres needs to be resolved in the experiment, a detection system has to be carefully designed. For the experiments where local blockade or collective excitation is

observed, the distance over which the interactions are observed is of the order of few micrometres for non-resonant (van der Waals) interactions and tens of micrometres for resonant interactions (Gaëtan *et al.*, 2009; Urban *et al.*, 2009), thus the detection system has to be able to spatially resolve atoms in nearby traps. In the next section a preliminary design based on field ionisation and electrostatic lenses is presented, that could enable to achieve a spatial resolution that allows for resolving ions separated by 10–100 μm.

6.2 Simulations of a detection system

The main challenge in designing the detection system is the fact that single Rydberg atoms separated by tens of micrometres need to be resolved. Ionisation of the atoms and acceleration of the ions towards the MCP is sufficient to detect the ion. Time of flight (TOF) measurements could distinguish between atoms at different locations, but only in one dimension. The detection system described here uses electrostatic lenses, that can route the ions apart and image them at distances of 100–200 μm and thus allows to detect the the atoms position in a 2-D plane.

For the simulation of the detection system a commercial software, Charged Particles Optics (CPO), was used. Giving as input positions, sizes and voltages applied to electrodes of different shapes, CPO traces the movement of a charged particle from the given input positions. The software uses the Boundary Element Method (BEM) to find electrostatic potentials and fields for systems of conducting electrodes. This method is described in details in Read *et al.* (1971) and Harting and Read (1976). In short, it relies on the fact that in a system of conducting electrodes the charges appear on their surfaces when potentials are applied. These surface charges are then the sources of all the potentials and fields in the system, so in the BEM the electrodes are effectively replaced by these charges.

Before showing the realisation of detection system, a description of electrostatic lenses has to be made.

6.2.1 Electrostatic lenses

Similarly to optical lenses, electrostatic lenses are used to shape, magnify or demagnify beams of electrons or ions, but unlike light optics the factor that reflects the beam is not the interface between two media but an electrostatic field, but the principles of electron/ion lenses are analogous to the optical ones. There are 4 common geometries of electrostatic lenses: double-cylinder, triple-cylinder, double-aperture and triple-aperture. Aperture and cylinder lenses, apart from their geometry, have similar properties, but cylinder lenses tend to be stronger and have lower aberrations. However, aperture lenses are more compact physically, and this is the main reason why the system described here will use aperture lenses. Here, the difference between double- and triple-aperture lenses will be briefly described.

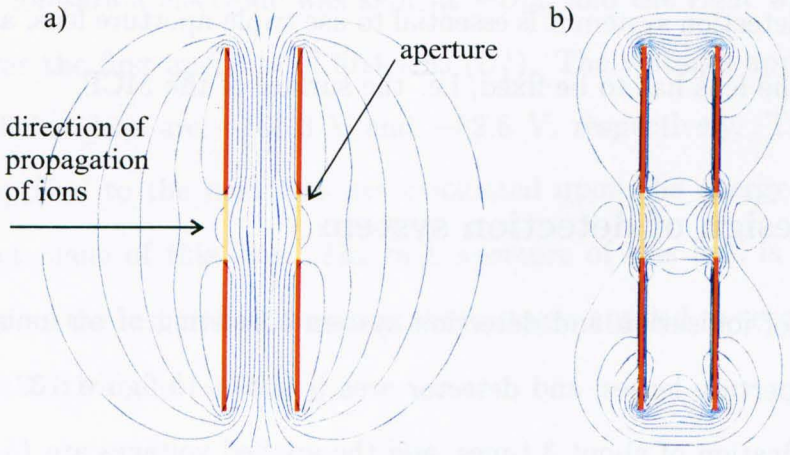

Figure 6.1: Potential a) and electric field b) around double-apertures lens simulated with CPO.

For a double-aperture lens two electrodes are held at potentials U_1 and U_2 ($U_1 \neq U_2$) where U_1 and U_2 correspond to the initial and final energy, respectively. Field distribution in such a lens leads to a focussing effect but it changes the

energy of electrons as well (see figure 6.1). The focal lengths of this lens depends on the ratio U_2/U_1. These values can be found in Harting and Read (1976).

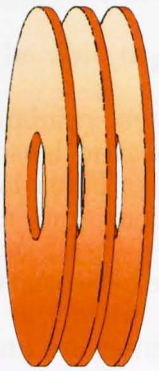

Figure 6.2: Triple-aperture lens

The main difficulty in double-aperture lenses is of not being able to change the overall acceleration ratio without changing the image position, but this can be overcome by introducing an additional aperture so the lens becomes a triple-aperture lens (figure 6.2). This kind of lens is a zoom lens, and by changing U_3/U_1 ratio and potential U_2 one can keep the position of image in the same place.

For the detection system it is essential to use triple-aperture lens, as the image position of the lens has to be fixed, i.e. the surface of the MCP.

6.2.2 Design of detection system

The design of ionisation and detection system consisting of an ionisation area, two triple-aperture lenses, and detector area is shown in figure 6.3. Both lenses have magnification of about 3 times, and the applied voltages are $U_2 = 10 \times U_1$, $U_3 = 5 \times U_1$.

Firstly, the ionisation electric field was being applied between the back of ionisation area and the first lens' most left electrode, however this was not producing uniform enough field in the ionisation area, so extra ionisation plates, made of mesh, were added. They have 5 cm diameter and the field produced by the lenses

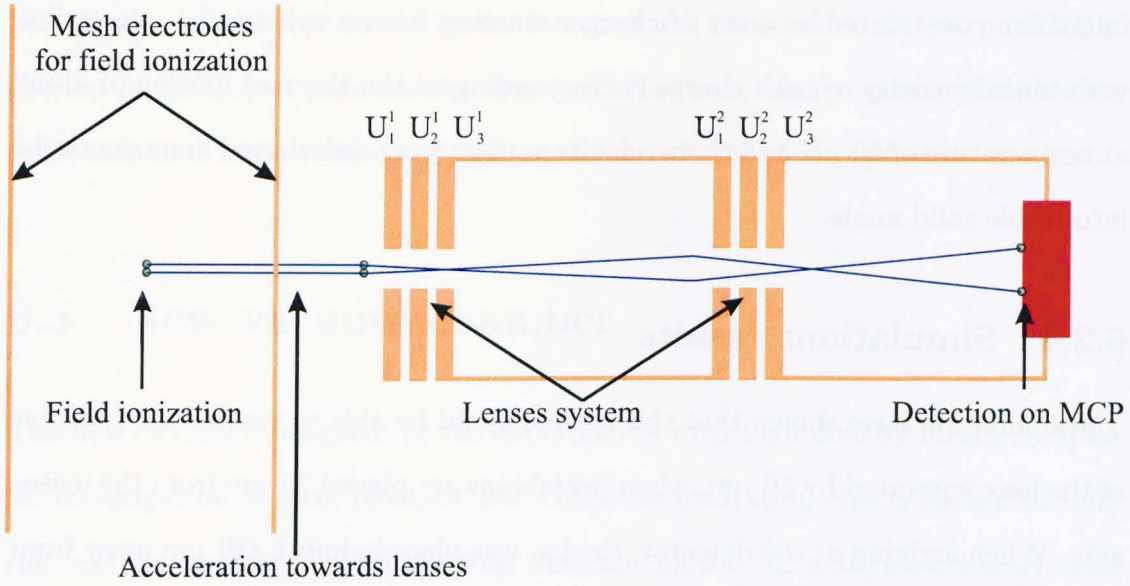

Figure 6.3: Scheme of detection system. Ions are produced in ionisation region and have to be transferred to the object plane, which is the surface of MCP.

is uniform within the region where atoms will be ionised. It is important to reassure the uniform ionisation field, so the produced ions will travel only in direction parallel to the lenses axis without gaining any acceleration in off-axis direction.

The left ionisation electrode was kept at $-U_{ion}$ and the right was grounded at 0V, so was the first aperture of first lens (U_1^1). The voltages applied to next apertures of first lens are -186.3 V and -82.8 V, respectively. The values of potentials applied to the next lens are calculated upon the energy of the ions in the object plane of this lens. The first aperture of this lens is kept at the same voltage as the last in first lens, and the voltages applied to second lens are: -82.2 V, -1252.1 V and -720.6 V.

6.2.3 Preparation of ions for simulation

In order to simulate the ion's path has to assume an isotropic velocity distribution and that the ion will have the same initial velocity as the atom. It is also important to take into account the size of the trap and the effect that the ion can be initially placed within some area. Thus, the simulations were performed for the

initial ion constructed as a set of charges starting from a sphere of 1 μm radius with initial velocity of each charge corresponding to the thermal motion of atom at temperature of 50 μK and their velocity vectors were distributed homogenously into whole solid angle.

6.2.4 Simulations results

The simulation have shown that this system could be able to resolve the position of the ions separated by 50 μm, when initial ions are placed 25 μm from the lenses axis. When arriving at the detector, the ion was placed almost 380 μm away from the axis and the area on which the ions hit the detector was circular with 23.5 μm diameter. The spread of the position in which the ion hits the detector is due to different starting points and different vectors of initial velocity of the ion. This means that the initial ion starting from a sphere of the diameter of 2 μm on the detector plane will arrive within the circle of diameter of 23.5 μm (see figure 6.4). This would suggest that ions spaced even by a few of microns should be resolvable. This result was obtained for ionisation field of 30 V/cm, which corresponds to ionisation of the $n \sim 65$ state. For different values of the field the

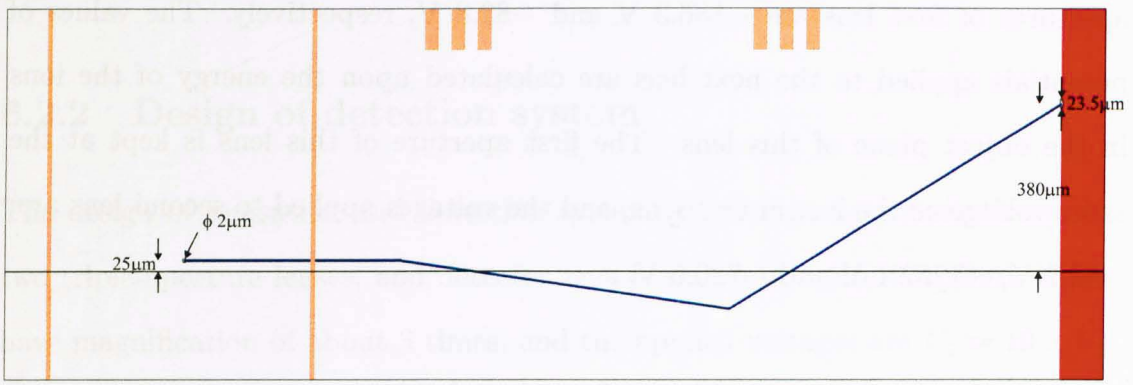

Figure 6.4: Ions starting from position 25 μm from lenses axis are imaged on the MCP at the distance of 380 μm. Horizontal dimensions are not to scale. The system has cylindrical symmetry around the lens system optical axis so the ion produced at position 25 μm below the axis will end up on the MCP at position -380 μm.

acceleration of the ions in the ionisation area will cause the different position of the ion in the object plane of the first lens. However, higher values of ionisation field, and thus lower n involved, will make the spread of ions position smaller.

6.3 New vacuum chamber

The new chamber designed for the experiments with high density atoms samples for investigation of local blockade and collective excitation effects should include the lens for creation of dipole trap and the ionisation and detection system. However, placing the lens inside the vacuum chamber, very close to the ionisation region, will cause that charges will induct on the surface of the lens. To avoid it one can shield the lens, but this will compromise the quality of the focused beam, and thus affect the performance of the dipole trap. However, if two lenses are placed into the system, symmetrically spaced from the symmetry axis of the ionisation electrodes, the net effect of the charges collected on each of the lenses will be minimised.

The design of the new chamber was done together with Chris Hall from S&T Workshop, who was also in charge for machining all needed parts. The centre of the design is the Kimball 8 Multi-CF Spherical Octagon chamber (MCF800-SO200800) that has two 8" CF view-ports and eight 2¾ CF side ports. The biggest challenge was to place into the chamber all the parts, i.e. ionisation plates, dipole trap lenses mounted on a metal tube, and MCPs, in such a way, that full optical access was enabled, in particular for the 3 pairs of MOT beams and the extra beams for excitation, probing etc. The design is presented in figure 6.5. The magnetic coils for MOT field will be placed outside the chamber. The designed chamber does not host the electrostatic lenses system for position depended detection of ions, but the space was left inside to allow adding it at the later stage.

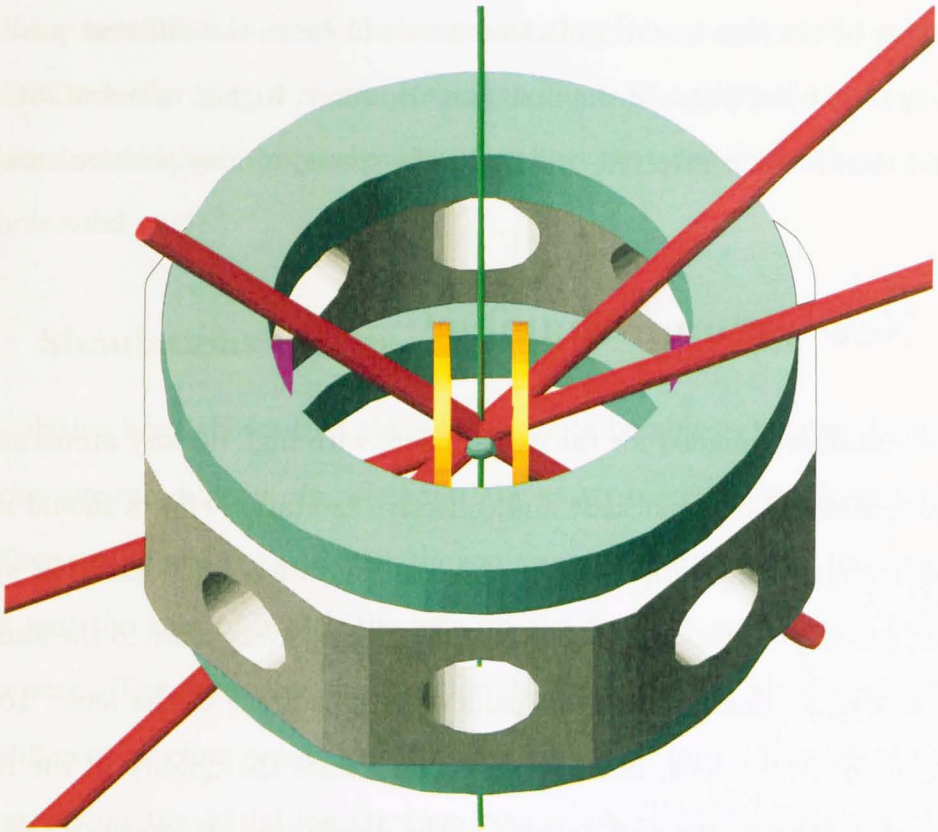

Figure 6.5: The CAD design of the new chamber. Red lines show the paths of the MOT beams, green is the excitation laser. Aspheric lens for creation of dipole trap is shown as a blue part in the middle of the chamber between two ionisation mesh-plate (yellow).

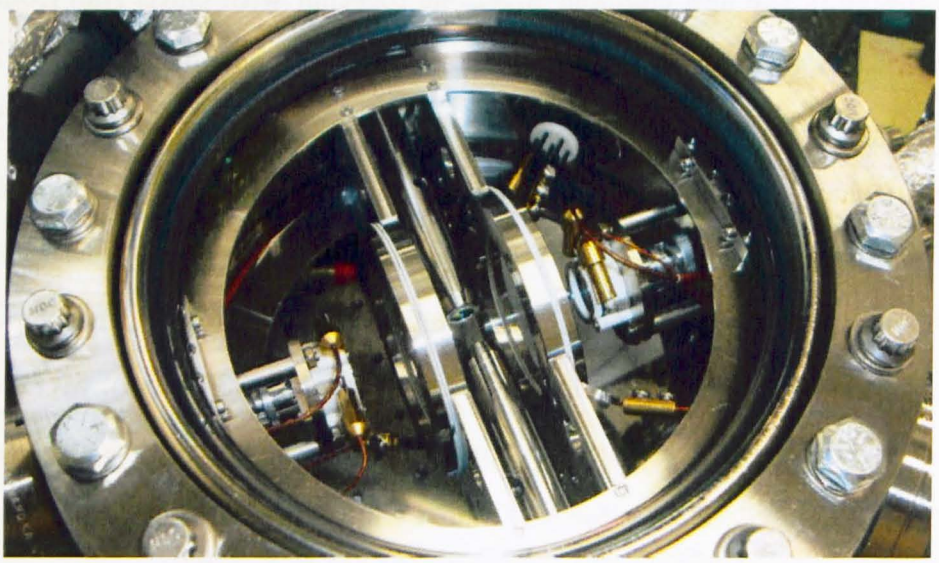

Figure 6.6: The photography of the new chamber.

The chamber is now assembled, and a photo of it, with all parts inside, is presented in figure 6.6. A the time of writing this thesis the chamber was being backed to achieve the ultra-high vacuum. Two of the eight 2¾ CF view-ports are used to mount MCPs and through the two perpendicular ports dipole trap will be created by the aspheric lens from Light Path. The two aspheric lenses are mounted on the metal tubes that shield them from the electric field and allow positioning. Two mesh electrodes are mounted for field ionisation. The other side ports are used for electric feeds and as auxiliary access ports. The MOT beams will be accessed through 8 in. view-ports.

The first goal with the new chamber is to create the dense atomic sample in dipole traps and observe the EIT in this conditions. Recently Pritchard *et al.* (2010) demonstrated that interactions between Rydberg states in dense samples can affect the observed EIT signal, by suppressing it. Also the effect of the external electric field on the EIT signal can be observed.

6.4 Conclusions

In this chapter the design of a new system for investigation of high density atomic samples with controllable number of atoms created in dipole trap was presented. The atoms will be excited to Rydberg states allowing direct observation of Rydberg-Rydberg interactions. Simulations showed that the high spatial resolution detection system for Rydberg atoms can be obtained, capable of resolving atoms separated by 50 μm.

CHAPTER 7

Conclusions

Ultracold Rydberg atoms are a relatively new field of research, which has attracted interest in recent years particularly because of its potential applications in the field of quantum computing and in the study of many-body systems. The strong, long range interactions that these system display can be studied in a new regime, where the atoms are virtually at rest. Crystal-like structures can be created where the atoms are confined in space and arranged in arbitrary geometries and the interactions amongst them can be switched on and off at will and tuned finely. The unprecedented level of control that can be achieved in these systems and the low level of decoherence they display, has allowed scientists to achieve atom-atom entanglement and quantum gate operation (Isenhower *et al.*, 2010; Wilk *et al.*, 2010; Zhang *et al.*, 2010) using single atoms in microscopic dipole traps. However, because of the loading mechanisms that single atoms trapping relies on, the scalability of these systems is still an issue. Alternatively, single excitations can be achieved in mesoscopic samples of atoms exploiting a blockading of multiple excitations enabled by the interactions themselves. Besides of the more straightforward preparation, collective excitations in mesoscopic samples also have the potential of enhancing the capabilities of these systems, by

strengthening the interactions. Despite the envisaged potential of collective excitations in mesoscopic samples, an experimental demonstration has not been achieved yet.

A new experimental facility has been developed in the course of this PhD, that allows for the study of collective excitations to Rydberg states in mesoscopic samples of cold Rubidium atoms in dipole traps and it further enables the control of the interactions amongst them. A laser cooling setup for rubidium atoms was designed and implemented, that allowed to produce a sample of 3×10^6 atoms at temperatures of few microkelvins and a laser system for coherent excitation to Rydberg states was realised. Despite the numerous challenges and the heavy requirements that such systems have, the experimental setup proved to be successful and enabled the direct measurement of transition dipole moments from the first excited state to high n Rydberg states exploiting Autler-Townes splitting. The measured values were found to be in excellent agreement with quasiclassical model developed by the collaborators from the group in Novosibirsk. To the author's knowledge, these are the first direct measurements of such dipole matrix elements and, besides proving the reliability of the measurements method, they are extremely useful to validate theoretical models and to gain insight in the physics of the interactions that will be studied. The results of this thesis are being prepared to be published. Future work will also include the application of similar methods to detect Rydberg-Rydberg interactions within a mesoscopic sample in a non-destructive manner.

In this thesis the theoretical description of the interaction of coherent light with atoms for two-level atom is presented, which is then extended to the three-level system. In this system the coherent effects like electromagnetically induced transparency (EIT) and Autler-Townes (AT) splitting can occur, which facilitated the measurements of the transition dipole moments. The most relevant properties

of Rydberg atoms are also described and all the relevant literature review is outlined.

Any laser cooling experiment requires very narrow laser sources, which were implemented using commercially available diode lasers and mounting them in a home-built extended cavity with diffraction grating which was exploited to lock the lasers via a saturated absorption signal, reducing the linewidth to less then 500 kHz. A magneto-optical trap was implemented and the measurements for its characterisation in terms of the density and temperature are presented, which allowed for the optimisation of the experimental sequence to maximise the number and density of atoms trapped in the MOT, as well as to minimise their temperature.

A crucial part of the experiment was to build a stable two-photon laser source for coherent excitation of the sample via a two-steps ladder scheme. The system implemented consisted of a high-power laser at 480 nm and a 780 nm source. The 780 nm light was derived from a diode laser mounted on extended cavity to allow for frequency stabilisation, whilst the 480 nm light was obtained from a commercial frequency doubled, amplified laser diode system. The 780 nm source was first stabilised using a frequency modulation transfer technique and used to enable an EIT signal to lock the 480 nm laser source.

Direct measurements of dipole moments for transitions from state $|5P_{3/2}\rangle$ to $|nD_{5/2}\rangle$, where $n = 20 - 48$ were performed. The measurement technique exploits the dependence of the Autler-Townes splitting on the Rabi frequency of the transition in question. The dependence of Rabi frequency on the power of laser beam allows to obtain the dipole moments of transitions. The sample was prepared by optical pumping to a specific Zeeman state with an efficiency of 80%. This allowed to target a specific transition which simplifies the analysis of the traces. However, it was not possible in the setup to completely select the Rabi frequency for the transition involved because of the inhomogeneity of

the coupling laser beam intensity. Nonetheless the intensity profile was taken into account in the analysis of the trace and it was found that the experimental results were in very good agreement with the theoretical calculations obtained by the use of quasiclassical model. A brief description of the model as well as a discussion of the results are also presented.

The last chapter presents the design of a new vacuum and detection system in which the future experiments will be performed. As it was signaled in this thesis the future work will focus on the investigation of local blockade and the behaviour of collective states. The new chamber enables the creation of dipole trap where small, controlled number of atoms can be trapped. The successful implementation of the cold atoms facility and the achievement of the first application of EIT/AT to measure transition dipole moments have encouraged the group to perform further experiments based on EIT on a small sample of atoms the regime of high density and strong Rydberg interactions. Those interactions should affect the shape of the observed signals. The effects of arbitrary external electric field would be also possible to observe.

Further down the line, the long-term goal is to observe a single collective excitation in a small number of atoms trapped in a dipole trap. One can envisage how more dipole traps could be added, to create a register (or array) of dipole traps that can be individually controlled to study and control the interactions amongst them. This could enable the creation of a quantum processor based on Rydberg blockade effect.

APPENDIX A

Mathematica Scripts for Data Analysis

In this appendix a sample of the scripts written in Mathematica are presented. The scripts automatised the fitting procedures of the EIT/AT spectra described in chapter 5. The first script is an example of fitting individual EIT scans for n=20 and obtaining the linear dependence of Rabi frequency vs. $\sqrt{\text{laser power}}$. The script was also used to visualise the data. The second script was used to calculate the dipole moments based on the values obtained from the fits.

Michal J. Piotrowicz, Calum MacCormick

Fitting EIT data for ^{87}Rb $|5P_{3/2}\rangle \rightarrow |nD_{5/2}\rangle$ transition

Functions to get the data

In[1]:=
```
Needs["ErrorBarPlots`"]
```

In[2]:=
```
Const = {c0 → 2.99792458 × 10^8, ħ → 1.054571596 × 10^-34, ε0 → 8.854187817 × 10^-12,
  kB → 1.3806504 × 10^-23, a0 → 5.291772083 × 10^-11, qe → 1.602176462 × 10^-19}
```

Out[2]=
```
{c0 → 2.99792 × 10^8, ħ → 1.05457 × 10^-34, ε0 → 8.85419 × 10^-12,
 kB → 1.38065 × 10^-23, a0 → 5.29177 × 10^-11, qe → 1.60218 × 10^-19}
```

In[3]:=
```
SetDirectory[
 "c:\\Documents and Settings\\Michal\\My documents\\OU\\LabData\\20091010_EIT_part_II\\Renamed\\"]
```

Out[3]=
```
c:\Documents and Settings\Michal\My documents\OU\LabData\20091010_EIT_part_II\Renamed
```

In[4]:=
```
DataLabels[type_, n_, J_, Pol_] :=
 If[ToString[type] == "EIT", {StringTake[#, {3, 4}], StringTake[#, {8, 10}], StringTake[#, {15, 15}],
     StringTake[#, {17, 20}], StringTake[#, {28, 28}], DateString[FileDate[#]]} & /@
   FileNames[ToString[StringForm["n=``_J=``_Sig``*_``*.csv", n, J, Pol, type]]],
  {StringTake[#, {3, 4}], StringTake[#, {8, 10}], StringTake[#, {15, 15}],
     StringTake[#, {17, 20}], DateString[FileDate[#]]} & /@
   FileNames[ToString[StringForm["n=``_J=``_Sig``*_``.csv", n, J, Pol, type]]]]
DataLabels[type_, n_, J_, Pol_, Pow_, no_] := If[ToString[type] == "EIT",
  {StringTake[#, {3, 4}], StringTake[#, {8, 10}], StringTake[#, {15, 15}],
     StringTake[#, {17, 20}], StringTake[#, {28, 28}], DateString[FileDate[#]]} & /@
   FileNames[ToString[StringForm["n=``_J=``_Sig``_``mW_``_``.csv", n, J, Pol, Pow, type, #]] & /@ no]]
```

In[6]:=
```
CreateFileName[n_, J_, Pol_, Pow_, type_, no_] :=
 If[
  ToString[type] == "EIT"
  , ToString[StringForm["n=``_J=``_Sig``_``mW_``_``.csv", ToString[n],
    ToString[J], ToString[Pol], ToString[Pow], ToString[type], ToString[no]]],
  ToString[StringForm["n=``_J=``_Sig``_``mW_``.csv", ToString[n], ToString[J],
    ToString[Pol], ToString[Pow], ToString[type], ToString[no]]]
 ]
CreateFileName[n_, J_, Pol_, Pow_, type_] :=
 If[
  ToString[type] == "EIT"
  , ToString[StringForm["n=``_J=``_Sig``_``mW_``_*.csv",
    ToString[n], ToString[J], ToString[Pol], ToString[Pow], ToString[type]]],
  ToString[StringForm["n=``_J=``_Sig``_``mW_``.csv", ToString[n],
    ToString[J], ToString[Pol], ToString[Pow], ToString[type]]]
 ]
```

In[8]:=
```
CreateData[n_, J_, Pol_, Pow_, type_, no_, first_, last_] :=
 Take[Transpose[
   Take[
    Import[
     CreateFileName[n, J, Pol, Pow, type, no]
    ], {first, last}
   ]
  ], {4, 5}
 ]

CreateData[n_, J_, Pol_, Pow_, type_, first_, last_] :=
 Take[Transpose[
   Take[
    Import[
     CreateFileName[n, J, Pol, Pow, type]
    ], {first, last}
   ]
  ], {4, 5}
 ]
```

In[10]:=
```
DataOffset[n_, J_, Pol_, Pow_, type_, first_, last_] :=
 Mean[Take[CreateData[n, J, Pol, Pow, type, 1, first, last][[2]], {first, last}]]
```

In[11]:=
```
Profile[n_, J_, Pol_, Pow_, type_, no_, rate_, first_, last_] :=
 Transpose[{{rate CreateData[n, J, Pol, Pow, BKG, 1, first, last][[1]],
    Log[(CreateData[n, J, Pol, Pow, BKG, first, last][[2]] - DataOffset[n, J, Pol, Pow, BKG, 1, 400])
      / (CreateData[n, J, Pol, Pow, type, no, first, last][[2]] - DataOffset[n, J, Pol, Pow, BKG, 1, 400])]}]
```

Define the rates for each data set.

Normally I'd use 5.8279*4*(5.25 - 3.25)/0.001. $1000 * 10.6\,x\,3.5$ comes from the set-up with the mini-circuits VCO.

In[12]:=
```
rate1 = 5.7984 * 2 * 4.2 / 0.001 (* 2*5.7984 (3.2) / 0.001 *);
rate2 = 5.7984 * 2 * 4.2 / 0.0005;
rate3 = 5.7984 * 2 * 4.2 / 0.002;
```

Parameters

In[15]:=
```
nn = 20;
JJ = 2.5;
PolPol = P;
```

In[18]:=
```
Powers = #[[4]] & /@ DataLabels[SIG, nn, JJ, PolPol]
```

Out[18]=
```
{06.5, 10.6, 15.7, 25.7, 37.2, 50.2, 60.1, 71.2, 78.6}
```

In[19]:=
```
IlyasData = Transpose[{{20, 22, 24, 26, 28, 30, 32, 35, 37, 40, 42, 44, 48}, {0.085, 0.07278, 0.06325,
     0.05563, 0.04944, 0.04432, 0.04002, 0.03476, 0.03187, 0.02821, 0.02615, 0.02433, 0.02126}}];
```

In[20]:=
```
CorrectionFactor = 1 / 1.1774
```

Out[20]=
```
0.849329
```

3 | *Individual EIT analysis n=20.nb*

Good files to be processed

In[21]:=
```
FilesToTake = {
   {"06.5", {0, 1, 2, 3, 4, 5, 6, 7, 8, 9}},
   {10.6, {0, 1, 2, 3, 4, 5, 6, 7, 8, 9}},
   {15.7, {0, 1, 2, 3, 4, 5, 6, 7, 8, 9}},
   {25.7, {0, 1, 2, 3, 4, 5, 6, 7, 8, 9}},
   {37.2, {0, 1, 2, 3, 4, 5, 6, 7, 8, 9}},
   {50.2, {0, 1, 2, 3, 4, 5, 6, 7, 8, 9}},
   {60.1, {0, 1, 2, 3, 4, 5, 6, 7, 8, 9}},
   {71.2, {0, 1, 2, 3, 4, 5, 6, 7, 8, 9}},
   {78.6, {0, 1, 2, 3, 4, 5, 6, 7, 8, 9}}
  };
```

Fitting the two level atom lineshapes

Two level atom and one field lineshape and fit function

In[22]:=
```
FivePTwoLevel = A (Ilas/Isat) / (1 + Ilas/Isat + ((2 (Δ12-x0))/Γ)^2) /. {Ilas → 95 × 10^-9 / (π (0.364/1000)^2), Isat → 16.67};
```

In[23]:=
```
FitTwoLevel[n_, J_, Pol_, Pow_, type_, no_, rate_, first_, last_, Γ00_, x00_, A00_] := NonlinearModelFit[
   Profile[n, J, Pol, Pow, type, no, rate, first, last], FivePTwoLevel, {{Γ, Γ00}, {A, A00}, {x0, x00}}, Δ12];
```

Put the function to work for ALL data

In[24]:=
```
FitData2Lev = FitTwoLevel[#[[1]], #[[2]], #[[3]], #[[4]], SIG, 1, rate1, 780, 1750, 8.3, 26, 300] & /@
   DataLabels[SIG, nn, JJ, PolPol];
```

In[25]:=
```
AVals = A /. (#["BestFitParameters"] & /@ FitData2Lev)
ΓVals = Γ /. (#["BestFitParameters"] & /@ FitData2Lev)
x0Vals = x0 /. (#["BestFitParameters"] & /@ FitData2Lev)
```

Out[25]= {116.978, 101.657, 106.398, 120.349, 120.422, 105.802, 117.317, 111.737, 99.4903}

Out[26]= {8.65608, 8.74645, 8.22708, 8.55936, 8.419, 8.48405, 8.49081, 8.43591, 8.3626}

Out[27]= {26.2853, 26.4703, 26.3643, 26.3858, 26.1535, 26.3746, 26.2059, 26.279, 26.1817}

In[28]:=
```
Table[
 Show[
  ListPlot[Profile[nn, JJ, PolPol, DataLabels[SIG, nn, JJ, PolPol][[n, 4]], SIG, 1, rate1, 780, 1750]],
  Plot[Evaluate[FitData2Lev[[n]][x]], {x, 0, 50}, PlotStyle → Directive[Red, Thick]], ImageSize → Tiny
 ], {n, 1, Length[FitData2Lev]}
]
```

Out[28]=

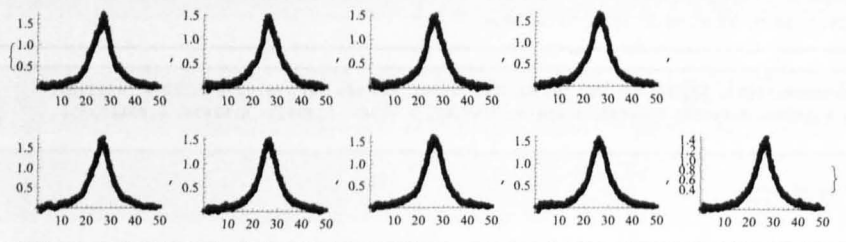

This is supposed to show that our data is normally distributed. I chopped the possible values to get rid of some data- this is the data where "rate" is different to the standard, hence using the fit function above I get the wrong width etc. Also, the range is wrong so the fit is not optimum.

In[29]:=
```
Show[
 Histogram[Select[Abs[ΓVals], Abs[#] < 10 &], {0.2}],
 Plot[0.2 Length[Select[ΓVals, Abs[#] < 10 &]] 1/(2 π StandardDeviation[Select[ΓVals, Abs[#] < 10 &]]^2)
   Exp[-(x - Mean[Select[ΓVals, Abs[#] < 10 &]])^2/(2 StandardDeviation[Select[ΓVals, Abs[#] < 10 &]]^2)], {x, 7, 10},
  PlotStyle → Directive[Red, Thick], PlotRange → Full], PlotRange → All, Frame → True, Axes → False]
```

Out[29]=

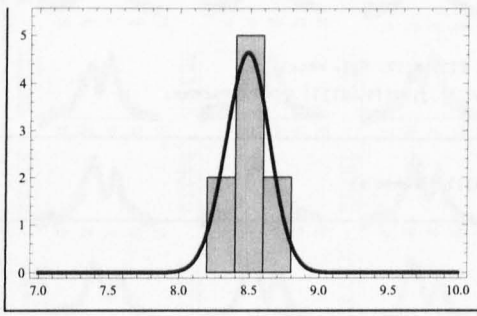

Load data

In[30]:=
```
Inits = Transpose[{x0Vals, AVals, ΓVals}];
```

In[31]:=
```
lst = Flatten[DataLabels[EIT, nn, JJ, PolPol, #[[1]], #[[2]]] & /@ FilesToTake, 1];
```

In[32]:=
```
FitParams =
  Table[{lst[[n]], Inits[[Position[ToExpression[FilesToTake], ToExpression[lst[[n]][[4]]]][[1, 1]]]]},
   {n, 1, Length[lst]}];
```

Fitting the EIT lineshapes

Three level atom and two fields lineshape and fit function

In[33]:=
```
Signal[{A_, Ω23_}, {σx1_, WaistRed_, WaistBlue_}, {Γ_, γ3_}, {Δ12_, Δ23_}, xmax_, w_] :=
 Sum[-(A/(2 Γ) (π (2 x w + w^2)) Exp[-x^2/(2 σx1^2)] Exp[-2 x^2/WaistRed^2])
   (-(Γ - 2 i Δ12 + (Ω23 Exp[-2 x^2/WaistBlue^2])^2/(γ3 - 2 i (Δ12 + Δ23)))^-1 -
    (Γ + 2 i Δ12 + (Ω23 Exp[-2 x^2/WaistBlue^2])^2/(γ3 + 2 i (Δ12 + Δ23)))^-1) /. {x → x + w/2}, {x, 0, xmax, w}]
```

5 | *Individual EIT analysis n=20.nb*

In[34]:=
```
FitEIT[n_, J_, Pol_, Pow_, type_, no_, rate_, first_, last_, Δ2300_, Ω2300_, γ3100_, x00_, Γ00_, A00_] :=
  NonlinearModelFit[Profile[n, J, Pol, Pow, type, no, rate, first, last],
   {offset2 + Signal[{B, Ω23}, {330, 364, √(175 * 243)}, {Γ00, γ3}, {δ - x00, Δ}, 150, 15]},
   {{offset2, 0.1}, {B, 0.001}, {Ω23, Ω2300}, {γ3, γ3100}, {Δ, Δ2300}}, δ];
```

Put the three EIT fit function to work (again, for all data).

In[35]:=
```
FitDataEIT = Block[{DM, power, InitialRabi},
    DM = Select[IlyasData, #[[1]] == nn &][[1, 2]];
    power = CorrectionFactor ToExpression[#[[1, 4]]];
    InitialRabi = a0 qe DM / (2 π w0 ħ √(3/8 π ε0 c0)) √(0.001 power) /. Const /. w0 → √(175 * 243);
    FitEIT[#[[1, 1]], #[[1, 2]], #[[1, 3]], #[[1, 4]], EIT, #[[1, 5]], rate1,
     780, 1750, 0, InitialRabi, 3, #[[2, 1]], Abs[#[[2, 3]]], #[[2, 2]]] & /@ FitParams;
```

In[36]:=
```
DataLabelsPower[type_, n_, J_, Pol_, Power_] :=
 Select[DataLabels[type, n, J, Pol], ToExpression[#[[4]]] == Power &]
```

In[37]:=
```
Sets[count_] := Block[{Pow},
   Pow = ToExpression[Powers[[count]]];
   Show[
      ListPlot[Profile[nn, JJ, PolPol, #[[4]], EIT, #[[5]], rate1, 780, 1750]],
      Plot[Evaluate[Transpose[Select[
            Transpose[{DataLabels[EIT, nn, JJ, PolPol], FitDataEIT}], ToExpression[#[[1, 4]]] == Pow &]][[
          2, ToExpression[#[[5]]] + 1]][Δ12]], {Δ12, 0, 50}, PlotStyle → Directive[Red, Thick]],
      ImageSize → Tiny
     ] & /@ DataLabelsPower[EIT, nn, JJ, PolPol, Pow]
  ];
```

In[38]:=
```
Sets[#] & /@ Range[Length[Powers]] // TableForm
```

Out[38]//TableForm=

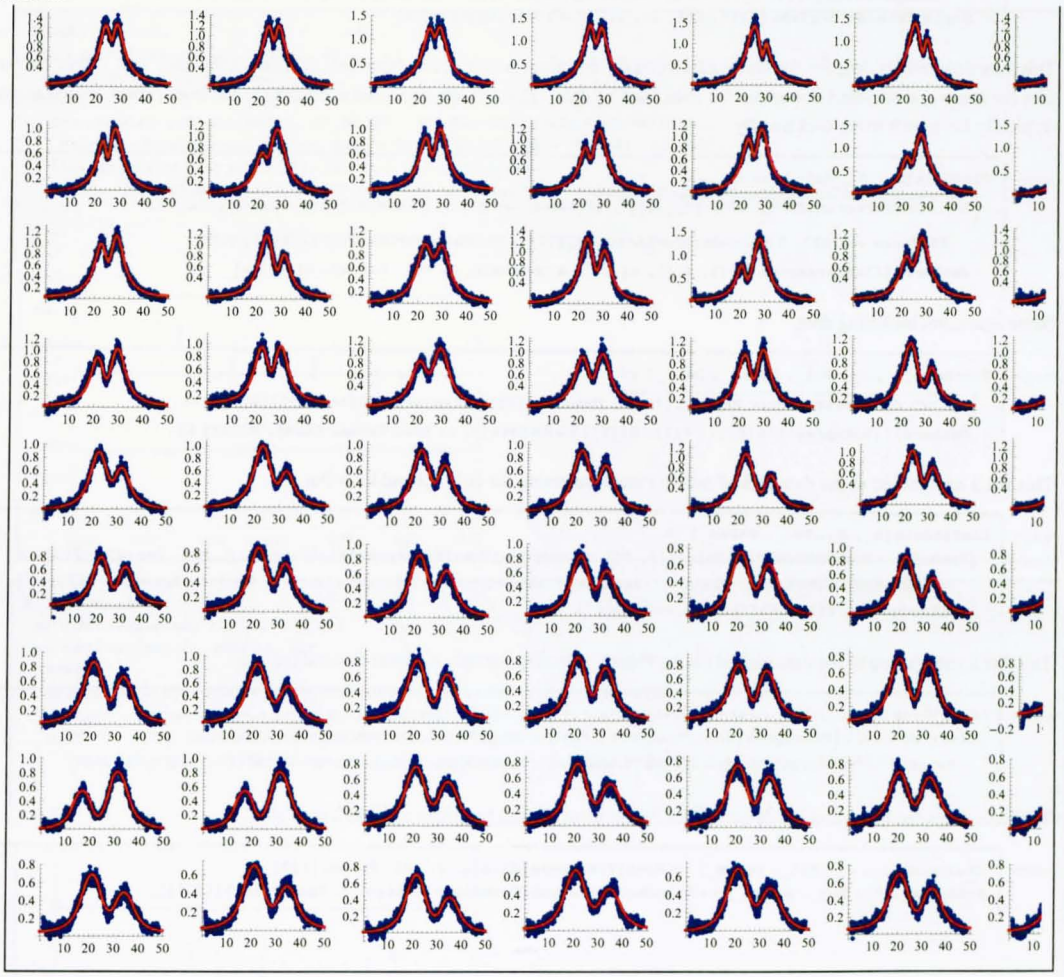

Functions to process the data

This function creates data for the listed parameters, n=principle quantum number, J=electronic angular momentum, Pol= laser polarisation, Param=Parameter needed (e.g. Ω23).

In[39]:=
```
data[n_, J_, Pol_, Param_] := Select[Select[
    Select[Transpose[{DataLabels[EIT, nn, JJ, PolPol], Param /. #["BestFitParameters"] & /@ FitDataEIT}],
     ToExpression[#[[1, 1]]] = n &], ToString[#[[1, 3]]] = ToString[Pol] &], ToExpression[#[[1, 2]]] = J &]
```

This function selects data for the listed parameters, n=principle quantum number, J=electronic angular momentum, Pol= laser polarisation, Param=Parameter needed (e.g. Ω23) and file date. String trim removes the white spaces from the ends of the String-Take which means no padding is needed for e.g. " 4 NOV".

7 | *Individual EIT analysis n=20.nb*

In[40]:=
```
data[n_, J_, Pol_, Param_, Date_] := Select[Select[Select[
    Select[Transpose[{DataLabels[EIT, nn, JJ, PolPol], Param /. #["BestFitParameters"] & /@ FitDataEIT}],
     ToExpression[#[[1, 1]]] == n &], ToString[#[[1, 3]]] == ToString[Pol] &], ToExpression[#[[1, 2]]] == J &],
  StringTrim[StringTake[#[[1, 6]], {4, 10}]] == ToString[Date] &]
```

This function creates data for the **ErrorListPlot** function, which needs {abscissa, ordinate, error bar} and I have chosen to take the mean and standard deviations for each "set" of data. The sets are organised according to the laser power, which groups the (typically 10) points using **GatherBy**.

In[41]:=
```
PlotData[n_, J_, Pol_, Param_] :=
 {Sqrt[0.001 CorrectionFactor Mean[#][[1]]], If[Param === Q23, 2 π Mean[#][[2]], Mean[#][[2]]],
    If[Param === Q23, 2 π StandardDeviation[#][[2]], StandardDeviation[#][[2]]]} & /@
  GatherBy[{ToExpression[#[[1, 4]]], #[[2]]} & /@ data[n, J, Pol, Param], #[[1]] &]
```

Same again, but including date.

In[42]:=
```
PlotData[n_, J_, Pol_, Param_, Date_] :=
 {Sqrt[0.001 CorrectionFactor Mean[#][[1]]], Mean[#][[2]], StandardDeviation[#][[2]]} & /@
  GatherBy[{ToExpression[#[[1, 4]]], #[[2]]} & /@ data[n, J, Pol, Param, Date], #[[1]] &]
```

This fits a straightline to the data picked out by Param, selecting for only n,J and laser Pol.

In[43]:=
```
LinFitData[n_, J_, Pol_, Param_] :=
 (FitModel = LinearModelFit[Join[{{0, 0}}, Transpose[Take[Transpose[PlotData[n, J, Pol, Param]], 2]]], x,
    x, Weights -> Join[{1}, Flatten[Transpose[Take[Transpose[PlotData[nn, JJ, PolPol, Param]], -1]]]^-1];
  {FitModel[x], FitModel["ParameterErrors"]})
```

This fits a straightline to the data picked out by Param, selecting for only n,J laser Pol and the date.

In[44]:=
```
LinFitData[n_, J_, Pol_, Param_, Date_] :=
 LinearModelFit[Transpose[Take[Transpose[PlotData[n, J, Pol, Param, Date]], 2]], x, x,
   Weights -> Flatten[Transpose[Take[Transpose[PlotData[n, J, Pol, Param, Date]], -1]]]^-1][x]
```

This calculates the mean and std deviation for Param form all data for given n, J and laser Pol.

In[45]:=
```
MeanValue[n_, J_, Pol_, Param_] := Mean[Transpose[data[n, J, Pol, Param]][[2]]];
StdDev[n_, J_, Pol_, Param_] := StandardDeviation[Transpose[data[n, J, Pol, Param]][[2]]];
```

Process the data

In[47]:=
```
Block[{mw, sd},
 mw = MeanValue[nn, JJ, PolPol, B];
 sd = StdDev[nn, JJ, PolPol, B];
 Show[
  ErrorListPlot[PlotData[nn, JJ, PolPol, B], PlotStyle → Directive[Blue],
   Joined → False, Frame → True, Axes → False, PlotRange → {0.0005, 0.002}],
  Plot[{mw - 3 sd, mw, mw + 3 sd}, {x, 0, 0.3}, PlotStyle →
    {Directive[Red, Thick], Directive[Lighter[Blue, 0.5], Thick], Directive[Orange, Thick]}]
 ]
]
```

Out[47]=

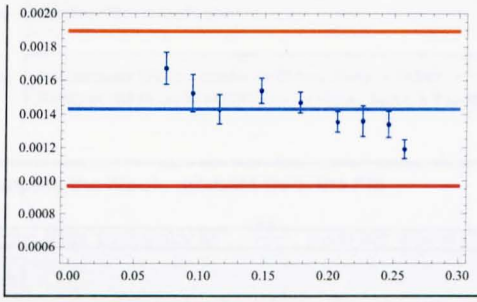

In[48]:=
```
Block[{mw, sd},
 mw = MeanValue[nn, JJ, PolPol, Δ];
 sd = StdDev[nn, JJ, PolPol, Δ];
 Show[
  ErrorListPlot[PlotData[nn, JJ, PolPol, Δ], PlotStyle → Directive[Blue],
   Joined → False, Frame → True, Axes → False, PlotRange → {-10, 10}],
  Plot[{mw - 3 sd, mw, mw + 3 sd}, {x, 0, 0.3}, PlotStyle →
    {Directive[Red, Thick], Directive[Lighter[Blue, 0.5], Thick], Directive[Orange, Thick]}]
 ]
]
```

Out[48]=

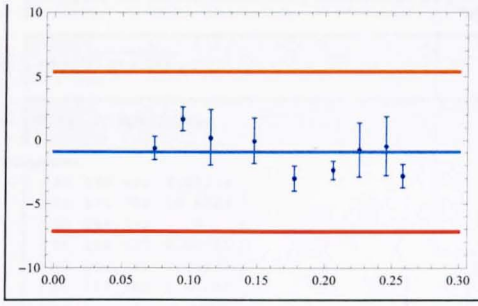

9 | *Individual EIT analysis n=20.nb*

In[49]:=
```
Block[{mw, sd},
 mw = MeanValue[nn, JJ, PolPol, γ3];
 sd = StdDev[nn, JJ, PolPol, γ3];
 Show[
  ErrorListPlot[PlotData[nn, JJ, PolPol, γ3], PlotStyle → Directive[Blue],
   Joined → False, Frame → True, Axes → False, PlotRange → {0, 6}],
  Plot[{mw - 3 sd, mw, mw + 3 sd}, {x, 0, 0.3}, PlotStyle →
    {Directive[Red, Thick], Directive[Lighter[Blue, 0.5], Thick], Directive[Orange, Thick]}]
 ]
]
```

Out[49]=

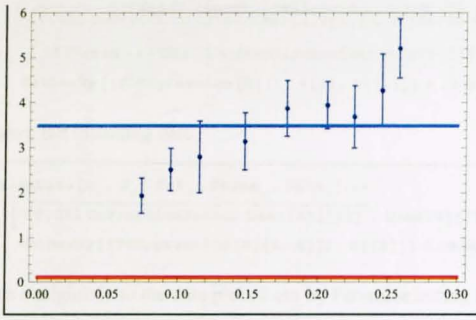

In[50]:=
```
Show[
 ErrorListPlot[PlotData[nn, JJ, PolPol, Ω23], PlotStyle → Directive[Black, PointSize[0.015]],
  Joined → False, Frame → True, Axes → False, PlotRange → {{0, .3}, {0, 25}}],
 Plot[Evaluate[LinFitData[nn, JJ, PolPol, Ω23][[1]]], {x, 0, 10}, PlotStyle → Directive[Red, Thick]],
 PlotRange → {{0, √(80 / 1000)}, 2 π {0, 25}},
 ImageSize → Medium,
 LabelStyle → Medium,
 FrameLabel → {"√(Power / W)", "Rabi Frequency/MHz"}
]
```

Out[50]=

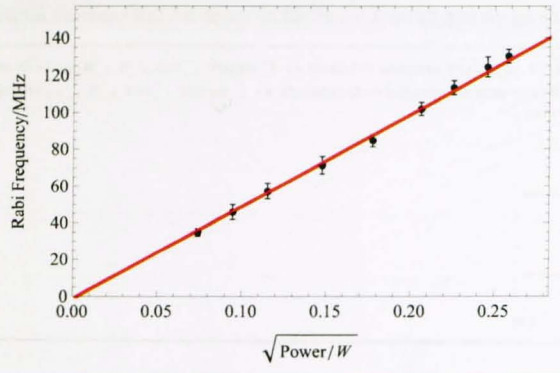

In[51]:=
```
PlotData[nn, JJ, PolPol, Ω23]
```

Out[51]=
```
{{0.074301, 34.6025, 1.97373}, {0.0948835, 45.6589, 4.02474}, {0.115475, 57.1507, 4.2337},
 {0.147742, 71.1674, 4.55789}, {0.17775, 84.4447, 3.3401}, {0.206486, 101.69, 3.59804},
 {0.225931, 113.078, 3.78303}, {0.245911, 124.111, 5.40363}, {0.258374, 129.944, 3.67059}}
```

In[52]:=
```
LinFitData[nn, JJ, PolPol, Ω23]
```

Out[52]=
```
{-1.01272 + 499.461 x, {0.891225, 6.01114}}
```

Michal J. Piotrowicz

Calculation of ^{87}Rb $\langle 5P_{3/2}, F, m_F \| er \| nD_J, F', m'_F \rangle$ reduced matrix elements from our EIT data and comparation with calculations.

Needs & Options

In[1]:=
```
Needs["ErrorBarPlots`"]
```

In[2]:=
```
SetOptions[Plot, Frame -> True, Axes → False];
SetOptions[ListPlot, Frame -> True, Axes → False];
```

Compute the dipole moment from the fits

Define Rabi frequency as : $\frac{-E\,\mu_{ab}}{\hbar}$, $\mu_{ab}$is the dipole matrix element. Normally this is quoted in units of [C.m] or in [e a_0]

Here are fitted gradients of the lines for each *n*. Fits: {n, *gradient*, *error*}

In[4]:=
```
Fits1 = {{20, 499.46134089453216`, 6.011138097615016`},
   {24, 375.7886440975376`, 15.692297209910095`}, {30, 244.5920075136407`, 5},
   {35, 198.53710395812996`, 6.065905833696925`}, {37, 150.70932503143462`, 9.059970439748112`},
   {40, 159.99573547436103`, 6.9705091149009375`}, {42, 142.34865867348577`, 5.803396261604885`}};
Fits2 = {{20, 587.3954204760797`, 20.702261404348818`}, {22, 492.3399568570571`, 11.813226917150443`},
   {26, 402.17765599736373`, 12.976993106290022`}, {28, 351.86954514915584`, 9.847368273409774`},
   {30, 309.8906815150935`, 5.077528085513882`}, {35, 222.23876938135467`, 13.894507650495749`},
   {37, 214.89071669205845`, 6.286701426128721`}, {40, 210.1906579586632`, 8.824495497452807`},
   {42, 163.73981021607474`, 10.622357608587468`}, {44, 160.55098080187082`, 9.921848746309633`},
   {48, 146.22043714373217`, 11.745621436424937`}};
```

In[6]:=
```
w0 = √(175 * 243);
```

In[7]:=
```
Fits1 // MatrixForm
```

Out[7]//MatrixForm=

20	499.461	6.01114
24	375.789	15.6923
30	244.592	5
35	198.537	6.06591
37	150.709	9.05997
40	159.996	6.97051
42	142.349	5.8034

2 | *dipole moments calculation.nb*

In[8]:=
```
Fits2 // MatrixForm
```

Out[8]//MatrixForm=

20	587.395	20.7023
22	492.34	11.8132
26	402.178	12.977
28	351.87	9.84737
30	309.891	5.07753
35	222.239	13.8945
37	214.891	6.2867
40	210.191	8.8245
42	163.74	10.6224
44	160.551	9.92185
48	146.22	11.7456

In[9]:=
```
Const = {c0 → 2.99792458 × 10^8, ħ → 1.054571596 × 10^-34, e0 → 8.854187817 × 10^-12,
    kB → 1.3806504 × 10^-23, a0 → 5.291772083 × 10^-11, qe → 1.602176462 × 10^-19};
```

In[10]:=
```
FivePnD1 = 1/(a0 qe) w0 ħ Sqrt[3/8 π e0 c0] (#[[2]], 2 #[[3]]) & /@ Fits1 /. Const;

FivePnD2 = 1/(a0 qe) w0 ħ Sqrt[3/8 π e0 c0] (#[[2]], 2 #[[3]]) & /@ Fits2 /. Const;
```

Printing nice tables with measured and calculated dipole moments

In[12]:=
```
Dipoles1 = Transpose[{Transpose[Fits1][[1]], Transpose[FivePnD1][[1]], Transpose[FivePnD1][[2]]}];
Dipoles2 = Transpose[{Transpose[Fits2][[1]], Transpose[FivePnD2][[1]], Transpose[FivePnD2][[2]]}];
Dipoles1 // TableForm
Dipoles2 // TableForm
```

Out[14]//TableForm=

20	0.0716414	0.00172444
24	0.0539021	0.00450172
30	0.0350836	0.00143437
35	0.0284776	0.00174015
37	0.0216173	0.00259908
40	0.0229494	0.00199966
42	0.0204181	0.00166485

Out[15]//TableForm=

20	0.0842544	0.00593895
22	0.0706199	0.00338891
26	0.0576873	0.00372277
28	0.0504712	0.00282496
30	0.0444499	0.00145661
35	0.0318773	0.00398598
37	0.0308233	0.00180349
40	0.0301492	0.00253152
42	0.0234864	0.00304728
44	0.023029	0.00284633
48	0.0209735	0.00336952

In[16]:=
```
DipolesIlya = Transpose[{{20, 22, 24, 26, 28, 30, 32, 35, 37, 40, 42, 44, 48}, {0.085, 0.07278, 0.06325,
      0.05563, 0.04944, 0.04432, 0.04002, 0.03476, 0.03187, 0.02821, 0.02615, 0.02433, 0.02126}}];
DipolesIlya //
 TableForm
```

Out[17]//TableForm=

20	0.085
22	0.07278
24	0.06325
26	0.05563
28	0.04944
30	0.04432
32	0.04002
35	0.03476
37	0.03187
40	0.02821
42	0.02615
44	0.02433
48	0.02126

Finding the scaling parameters for the data

In[18]:=
```
ScalingLaw1 = FindFit[
  Transpose[{# - 1.34809171 - 0.596 / (# - 1.34809171)^2 & /@ Transpose[Fits1][[1]], Transpose[FivePnD1][[1]]}],
  (n0 x^-1.5), {n0}, x]
ScalingLaw2 = FindFit[Transpose[{# - 1.34809171 - 0.596 / (# - 1.34809171)^2 & /@ Transpose[Fits2][[1]],
    Transpose[FivePnD2][[1]]}], (n0 x^-1.5), {n0}, x]
ScalingLawAll = FindFit[Transpose[{Join[# - 1.34809171 - 0.596 / (# - 1.34809171)^2 & /@ Transpose[Fits1][[1]],
     # - 1.34809171 - 0.596 / (# - 1.34809171)^2 & /@ Transpose[Fits2][[1]]],
    Join[Transpose[FivePnD1][[1]], Transpose[FivePnD2][[1]]]}], (n0 x^-1.5), {n0}, x]
```

Out[18]= {n0 → 5.61615}

Out[19]= {n0 → 6.75215}

Out[20]= {n0 → 6.29178}

In[21]:=
```
IlyaLine = FindFit[
  Transpose[{# - 1.34809171 - 0.596 / (# - 1.34809171)^2 & /@ {20, 22, 24, 26, 28, 30, 35, 37, 40, 42, 44, 48},
    0.5 {0.17583, 0.15054, 0.1308, 0.11504, 0.10223, 0.09163, 0.07187,
      0.06588, 0.05833, 0.05406, 0.05029, 0.04394}}], (n0 x^-1.5), {n0}, x]
```

Out[21]= {n0 → 7.04918}

4 | *dipole moments calculation.nb*

In[22]:=
```
Show[
 ListPlot[DipolesZiya, Joined → True, PlotStyle → Directive[Red, Thick, Dashed]],
 (*Plot[{n0 (x-1.34809171-0.596/(x-1.34809171)^2)^-1.5}/.ZiyaLine,
  {x,19,49},PlotStyle→Directive[Red,Thick,Dashed]],*)
 ErrorListPlot[Dipoles2, Joined → False, PlotStyle → Directive[Black, PointSize[0.012]]],
 ErrorListPlot[Dipoles1, Joined → False, PlotStyle → Directive[Gray, PointSize[0.012]]],
 (*Plot[{n0 (x-1.35)^-1.5}/.ScalingLaw2,{x,20,48},PlotStyle→Directive[Black,Thick,Dashed]],
 Plot[{n0( x-1.35)^-1.5}/.ScalingLaw1,{x,20,48},PlotStyle→Directive[Gray,Thick,Dashed]],
 Plot[{n0 (x-1.35)^-1.5}/.ScalingLawAll,{x,20,48},PlotStyle→Directive[Blue,Thick,Dashed]],*)
 FrameLabel → {"Principal Quantum Number n", "Dipole moment/ e a₀"},
 ImageSize → Large,
 LabelStyle → Large,
 PlotRange → {{19, 49}, {0, 0.1}}
]
```

Out[22]=

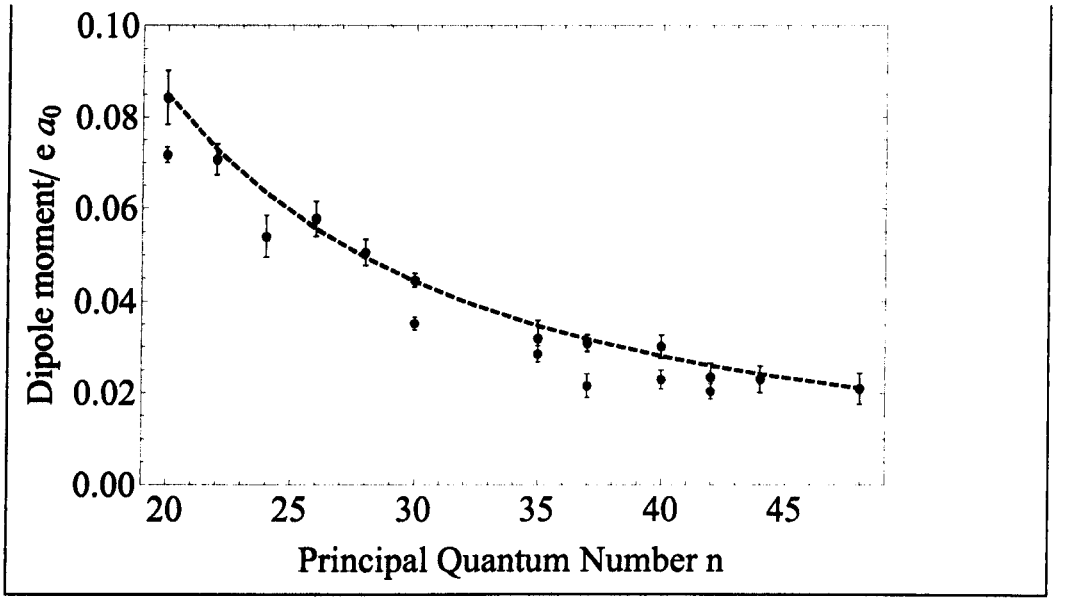

Acknowledgements

My first thanks should go to Dr. Silvia Bergamini, my supervisor, for giving me the opportunity to work on a completely new project that was starting from nothing. It was her who gave me all the support I needed, and who was constantly saying that the things would go in the right way, even when they didn't seem to.

During my second year Calum MacCormick joined us and we could officially call ourselves the Cold Atoms Group. It was a great pleasure to work with Calum in the lab, I have learnt a lot from his knowledge and skills. Calum was also indispensable when it came to help with data analysis.

The person who deserves a lot of credit is Ilya Beterov. If I hadn't met him at EGAS conference I wouldn't have the theoretical data to compare my results with. However, his help was not only with providing the theoretical data: Ilya also convinced me of the importance of the measurements of the dipole moments. Thanks to the Royal Society and the Russian Foundation for Basic Research our collaboration was extended and allowed me to spend two weeks in Novosibirsk participating in the labwork there.

The only thing that made the stay in the town of 250 roundabouts enjoyable was a group of friends I have met there. Firstly, I have to thank Gosia, whom I know from Gdańsk. Then comes our crazy *Motley Crue* office. Without (in alphabetical order) Jonty, Stefano and Vladimir the long days at OU and in MK

would be unbearable. We had a lot of laugh in the office, trying to pin Stefano's palm *with darts provided*, gathering all the odd equipment including our unique binary solar system... I hope the new occupants of the office will make a good use of the place. There were also those unforgettable parties at Marshworth, mostly organised by Katarina.

Last but not least I would like to thank my family for all the support during the last four years and my whole earlier life.

Bibliography

ABEL, R. P., A. K. MOHAPATRA, M. G. BASON, J. D. PRITCHARD, K. J. WEATHERILL, U. RAITZSCH, and C. S. ADAMS (2009). "Laser frequency stabilization to excited state transitions using electromagnetically induced transparency in a cascade system." *Appl. Phys. Lett.*, **94**, 071107.

ABI-SALLOUM, T. Y. (2010). "Electromagnetically induced transparency and Autler-Townes splitting: Two similar but distinct phenomena in two categories of three-level atomic systems." *Phys. Rev. A*, **81**, p. 053836.

ANDERSON, W. R., J. R. VEALE, and T. F. GALLAGHER (1998). "Resonant Dipole-Dipole Energy Transfer in a Nearly Frozen Rydberg Gas." *Phys. Rev. Lett.*, **80**, pp. 249–252.

ARNOLD, A. S., J. S. WILSON, and M. G. BOSHIER (1998). "A simple extended-cavity diode laser." *Rev. Sci. Instrum.*, **69**, pp. 1236–1239.

AUTLER, S. H. and C. H. TOWNES (1955). "Stark Effect in Rapidly Varying Fields." *Phys. Rev.*, **100**, pp. 703–722.

BATES, D. R. and A. DAMGAARD (1949). "The Calculation of the Absolute Strengths of Spectral Lines." *Phil. Trans. R. Soc. A*, **242**, pp. 101–122.

BENDKOWSKY, V., B. BUTSCHER, J. NIPPER, J. P. SHAFFER, R. LOW, and T. PFAU (2009). "Observation of ultralong-range Rydberg molecules." *Nature*, **458**, pp. 1005–1008.

BETEROV, I. (2010). Private communication.

BETEROV, I. I., I. I. RYABTSEV, D. B. TRETYAKOV, and V. M. ENTIN (2009). "Quasiclassical calculations of blackbody-radiation-induced depopulation rates and effective lifetimes of Rydberg nS, nP, and nD alkali-metal atoms with $n \leq 80$." *Phys. Rev. A*, **79**, 052504.

BETHE, H. A. and E. E. SALPETER (1977). *Quantum Mechanics of One- and Two-Electron Atoms*. Springer, 1st edition.

BOISSEAU, C., I. SIMBOTIN, and R. CÔTÉ (2002). "Macrodimers: Ultralong Range Rydberg Molecules." *Phys. Rev. Lett.*, **88**, 133004.

BOLLER, K.-J., A. IMAMOLU, and S. E. HARRIS (1991). "Observation of electromagnetically induced transparency." *Phys. Rev. Lett.*, **66**, pp. 2593–2596.

BRANDEN, D. B., T. JUHASZ, T. MAHLOKOZERA, C. VESA, R. O. WILSON, M. ZHENG, A. KORTYNA, and D. A. TATE (2010). "Radiative lifetime measurements of rubidium Rydberg states." *J. Phys. B: At., Mol. Opt. Phys.*, **43**, p. 015002 (13pp).

BRINK, D. M. and G. R. SATCHLER (1994). *Angular Momentum*. Oxford University Press, third edition edition.

BUDKER, D., D. F. KIMBALL, S. M. ROCHESTER, and V. V. YASHCHUK (1999). "Nonlinear Magneto-optics and Reduced Group Velocity of Light in Atomic Vapor with Slow Ground State Relaxation." *Phys. Rev. Lett.*, **83**, pp. 1767–1770.

CALIEBE, E. and K. NIEMAX (1979). "Oscillator strengths of the principal series lines of Rb." *J. Phys. B: At. Mol. Phys.*, **12**, p. L45.

CHU, S., L. HOLLBERG, J. E. BJORKHOLM, A. CABLE, and A. ASHKIN (1985). "Three-dimensional viscous confinement and cooling of atoms by resonance radiation pressure." *Phys. Rev. Lett.*, **55**, pp. 48–51.

CLARKE, J., H. CHEN, and W. A. VAN WIJNGAARDEN (2001). "Electromagnetically induced transparency and optical switching in a rubidium cascade system." *Appl. Opt.*, **40**, pp. 2047–2051.

CUBEL LIEBISCH, T., A. REINHARD, P. R. BERMAN, and G. RAITHEL (2005). "Atom Counting Statistics in Ensembles of Interacting Rydberg Atoms." *Phys. Rev. Lett.*, **95**, 253002.

DALIBARD, J. and C. COHEN-TANNOUDJI (1989). "Laser cooling below the Doppler limit by polarization gradients: simple theoretical models." *J. Opt. Soc. Am. B*, **6**, pp. 2023–2045.

VAN DITZHUIJZEN, C. S. E., A. F. KOENDERINK, J. V. HERNÁNDEZ, F. ROBICHEAUX, L. D. NOORDAM, and H. B. VAN LINDEN VAN DEN HEUVELL (2008). "Spatially Resolved Observation of Dipole-Dipole Interaction between Rydberg Atoms." *Phys. Rev. Lett.*, **100**, 243201.

VAN DITZHUIJZEN, C. S. E., A. F. KOENDERINK, L. D. NOORDAM, and H. B. VAN LINDEN VAN DEN HEUVELL (2006). "Simultaneous position and state measurement of Rydberg atoms." *Eur. Phys. J. D*, **40**, pp. 13–17.

DRAVSKIKH, A. F. and Z. V. DRAVSKIKH (1967). "Detection and Investigation of the 5-cm Excited-Hydrogen Radio Line (n105 –> n104) in Several Galactic Nebulae." *Sov. Astron.*, **11**, p. 27.

DYACHKOV, L. G. and P. M. PANKRATOV (1994). "On the use of the semiclassical approximation for the calculation of oscillator strengths and photoionization cross sections." *J. Phys. B: At., Mol. Opt. Phys.*, **27**, p. 461.

FAROOQI, S. M., D. TONG, S. KRISHNAN, J. STANOJEVIC, Y. P. ZHANG, J. R. ENSHER, A. S. ESTRIN, C. BOISSEAU, R. CÔTÉ, E. E. EYLER, and P. L. GOULD (2003). "Long-Range Molecular Resonances in a Cold Rydberg Gas." *Phys. Rev. Lett.*, **91**, 183002.

FLEISCHHAUER, M., A. IMAMOGLU, and J. P. MARANGOS (2005). "Electromagnetically induced transparency: Optics in coherent media." *Rev. Mod. Phys.*, **77**, 633.

FRIEDLER, I., D. PETROSYAN, M. FLEISCHHAUER, and G. KURIZKI (2005). "Long-range interactions and entanglement of slow single-photon pulses." *Phys. Rev. A*, **72**, p. 043803.

GAËTAN, A., Y. MIROSHNYCHENKO, T. WILK, A. CHOTIA, M. VITEAU, D. COMPARAT, P. PILLET, A. BROWAEYS, and P. GRANGIER (2009). "Observation of collective excitation of two individual atoms in the Rydberg blockade regime." *Nature Phys.*, **5**, pp. 115–118.

GALLAGHER, T. F. (1994). *Rydberg Atoms*. Cambridge Monographs on Atomic, Molecular and Chemical Physics (No. 3). Cambridge University Press, 2nd (2005) edition.

GEA-BANACLOCHE, J., Y.-Q. LI, S.-Z. JIN, and M. XIAO (1995). "Electromagnetically induced transparency in ladder-type inhomogeneously broadened media: Theory and experiment." *Phys. Rev. A*, **51**, pp. 576–584.

GOUNAND, F. (1979). "Calculation of radial matrix elements and radiative lifetimes for highly excited states of alkali atoms using the Coulomb approximation." *J. Phys. France*, **40**, pp. 457–460.

GRIMM, R., M. WEIDEMÜLLER, and Y. B. OVCHINNIKOV (2000). "Optical dipole traps for neutral atoms." *Adv. At. Mol. Opt. Phys.*, **42**, pp. 95–170.

GÜRTLER, A. and W. J. VAN DER ZANDE (2004). "ℓ-state selective field ionization of rubidium Rydberg states." *Phys. Lett. A*, **324**, pp. 315 – 320.

GUTTERRES, R. F., C. AMIOT, A. FIORETTI, C. GABBANINI, M. MAZZONI, and O. DULIEU (2002). "Determination of the ^{87}Rb $5p$ state dipole matrix element and radiative lifetime from the photoassociation spectroscopy of the Rb_2 $0_g^-(P_{3/2})$ long-range state." *Phys. Rev. A*, **66**, p. 024502.

HÄNSCH, T. and A. SCHAWLOW (1975). "Cooling of gases by laser radiation." *Opt. Commun.*, **13**, pp. 68 – 69.

HARRIS, S. E., J. E. FIELD, and A. IMAMOĞLU (1990). "Nonlinear optical processes using electromagnetically induced transparency." *Phys. Rev. Lett.*, **64**, pp. 1107–1110.

HARTING, E. and F. H. READ (1976). *Electrostatic Lenses*. Elsevier, Amsterdam.

HARTLEY, W. N. (1883). "LVI.—On homologous spectra." *J. Chem. Soc., Trans.*, **43**, pp. 390–400.

HAU, L. V., E. HARRIS, Z. DUTTON, and C. H. BEHROOZI (1999). "Light speed reduction to 17 metres per second in an ultracold atomic gas." *Nature*, **397**, pp. 594–598.

HAWTHORN, C. J., K. P. WEBER, and R. E. SCHOLTEN (2001). "Littrow configuration tunable external cavity diode laser with fixed direction output beam." *Rev. Sci. Instrum.*, **72**, pp. 4477–4479.

HEIDEMANN, R., U. RAITZSCH, V. BENDKOWSKY, B. BUTSCHER, R. LÖW, L. SANTOS, and T. PFAU (2007). "Evidence for Coherent Collective Rydberg Excitation in the Strong Blockade Regime." *Phys. Rev. Lett.*, **99**, 163601.

HOPKINS, S. A. and A. V. DURRANT (1997). "Parameters for polarization gradients in three-dimensional electromagnetic standing waves." *Phys. Rev. A*, **56**, pp. 4012–4022.

ISENHOWER, L., E. URBAN, X. L. ZHANG, A. T. GILL, T. HENAGE, T. A. JOHNSON, T. G. WALKER, and M. SAFFMAN (2010). "Demonstration of a Neutral Atom Controlled-NOT Quantum Gate." *Phys. Rev. Lett.*, **104**, 010503.

JAKSCH, D., J. I. CIRAC, P. ZOLLER, S. L. ROLSTON, R. CÔTÉ, and M. D. LUKIN (2000). "Fast Quantum Gates for Neutral Atoms." *Phys. Rev. Lett.*, **85**, pp. 2208–2211.

KASH, M. M., V. A. SAUTENKOV, A. S. ZIBROV, L. HOLLBERG, G. R. WELCH, M. D. LUKIN, Y. ROSTOVTSEV, E. S. FRY, and M. O. SCULLY (1999). "Ultraslow Group Velocity and Enhanced Nonlinear Optical Effects in a Coherently Driven Hot Atomic Gas." *Phys. Rev. Lett.*, **82**, pp. 5229–5232.

LEE, S. A., J. HELMCKE, J. L. HALL, and B. P. STOICHEFF (1978). "Doppler-free two-photon transitions to Rydberg levels: convenient, useful, and precise reference wavelengths for dye lasers." *Opt. Lett.*, **3**, pp. 141–143.

LETT, P. D., R. N. WATTS, C. I. WESTBROOK, W. D. PHILLIPS, P. L. GOULD, and H. J. METCALF (1988). "Observation of Atoms Laser Cooled below the Doppler Limit." *Phys. Rev. Lett.*, **61**, pp. 169–172.

LI, W., I. MOURACHKO, M. W. NOEL, and T. F. GALLAGHER (2003). "Millimeter-wave spectroscopy of cold Rb Rydberg atoms in a magneto-optical trap: Quantum defects of the *ns*, *np*, and *nd* series." *Phys. Rev. A*, **67**, 052502.

LIU, C., Z. DUTTON, C. H. BEHROOZI, and L. V. HAU (2001). "Observation of coherent optical information storage in an atomic medium using halted light pulses." *Nature*, **409**, pp. 490–493.

LIU, I. C. H. and J. M. ROST (2006). "Polyatomic Molecules Formed with a Rydberg Atom in an Ultracold Environment." *Eur. Phys. J. D*, **40**, p. 65.

LORENZEN, C.-J. and K. NIEMAX (1983). "Quantum Defects of the $n^2P_{1/2,3/2}$ Levels in ^{39}K I and ^{85}Rb I." *Phys. Scr.*, **27**, pp. 300–305.

LÖW, R., U. RAITZSCH, R. HEIDEMANN, V. BENDKOWSKY, B. BUTSCHER, A. GRABOWSKI, and T. PFAU (2007). "Apparatus for excitation and detection of Rydberg atoms in quantum gases." `http://arxiv.org/abs/0706.2639`.

LUKIN, M. D., M. FLEISCHHAUER, R. COTE, L. M. DUAN, D. JAKSCH, J. I. CIRAC, and P. ZOLLER (2001). "Dipole Blockade and Quantum Information Processing in Mesoscopic Atomic Ensembles." *Phys. Rev. Lett.*, **87**, 037901.

MCCARRON, D. J., S. A. KING, and S. L. CORNISH (2008). "Modulation transfer spectroscopy in atomic rubidium." *Meas. Sci. Technol.*, **19**, 105601 (8pp).

MEZGER, P. and B. HOGLUND (1967). "Galactic H II Regions. II. Observations of Their Hydrogen 109α Recombination-Line Radiation at the Frequency 5009 MHz." *Ap. J.*, **147**, p. 490.

MOHAPATRA, A. K., M. G. BASON, B. BUTSCHER, K. J. WEATHERILL, and C. S. ADAMS (2008). "A giant electro-optic effect using polarizable dark states." *Nature Phys.*, **4**, pp. 890–894.

MOHAPATRA, A. K., T. R. JACKSON, and C. S. ADAMS (2007). "Coherent Optical Detection of Highly Excited Rydberg States Using Electromagnetically Induced Transparency." *Phys. Rev. Lett.*, **98**, 113003.

MOURACHKO, I., D. COMPARAT, F. DE TOMASI, A. FIORETTI, P. NOSBAUM, V. M. AKULIN, and P. PILLET (1998). "Many-Body Effects in a Frozen Rydberg Gas." *Phys. Rev. Lett.*, **80**, pp. 253–256.

DE OLIVEIRA, A. L., M. W. MANCINI, V. S. BAGNATO, and L. G. MARCASSA (2003). "Rydberg Cold Collisions Dominated by Ultralong Range Potential." *Phys. Rev. Lett.*, **90**, 143002.

PRITCHARD, D. E., E. L. RAAB, V. BAGNATO, C. E. WIEMAN, and R. N. WATTS (1986). "Light Traps Using Spontaneous Forces." *Phys. Rev. Lett.*, **57**, pp. 310–313.

PRITCHARD, J. D., D. MAXWELL, A. GAUGUET, K. J. WEATHERILL, M. P. A. JONES, and C. S. ADAMS (2010). "Cooperative Atom-Light Interaction in a Blockaded Rydberg Ensemble." *Phys. Rev. Lett.*, **105**, p. 193603.

PROTSENKO, I. E., G. REYMOND, N. SCHLOSSER, and P. GRANGIER (2002). "Operation of a quantum phase gate using neutral atoms in microscopic dipole traps." *Phys. Rev. A*, **65**, 052301.

RALCHENKO, Y., A. KRAMIDA, J. READER, and N. A. T. (2008) (2008). "NIST Atomic Spectra Database (version 3.1.5), [Online]." `http://physics.nist.gov/asd3`.

READ, F. H., A. ADAMS, and J. R. SOTO-MONTIEL (1971). "Electrostatic cylinder lenses. I. Two element lenses." *J. Phys. E: Sci. Instrum.*, **4**, p. 625.

REETZ-LAMOUR, M., T. AMTHOR, J. DEIGLMAYR, and M. WEIDEMÜLLER (2008). "Rabi Oscillations and Excitation Trapping in the Coherent Excitationof a Mesoscopic Frozen Rydberg Gas." *Phys. Rev. Lett.*, **100**, 253001.

SCHLOSSER, N., G. REYMOND, I. PROTSENKO, and P. GRANGIER (2001). "Sub-poissonian loading of single atoms in a microscopic dipole trap." *Nature*, **411**, pp. 1024–1027.

SHABANOVA, L. N. and A. N. KHLYUSTALOV (1984). "Oscillator strengths of lines of the principal series of rubidium." *Opt. Spectrosc.*, **56**, p. 128.

SINGER, K., M. REETZ-LAMOUR, T. AMTHOR, L. G. MARCASSA, and M. WEIDEMULLER (2004). "Suppression of Excitation and Spectral Broadening Induced by Interactions in a Cold Gas of Rydberg Atoms." *Phys. Rev. Lett.*, **93**, 163001.

SORTAIS, Y. R. P., H. MARION, C. TUCHENDLER, A. M. LANCE, M. LAMARE, P. FOURNET, C. ARMELLIN, R. MERCIER, G. MESSIN, A. BROWAEYS, and P. GRANGIER (2007). "Diffraction-limited optics for single-atom manipulation." *Phys. Rev. A*, **75**, p. 013406.

TAUSCHINSKY, A., R. M. T. THIJSSEN, S. WHITLOCK, H. B. VAN LINDEN VAN DEN HEUVELL, and R. J. C. SPREEUW (2010). "Spatially resolved excitation of Rydberg atoms and surface effects on an atom chip." *Phys. Rev. A*, **81**, p. 063411.

TEO, B. K., D. FELDBAUM, T. CUBEL, J. R. GUEST, P. R. BERMAN, and G. RAITHEL (2003). "Autler-Townes spectroscopy of the $5S_{1/2} - 5P_{3/2} - 44D$ cascade of cold ^{85}Rb atoms." *Phys. Rev. A*, **68**, 053407.

THEODOSIOU, C. E. (1984). "Lifetimes of alkali-metal—atom Rydberg states." *Phys. Rev. A*, **30**, pp. 2881–2909.

TONG, D., S. M. FAROOQI, J. STANOJEVIC, S. KRISHNAN, Y. P. ZHANG, R. COTE, E. E. EYLER, and P. L. GOULD (2004). "Local Blockade of Rydberg Excitation in an Ultracold Gas." *Phys. Rev. Lett.*, **93**, 063001.

URBAN, E., T. A. JOHNSON, T. HENAGE, L. ISENHOWER, D. D. YAVUZ, T. G. WALKER, and M. SAFFMAN (2009). "Observation of Rydberg blockade between two atoms." *Nature Phys.*, **5**, pp. 110–114.

VOGT, T., M. VITEAU, A. CHOTIA, J. ZHAO, D. COMPARAT, and P. PILLET (2007). "Electric-Field Induced Dipole Blockade with Rydberg Atoms." *Phys. Rev. Lett.*, **99**, 073002.

WALKER, T. G. and M. SAFFMAN (2008). "Consequences of Zeeman degeneracy for the van der Waals blockade between Rydberg atoms." *Phys. Rev. A*, **77**, p. 032723.

WEATHERILL, K. J., J. D. PRITCHARD, R. P. ABEL, M. G. BASON, A. K. MOHAPATRA, and C. S. ADAMS (2008). "Electromagnetically induced transparency of an interacting cold Rydberg ensemble." *J. Phys. B: At., Mol. Opt. Phys.*, **41**, 201002 (5pp).

WILK, T., A. GAËTAN, C. EVELLIN, J. WOLTERS, Y. MIROSHNYCHENKO, P. GRANGIER, and A. BROWAEYS (2010). "Entanglement of Two Individual Neutral Atoms Using Rydberg Blockade." *Phys. Rev. Lett.*, **104**, p. 010502.

ZHANG, X. L., L. ISENHOWER, A. T. GILL, T. G. WALKER, and M. SAFFMAN (2010). "Deterministic entanglement of two neutral atoms via Rydberg blockade." *Phys. Rev. A*, **82**, p. 030306.